EPR distance measurements using triaryl methyl radicals and EPR investigation of electron transfer processes in organic radicals

Dissertation

zur

Erlangung des Doktorgrades (Dr. rer. nat.)

der

Mathematisch-Naturwissenschaftlichen Fakultät

der

Rheinischen Friedrich-Wilhelms-Universität Bonn

vorgelegt von

Andreas Berndhäuser

aus Köln

Bonn 2017

Angefertigt mit Genehmigung der Mathematisch-Naturwissenschaftlichen Fakultät der Rheinischen Friedrich-Wilhelms Universität Bonn

1. Gutachter : Prof. Dr. Olav Schiemann
2. Gutachter : Prof. Dr. Helmut Baltruschat

Tag der Promotion: 21.03.2018

Erscheinungsjahr: 2018

In memory of my father

Kein Plan überlebt die erste Feindberührung.

- Helmuth von Moltke -

Abstract

EPR is a valuable tool for the investigation of biological structures. Most EPR-based distance measurements rely on the site directed spin labeling of the investigated biomolecule, since most biomolecular structures do not contain unpaired electrons. Most measurements today are conducted in frozen buffer solutions. These conditions are not the natural environment of the biomolecules, and may affect their geometric structure. To overcome this drawback of the method, research efforts are made to develop protocols for distance measurements under biologically relevant conditions. In the pursuit of measurement conditions that are closer to biological conditions, new kinds of spin labels have emerged to overcome the limitations of the widely used nitroxide spin labels. One of the new kinds of labels is the triarylmethyl radicals (trityl). In this work, the optimization and comparison of four different pulsed EPR-based distance measurement techniques on two organic bistrityl model compounds is presented. Building on these results, the use of new trityl spin labels for trityl-iron(III) distance measurement on *pseudomonas putida* CYP101 P450 is demonstrated. The performance of the new spin labels is compared to the commercially available MTSSL nitroxide spin label and two other trityl spin labels known from literature. The use of one of these new spin labels for the first *in cell* distance measurement with a trityl radical is then demonstrated. This is also the first *in cell* distance measurement between a spin label and a native metal cofactor. The second part of this work deals with the investigation of electron transfer processes and radical intermediates of catalytic reactions. To that end, two setups were designed that combine electrochemistry and EPR. The first is a potentiostatic flat cell, the second a galvanostatic flow cell. Both systems were characterized using Wurster`s reagent and employed in the study of the electronic structure and electron self-exchange rate of radical salts of bis(2-pyridylmethyl)azine and bis(2-pyridylmethyl-5-tert-butyl)azine. Further, they were used to investigate the mechanisms of copper-catalyzed coupling reactions of tetrahydroisochinoline (THIQ) and the MacMillan organo-catalytic cycle. In all cases, chemical means for the generation of the radicals and additional methods like freeze quench were also employed. In the work presented here, strong experimental evidence is given for the existence of radical intermediates in both investigated catalytic cycles. This supports proposed radical mechanisms known from the literature.

Acknowledgements

As my time as a graduate student comes to an end, I would like to express my gratitude to a number of people that accompanied me along the way. Firstly, I would like to express my gratitude towards my supervisor, Prof. Dr. Olav Schiemann, who has supported me in my work and personally during trying times. Further, a number of colleagues that helped me greatly should be given thanks: Dr. Dinar Abdullin, Dr. Hideto Matsuoka, Dr. Yaser Nejaty-Jahromy, Dr. Erik Schubert and Mr. Jean-Jacques Jassoy supported me greatly during my work. Much of my work would not have been possible without the outstanding work of our biochemical lab, and I want to thank Mrs. Nicole Florin, Mr. Fraser Duthie and Dr. Gregor Hagelüken for that. During my time here, I had the pleasure of supervising the bachelor thesis of Mr. Sebastian Spicher, and would like to thank him for his excellent work. I also wish to express my gratitude towards the personal of the electronics and mechanics workshops, and their respective workshop leaders Mr. Rolf Paulig and Mr. Peter Königshoven.

Many of the projects presented here were done in collaboration with other work groups, and I wish to express my gratitude towards my collaborators: Mr. Christian Mundt and PD. Dr. Marianne Engeser, Mr. Tongtong Wang and Prof. Dr. Dirk Menche, Mr. Josua Bächle, Dr. Borjana Mladenova and Prof. Dr. Günther Grampp as well as Dr. David Engelhart and Prof. Dr. Guido Clever.

Lastly, I want to thank the DFG for funding via the priority program 1601.

Table of Content

1 Introduction

1.1 Motivation and Aim

This work deals with two overarching topics: The determination of inter-spin distances by EPR and the investigation of electron transfer processes by a combination of electrochemistry and EPR. Distance information can be a valuable tool to acquire structural information of large molecules. A classic field where structural information is used to gain insight into complex procedures is structural biology. The structure-function relationship seen e.g. in proteins is a central paradigm of modern biology, and is described in standard textbooks.[1] A frequently used method for the investigation of such structures is X-ray crystallography.[2] It has been used in a large number of studies and is the most widely used technique for the investigation of biological macromolecules However, it is limited to those structures that can be crystallized, which excludes many polymeric or fibrous structures. In addition, the crystallization process is often tedious and time consuming. The different domains of large proteins often have to be crystallized individually. Also, molecular dynamics are not preserved in the crystal and can actually lead to a loss of resolution in X-ray diffraction. Another technique that made tangible progress in the past 15 years is nuclear magnetic resonance spectroscopy (NMR), which can be used to determine the structure of a protein on a bond-to-bond and angle-to-angle basis via the nuclear Overhauser effect (NOE) as well as with short distance constraints derived from residual dipolar coupling.[3] The information that can be obtained by this method is very detailed, however, it is limited in its applications by the size of the proteins. Currently, proteins up to a size of 100 kDa can be accessed. Also, due the high amount of measurements that are often necessary, the method is also time consuming and expansive. As an additional issue, the investigation of structures that contain paramagnetic metal centers is difficult, because paramagnetic species affect both the chemical shift and the relaxation behavior of the surrounding nuclei.[4] Another technique that saw significant advancements is cryo-EM, a variety of transmission electron microscopy (TEM). The method is nowadays used regularly to solve difficult crystal structures of proteins, because it offers a very high resolution of up to 4.5 Å. It is often used in cases where regular X-ray diffraction cannot offer a sufficiently high resolution.[5] These methods are powerful tools to determine biological structures, but other techniques that provide long distance constraints are often used to good effect where the mentioned limitations make the use of

x-ray diffraction and NMR difficult. An example for such a technique is fluorescence resonance energy transfer (FRET).[6] In a FRET experiment, the distance between two fluorescent dye molecules is determined based on the radiation free energy transfer between the donor and acceptor molecule due to dipolar interaction. Via this method, distances of up to 10 nm are readily accessible. More interestingly, it can be performed in liquid solution and allows to observe dynamics in real time with very high accuracy, since even single molecules can be observed. A major challenge of FRET is that the orientation factor of the dipolar interaction is often uncertain, which causes uncertainties in the extraction of the inter-dye distances. In addition, for all FRET experiments, two different fluorophores must be introduced. Electron paramagnetic resonance (EPR) is a method of magnetic resonance spectroscopy akin to NMR, and allows for the ready determination of inter-spin distances in the range of 4 to 160 Å.[7] While it was limited to short distances up to 2 nm 25 years ago, the tremendous advances made since established it as a valuable tool for structural biology. EPR can be used to determine the distance between two paramagnetic centers based on their dipolar coupling. Two this end, pulsed experiments have been developed, with pulsed electron-electron double resonance (PELDOR)[8] being the most prominent and most widely used. Other techniques like relaxation induced dipolar modulation enhancement (RIDME) [9] or double quantum coherence (DQC)[10] are used less frequently, but gained attention in recent years. While EPR can be and has been performed on native paramagnetic centers, it usually requires the introduction of paramagnetic species into the investigated biological structure. This is often done in the form of small organic molecules, which are referred to as spin labels. The most commonly used kind of spin labels are nitroxide labels, for which many different labeling strategies have been developed.[11] However, as EPR strives to achieve distance measurements under conditions that are close to biological conditions, e.g. measurements at room temperature or in living cells, nitroxides are limited by their short relaxation time at ambient temperatures and their short lifespan under reducing conditions. To overcome these limitations, new classes of spin labels have been investigated. The most prominent among these are gadolinium(III) complexes[12] and triarylmethyl spin label (trityl).[13] Gadolinium(III) complexes have been successfully employed for distance measurement on a large number of protein samples, and were used to successfully measure distances in living cells.[14] Their most important feature is that they employ gadolinium in its thermodynamically most stable oxidation state of +III and are therefore virtually indefinitely stable under biological conditions. However, they are known to show a transversal relaxation time of the order of magnitude of 5 μS even at 10-15 K, and relax almost instantaneously at

ambient temperatures.[15] Also, they have a spin S = 7/2 system, in which several different transitions can be exited. This was shown to cause ambiguities in the interpretation of the experimental data.[16] Trityls have emerged as in interesting new class of spin labels, which show long relaxation times in the order of magnitude up to 26 μs (T_1) and 7.5 μs (T_2) even at room temperature and, while not being quite as stable as gadolinium(III) complexes, they are much more resistant to reduction under biological conditions than nitroxide spin labels.[17] While they received increasing attention in the last five years, they are yet not very widely used. Part of the reason for this is certainly that the synthesis of trityl spin labels is rather demanding and the number of work groups today that can provide them is limited to a scarce hand full. However, a second part is that due to their narrow spectral width, they are especially well suited for the use with single frequency experiments, which are used more rarely. This work aims at promoting the use of trityl spin labels by providing a comparison of the available EPR distance measurement techniques for trityl-trityl distances. To this end, two different bistrityl model compounds are investigated. Building on that, four new trityl spin labels are presented and characterized in terms of spectroscopic properties and labeling efficiencies. Two are then used for distance measurements on *pseudomonas putida* cytochrome CYP101C58 to determine the distance to a native iron(III) cofactor. Their performance in terms of modulation depth and signal-to-noise ratio is compared to MTSSL, the most commonly used nitroxide spin label, and in terms of expected width of the distance distribution to other available trityl spin labels. Lastly, the first use of a trityl spin label in an in cell distance measurement is demonstrated by measuring the trityl-iron(III) distance inside a living oocyte cell of *xenopus laevis*.

Electron transfer processes are very important steps in a large variety of chemical and biological processes. Examples of such include photosynthesis[18] as well as a variety of catalytic chemical reactions.[19] While the theory of the electron transfer is well developed since Marcus Nobel prize winning theory[20] was first published in 1956, the vast amount of different applications have kept this field of research in the focus of many studies. Since the physics of these processes is well understood, studies focus on the details of specific cases to understand effects of the molecular structures on the electron transfer. Another focus is the investigation of processes where the electron transfer is only one step of a longer reaction chain. A critical issue of such studies is that electron transfer can be a very fast process, where none of the formed transient species is particularly stable and are therefore difficult to detect. To overcome this, many techniques aiming at the detection of short-lived species have been developed, e.g. stopped flow techniques, electron transfer emission spectra obtained via

FT-IR and RAMAN spectroscopy as well as pump-probe experiments that rely on optical spectroscopy.[21] Where the electron transfer includes open-shell systems, EPR can be applied to monitor electron transfer processes or radical intermediates that may arise during a reaction. Such radical intermediates play an important role in many organic reactions, be it in metalorganic catalysis or organocatalysis.[22] These radical intermediates and the processes involved in their generation often elude detection by spectroscopic means due to their short live span. A way to detect them regardless is to generate these radical by means of electrochemical oxidation or reduction either in situ directly inside the spectroscopic cell or in a separate reaction chamber, from where it is transported to the measurement chamber via a flow-cell system. This work aims at the development of electrochemical setups that combine electrolysis and EPR spectroscopy. These setups are then applied in the investigation of electron transfer processes and radical intermediates in organic radical salts of bis(2-pyridylmethyl)azine and bis(2-pyridylmethyl-5-tert-butyl)azine, copper-catalyzed coupling reactions on tetrahydroisoquinolinone (THIQ) and the MacMillan organocatalytic cycle.

1.2 Basics of EPR

1.2.1 Magnetic Interactions

In this section, a short introduction into EPR is given. Detailed descriptions of EPR are given in a number of excellent textbooks and lecture scripts, and the information given here is compiled from these sources.[23]

EPR is a method that can be used to measure electron transitions between spin states of paramagnetic species in an applied magnetic field by means of resonant absorption of microwave radiation. As such, it monitors the interaction of electron spins not only with the applied magnetic field, but also the interactions with other electron and nuclear spins in the surrounding. The spin-system is an ensemble of interacting quantum mechanical objects and is best describe by a Hamilton operator. However, a full Hamiltonian of a paramagnetic spin system is a rather unwieldy tool for the interpretation of experimental EPR data. To find a more applicable approach, Abragram and Pryce suggested to separate the spin system from all other interactions.[24] The resulting expression is known as the static Spin-Hamiltonian, which describes the spin system as a function of the electron spin operator $\boldsymbol{S}$ and the nuclear spin operator $\boldsymbol{I}$.

$$H_0 = H_{EZ} + H_{ZFS} + H_{HF} + H_{NZ} + H_{NQ}$$

$$= \frac{\beta_e B_0^T \bar{g} \boldsymbol{S}}{\hbar} + \boldsymbol{S^T} \bar{D} \boldsymbol{S} + \sum_{k=1}^{m} \boldsymbol{S^T} \bar{A}_k \boldsymbol{I_k} - \beta_n \sum_{k=1}^{m} \frac{g_{n,k} {B_0}^T \boldsymbol{I_k}}{\hbar} + \sum_{I_k > 1/2} \boldsymbol{I_k}^T \bar{P}_k \boldsymbol{I_k} \qquad (1.1)$$

Here, operators are bold, and tensors are marked with an overline. The first expression of this equation is the electron Zeeman interaction, which describes the splitting of the electron spin states in an outer magnetic field due to their different magnetic momentum. It is usually the largest term of the static spin Hamilton operator. The second term is only relevant in systems that possess a spin system with S > 1/2, because it corresponds to the zero field interaction that arises from dipolar interactions between multiple unpaired electrons of the same atom, e.g. electrons in neighboring d-orbitals of a transition metal. The third terms describes the so-called hyperfine interaction, which is the interaction between the electron spin and the nuclear spins of nuclei in proximity to the electron spin. The fourth and fifth term present the nuclear Zeeman interaction and the quadrupole interaction of the surrounding nuclei. The governing physical parameters of these interactions are the $\bar{g}$-Tensor of the electron spin, the zero field interaction tensor $\bar{D}$, the hyperfine tensor $\bar{A}_k$, the nuclear Zeeman interaction tensors and the

quadrupole interaction tensors $\bar{P}_k$. In this formula, β_e is the Bohr magneton, β_n is the nuclear magneton, and $\hbar$ is the reduced Planck constant. As shown here, the spin Hamilton operator describes one isolated spin center and its interaction with its immediate surroundings. However, large sections of this work deal with information that arises from the interaction of two or more spins. For the explanation of the resulting interaction, two different spins *A* and *B* that belong to different spin centers with an inter spin distance *r* are considered. For such a system, two different types of coupling must be considered. Firstly, for spins in close contact or for spins that are connected by conjugated orbitals, electron-electron exchange coupling *J* can be observed. This interaction results from weak orbital overlap, which leads to an exchange of spin density between the involved spin centers. The exchange coupling integral *J* can be given by the following expression:

$$J = 2e^2 \int \frac{\psi_A^*(r_A)\psi_B^*(r_B)\psi_A(r_B)\psi_B(r_A)}{|\vec{r}_A - \vec{r}_B|} dr_A dr_B \tag{1.2}$$

Here, e is the elementary charge, ψ and ψ^* are the binding and antibinding orbitals of the spins denoted by the subscript, and the r vectors denote the orientation vectors of the spin orbitals, which should not be confused with the inter spin vector, which is the difference between the orientation vectors. In this picture, the isotropic J coupling is then given as follows:

$$H_J = \bar{J}\boldsymbol{S_A S_B} \tag{1.3}$$

The J coupling is strongly dependent on the inter spin distance, and decays exponentially with increasing distance. The J coupling is often approximated as an isotropic interaction but it may have anisotropic components, which stem from spin-orbit coupling. Eq. 1.3 can be expanded to

$$H_J = \bar{J}\boldsymbol{S_{z,A} S_{z,B}} + \frac{1}{2}\bar{J}(\boldsymbol{S_{A,+} S_{B,-}} + \boldsymbol{S_{A,-} S_{B,+}}) \tag{1.4}$$

The two terms in Eq. 1.4 are called secular and pseudo-secular part of the exchange coupling, respectively. The latter term, which is the pseudo-secular part, is negligible if the magnitude of the exchange coupling is small compared to the difference of the resonance frequencies of the spins A and B. This condition is expressed in Eq. 1.5.

$$|\omega_A - \omega_B| = \Delta\omega \gg J \tag{1.5}$$

This case is called the weak exchange coupling regime. If the opposite condition is met, that is if the exchange coupling is large compared to the resonance difference, the pseudo secular part can no longer be disregarded. Eq. 1.6 expresses the condition for this case.

$$|\omega_A - \omega_B| = \Delta\omega \ll J \tag{1.6}$$

In such a case, the wave functions of the spins A and B mix, and the biradical is more accurately described as a delocalized triplet rather than two individual spins. Instead of the individual g-values and hyperfine coupling constants of the two radicals, the average of the two g-values is observed and hyperfine coupling constants are halved. This case is known as the strong coupling regime of the exchange coupling.

In between these cases, there is the complicated case where neither criterion is fulfilled.

$$|\omega_A - \omega_B| = \Delta\omega \approx J \tag{1.7}$$

For this so called intermediate coupling regime, the g-values and hyperfine coupling constants of the two spins are only partially merged and depend in a complex fashion on the ratio of the exchange coupling and the resonance frequency offset. For this condition, a quantitative treatment is very difficult and strongly dependent on the individual case.

In addition to this contact-based interaction, two spins will also show a distance and orientation dependent interaction of their respective magnetic momentums, the so-called dipolar coupling.

$$H_{dd} = \boldsymbol{S_A}\overline{D}_{dd}\boldsymbol{S_B} \tag{1.8}$$

The dipolar coupling is given by the above formula, where $\overline{D}_{dd}$ is the dipolar coupling tensor. It can be derived from the Hamiltonian for coupled magnetic point dipoles.

$$H_{AB} = \frac{\mu_0 g_A g_B \beta_e^2}{4\pi\hbar}\left[\frac{\boldsymbol{S_A}^T\boldsymbol{S_B}^T}{r^3} - \frac{3(\boldsymbol{S_A}^T\cdot r)(\boldsymbol{S_B}^T\cdot r)}{r^5}\right] \tag{1.9}$$

In this formula, μ_0 is the permeability of vacuum, g_A and g_B are the g-factors of the respective spins, and *r* is the inter spin vector of the spins A and B. From this expression, the so-called dipolar alphabet can be derived through inserting the appropriate quantum mechanical operators and simple mathematical transformations.

$$H_{AB} = \frac{\mu_0 g_A g_B \beta_e^2}{4\pi\hbar r^3}(A + B + C + D + E + F) \quad (1.10)$$

$$A = \boldsymbol{S_z^A S_z^B}(1 - \cos^2\theta)$$

$$B = -\frac{1}{4}(\boldsymbol{S_+^A S_-^B} + \boldsymbol{S_-^A S_+^B})(1 - \cos^2\theta)$$

$$C = -\frac{3}{2}(\boldsymbol{S_+^A S_z^B} + \boldsymbol{S_z^A S_+^B})\sin\theta \cdot \cos\theta \cdot e^{-i\varphi}$$

$$D = -\frac{3}{2}(\boldsymbol{S_-^A S_z^B} + \boldsymbol{S_z^A S_-^B})\sin\theta \cdot \cos\theta \cdot e^{-i\varphi}$$

$$E = -\frac{3}{4}\boldsymbol{S_+^A S_+^B}\sin^2\theta \cdot e^{-2i\varphi}$$

$$F = -\frac{3}{4}\boldsymbol{S_-^A S_-^B}\sin^2\theta \cdot e^{-2i\varphi}$$

Here, θ and φ are angles that define the orientation of the spin-pair relative to the outer magnetic field, $\boldsymbol{S_-}$ is the lowering operator and $\boldsymbol{S_+}$ is the raising operator. The dipolar coupling constant is defined as follows:

$$\omega_{dd} = \frac{\mu_0 g_A(\theta,\varphi) g_B(\theta,\varphi) \beta_e^2}{4\pi\hbar r^3} \quad (1.11)$$

If the dipolar coupling constant is much smaller than the resonance frequencies of the individual spins, the so-called non-secular terms C-F can be disregarded. If the difference between the resonance frequencies of the two spins is also much larger than the dipolar coupling constant, the B term can be neglected as well. This simplification is known as the high field approximation, as it is equivalent with the statement that the spins are quantized along the magnetic field. In the described case, the Hamilton operator for the dipolar coupling of the spins A and B can be expressed as

$$H_{AB} = \omega_{dd} S_Z^A S_Z^B (1 - 3cos^2\theta) \quad (1.12)$$

The circular coupling frequency for the spin pair A and B is therefore given by Eq. 1.9:

$$\omega_{AB} = \omega_{dd}(1 - 3cos^2\theta) \quad (1.13)$$

As is evident from Eq. 1.13, the actual value of the dipolar coupling for a given spin pair is a function of its orientation relative to the applied magnetic field as expressed by θ. For a large ensemble of spins without specifically introduced restrictions, all orientations are present in

proportion to the number of possibilities to realize a particular alignment. The resulting spectrum in the frequency domain is called the Pake doublet, and is shown below.

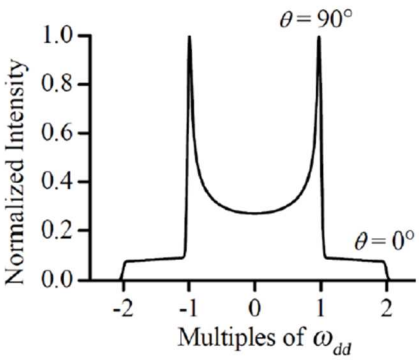

Figure 1: Pake doublet (taken from [25])

The Pake doublet has two characteristic points, which correspond to a spin alignment perpendicular to the B field ($\theta = 90^{\circ}$) and parallel to the B field ($\theta = 0^{\circ}$). They appear at the frequencies ω_{dd} and 2 ω_{dd}, respectively.

In analogy to the discussion of the weak and strong coupling case of the exchange coupling, a similar separation of different cases must be made for the dipolar coupling. If all the above conditions are met, the result is Eq. 1.13, which corresponds to the weak coupling regime. In this case, the perpendicular and the parallel components are shifted by the exchange coupling *J*. If the high field approximation is not fulfilled, the pseudo-secular term B of the dipolar alphabet must be taken into consideration. In that case, instead of Eq. 1.13, a 50 % larger value for the dipolar coupling constant is obtained.

$$1.5 \cdot \omega_{AB} = \omega_{dd}(1 - 3cos^2\theta) \qquad (1.13)$$

It should also be noted that the dipolar interaction is an anisotropic interaction, and vanishes if the rotation frequency of the spin system is faster than the dipolar frequency. For this reason, samples must be immobilized to measure the dipolar coupling constant. In EPR distance measurements, this is most often done by measuring in a frozen solution, although other methods like attaching the sample to a solid support or the use of highly viscous media have been also reported.[26]

1.2.2 *cw*-EPR

In order to understand how *cw*-EPR is utilized in distance measurements, it is necessary to first understand how the experiment works. As was already discusses in the previous section when the spin Hamiltonian was introduced, an (electron) spin in an applied magnetic field B will experience an energy splitting of its spin states, with the various contributions listed in Eq. 1.6, all adding to the exact magnitude of the splitting and the various resulting energy levels. For most organic radicals, the electron-Zeeman effect is the largest contribution, with the hyperfine coupling still noticeably contributing. Since all other contributions are very small or in fact zero for organic radicals with a spin of $S = 1/2$, the Hamiltonian can be written as

$$H_0 = \frac{\beta_e B_0^T g S}{\hbar} + \sum_{k=1}^{m} S^T A_k I_k \tag{1.14}$$

The g-value as well as the hyperfine tensor A can be anisotropic or isotropic depending on the symmetry of the electronic environment of the radical. Solving the Schrödinger equation for this shortened Hamiltonian will yield the eigenvalues of the spin system, or to put it more simply, yield the possible energy levels that a spin can populate. To illustrate that and to show how an EPR spectrum might look like, assume a spin system with a spin of $S = 1/2$ and a nuclear spin of $I = 1$. Possible examples of such systems are nitroxide radicals or carbon centered triarylmethyl radicals in the presence of a ^{13}C nucleus. In such a case, two energy levels are obtained initially due to the splitting of the $S = 1/2$, that then themselves split in three sublevels accrording to the possible values of $m_I = 1, 0, -1$. Thus, six distinguishable energy levels are obtained.

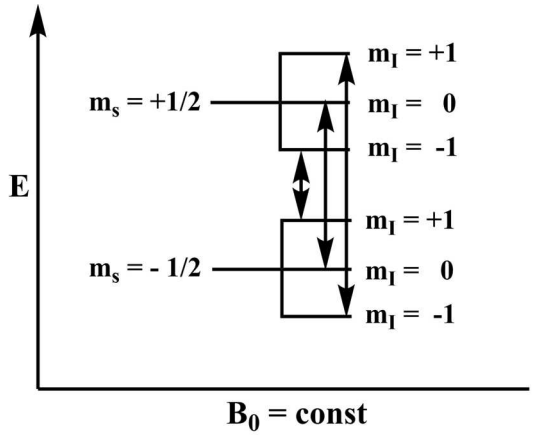

Figure 2: Energy level diagram of a spin system with S = ½ and I = 1

In a *cw*-EPR experiment, the sample is irradiated with microwaves to cause absorption following the selection rule $\Delta m_S = 1$ and $\Delta m_I = 0$. For the example spin system discussed here, that results in three distinct transitions that correspond to the condition $\omega_{mw} = \frac{g\beta_e B}{\hbar} + Am_I$. ω_{eff} is the angular microwave frequency, g and $\bar{A}$ are the g-value and hyperfine tensor. This is known as the resonance condition. In an actual experiment, the frequency is kept at a constant value and the magnetic field is linearly incremented. In addition, the field is modulated with a second, small magnetic field usually in the range of 0.1 to 5 G, so that instead of the microwave absorption, the first derivative is measured. These conditions are due to technical reasons, and also, measuring the change of absorption increases the sensitivity.

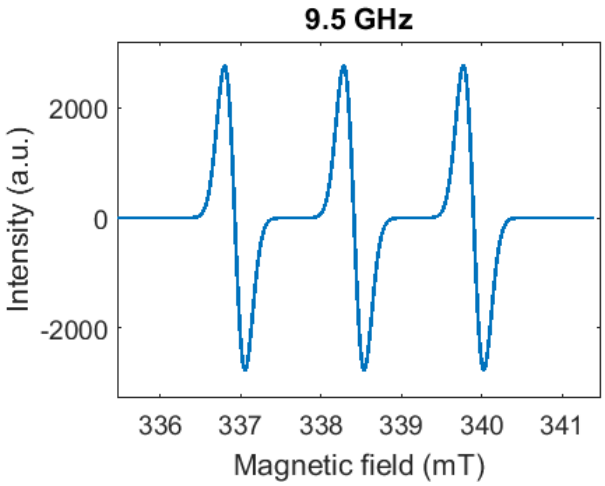

Figure 3: Simulated EPR spectrum of unbound MTSSL

An example of a nitroxide spectrum is provided in Figure 3. It is also important to remember that EPR is not a single molecule experiment, but that an ensemble of spins is measured, with usual spin concentrations on commercially available spectrometers, depending on the microwave frequency band, between 1 µM and 200 µM, although much higher concentrations are possible in *cw*-EPR experiments. In an unordered sample, all possible orientations of the spin relative to the magnetic field are present, and according to that, also all possible values of g and A are represented. The values also include slight variations of the magnetic field experienced by each spin due to its surrounding environment, e.g. solvent molecules or other dissolved components of the sample. This affects the relaxation times of the spin center, which in turn affects the lifetime of the observed spin states. The lifetime of the spin states cause a so-called homogenous broadening of the EPR lines. To this date, it is not possible to recover interactions smaller than the homogeneous broadening. An inhomogenous line

broadening may occur due to the anisotropy of the g-tensor and the A-tensor, but also due to unresolved hyperfine coupling constants.

1.2.3 Pulsed EPR

The information given here is primarily taken from a textbook by A. Schweiger and G. Jeschke.[23a]

The first fact to consider is that the electron is known to have an angular momentum that is quantized and proportional to the electron spin, from which a magnetic moment of $\mu = -g\beta_e S$ arises. In an ensemble of electrons, the macroscopic magnetic momentum equals the sum of all individual magnetic momentums. If a magnetic field is applied, the energy minimum at 0 K is realized when all spins are aligned parallel to this magnetic field. However, since the energy difference between the parallel and the antiparallel state is of the order of magnitude or smaller than thermal energies at non-zero temperatures, a state of thermal equilibrium will be realized. In this state, the spins precess individually around the magnetic field, but are slightly biased towards an orientation antiparallel to the magnetic field vector of the applied field. This causes the ensemble to have a non-zero magnetic momentum along the direction of the applied magnetic field. This so-called magnetization M_0 is given by the following equation:

$$M_0 = \frac{1}{V}\sum_{i=1}^{N} \mu_i \qquad (1.15)$$

Where V is the volume occupied by the spin ensemble and μ_i is the magnetic momentum of the spin *i*. The magnetization can be described as a single vector that is oriented along the outer magnetic field B_0. However, while the z-component of the magnetization is known and constant, the component in the x,y-plane is not determined. Therefore, the x,y-component of the magnetization vector changes constantly, which causes the magnetization vector to precess with an angle θ at a constant angular frequency ω_L, the so-called Larmor frequency.

$$\omega_L = \frac{g_e \beta_e B_0}{\hbar} \qquad (1.16)$$

A usual graphical representation of that process is a cone around an axis.

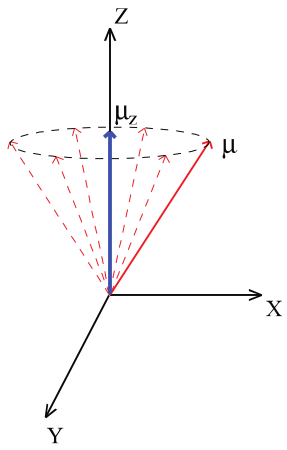

Figure 4: Precession of the magnetization vector along the outer magnetic field. (taken from [27])

If an additional field B_1 is applied in form of a microwave pulse in resonance with the Larmor frequency, meaning $\omega_{mw} = \omega_L$, the magnetization vector will precess around the axis along which the pulse is applied with a precession frequency of

$$\omega_1 = \frac{g_e \beta_e B_1}{\hbar} \tag{1.17}$$

Convenient descriptions of the effect of the mw-pulse on a spin assume a rotation frame, where the axis system rotates around the z-axis with the Larmor frequency. If such a system is in thermal equilibrium, the magnetization M is parallel to the z-axis, that is M = [0, 0, M_0]. If a pulse is applied along the x-axis, the magnetization is affected as follows:

$$M_x = 0 \tag{1.18}$$

$$M_y = -M_0 \sin(\omega_1 t_p) \tag{1.19}$$

$$M_z = M_0 \cos(\omega_1 t_p) \tag{1.20}$$

Where t_p is the duration of the mw-pulse. The product $\omega_1 t_p$ is also known as the flip angle β and gives the angle by which the magnetization vector rotates around the x-axis. As given here, the pulse will rotate the magnetization M in from the z-direction to the –y direction, but by introducing a phase shift of the microwave field of 90°, 180° or 270°, a rotation in –x, y, or x direction can also be achieved, while a rotation around the z-axis is realized by a combination of rotations around the x- and y-axis. Thus, it is possible to manipulate the magnetization in any direction via a combination of well-timed and phased microwave pulses. The equations are only valid if the resonance condition is fulfilled. If the microwave frequency is very different from the Larmor frequency, the spin system remains largely unaffected, since the flip angle decreases rapidly with increasing frequency offset. For small

frequency offsets, the axis of the precession of the spin system is no longer in the xy-plane, which is synonymous with introducing a second rotation around the z-axis. If the resonance offset $\Omega_1 \ll \omega_L$ is fulfilled, off-resonance effects are usually small enough to be neglected. So far, the given formulas indicate that once a spin ensemble is manipulated into a non-equilibrium state, it will remain there indefinitely. Obviously, that cannot be true, as it is possible to run an experiment repeatedly with the same result, indicating that the ensemble returned to its equilibrium state in between the experiments. Therefore, a mechanism or mechanisms must exist that allow the spin ensemble to shed the absorbed energy and return to its original state. The mechanistic details of these processes cannot be explained in a classical picture, since processes affecting the individual spin are involved, but a qualitative description of these so-called relaxation effects is given by the rotation frame Bloch equations.

$$\frac{dM_x}{dt} = -\Omega_1 M_Y - \frac{M_x}{T_2} \tag{1.21}$$

$$\frac{dM_y}{dt} = -\Omega_1 M_x - \omega_1 M_z - \frac{M_x}{T_2} \tag{1.22}$$

$$\frac{dM_z}{dt} = -\Omega_1 M_Y - \frac{M_x}{T_1} \tag{1.23}$$

The Bloch equations show that there are two processes that contribute to relaxation, one that shows the loss of magnetization in the x,y plane, which is connected to the time constant T_2, and one that describes the loss of magnetization along the z-axis and is connected by the time constant T_1. The former process is known as transversal relaxation, while the latter is known as longitudinal relaxation. In broad terms, and outside the classical interpretation, transversal relaxation encompasses all processes that change the angular momentum of the individual spins precessing in the x,y-plane, thereby disturbing the phase coherence between the spins and thus reducing the magnetization in that plane. Longitudinal relaxation means that the changes in the population of the spin states that were induced by the absorption of microwaves are reversed and the system returns to its thermodynamic equilibrium. Considering these effects, the magnetization caused by a microwave pulse after an evolution time t is given by

$$M_x(t) = M_0 \sin(\beta) \sin(\Omega_1 t) exp\ (-\frac{t}{T_2}) \quad (1.24)$$

$$M_y(t) = -M_0 \sin(\beta) \sin(\Omega_1 t) exp\ (-\frac{t}{T_2}) \quad (1.25)$$

$$M_z(t) = [1 - (1 - \cos\beta)]\ exp\ (-\frac{t}{T_1}) \quad (1.26)$$

The magnetization along the z-axis cannot be detected, but from a single pulse experiment arises a signal that is proportional to $M_y - iM_x$ which is described by

$$V(t) \propto \exp(i\Omega_1 t) \exp(-\frac{t}{T_2}) \quad (1.27)$$

This signal is known as a free induction decay (FID), and is the basis of most NMR experiments. However, for most electron spins, such an FID decays so fast that it vanishes within the dead time of the spectrometer, that is the time after an mw-pulse in which the spectrometer cannot detect a signal, and therefore most EPR experiments detect on so-called spin echoes instead. The most simple spin echo experiment was proposed in 1950 by E. L. Hahn [28] and consists of only two pulses, one with a 90° (or $\pi/2$) flip angle and the other with a 180° (or π) flip angle, separated by an evolution time τ. Assuming the mw-pulses are applied along the x-axis, the whole sequence reads as $\pi/2_x - \tau - \pi_x - \tau - echo$. The first pulse creates a magnetization in –y direction, thereby flipping the magnetization vector in the x,y-plane. The spins start to precess in the x,y-plane, but due to the slight differences of the magnetic field each spin experiences, the angular momentum of the spins differs. This means that the spins will spread out in the x,y-plane, which causes the magnetization to diminish and ultimately vanish. After the evolution time τ, all spins have precessed by a certain degree that calculates as $\omega_1\tau$. If a π-pulse is then applied, the sign of the precession is inverted, therefore the magnetization will increase again until it reaches its measureable maximum after a time equal to the first evolution time τ has passed. This maximum is referred to as a spin echo. It should be noted that for all the evolution, the spins are subject to transversal relaxation, which causes the echo intensity to be smaller the longer τ is, and that the echo intensity is always less than the original magnetization created by the $\pi/2$-pulse. In section 1.3.2, more complicated distance measurement experiments that employ the same principals for spin manipulation as the Hahn echo sequence will be discussed.

1.3 Distance measurement with EPR

1.3.1 cw-EPR Distance Measurements

The EPR line that is measured in the *cw*-experiment is the representation of a spin state that is defined by an electron spin quantum number and a nuclear spin quantum number. It also contains the various interactions that were discussed in section 1.2.1 and can be expressed as a superposition of all the interactions listed in Eq. 1.6. As such, all these interactions can be extracted from the EPR line, but they are often masked by line broadening due to the anisotropy of the A- and g-tensors. If this is the case, the they are not resolved, but contribute to the EPR linewidth. To measure the inter spin distance of two spins, the dipolar coupling constant can be determined via a fit of the increase in linewidth due to the dipolar coupling. However, this required knowledge of the EPR linewidth without dipolar coupling. This is usually determined via a reference sample that is equal to the investigated spin with the exception that it contains only one spin. If the dipolar coupling constant is larger than the linewidth of the EPR line, it is resolved in the spectrum and it can be fitted directly without previous knowledge of the linewidth.[29] The distances that can be measured depend on the linewidth of the spectrum of the observed spin. For nitroxides, a usual distance range is 1-2 nm, while for trityl radicals, measurements up to 2.5 nm have been reported.[29a] For longer distances, and for cases where many different lines are present in the *cw*-EPR spectrum, a number of pulsed techniques have been developed which will be discussed in the following section.

1.3.2 Pulsed EPR Distance Measurement Techniques

Pulsed EPR measurement techniques offer the distinct advantage over *cw*-EPR that they allow to separate the various contributions to the spin Hamilton operator. Where *cw*-EPR measures all contributions, that then need to be disentangled from the measured spectra, suitable pulse sequences allow to only record a specific interaction. For distance measurements, it is necessary to separate the dipolar coupling of the electron spins from other contributions. A number of sequences were developed to record the dipolar coupling between two different electron spin centers, enabling distance measurements for inter spin distances up to 16 nm.[7b, 30] The most common of these techniques is pulsed electron-electron double resonance (PELDOR)[8], a double frequency technique that has become widely popular and was successfully used for many biological applications.[7a] Beside PELDOR[8] exist a number of single frequency techniques, which have led a niche existence in the early days of pulsed EPR distance measurements, but received renewed interest in recent years due to advances in the spectroscopic equipment as well as the available spin labels. Most noteworthy are double quantum coherence (DQC)[31], single frequency technique for refocusing dipolar couplings (SIFTER)[32] and relaxation induced dipolar modulation enhancement (RIDME)[9]. Other techniques e.g. distance measurements based on changes of the longitudinal and transversal relaxation times, do also exist, but are irrelevant in the context of this work. The performance and challenges of the methods shown here are discussed in a number of review articles, although those articles focus on the use of these techniques in conjunction with nitroxide spin labels.[7a, 33]

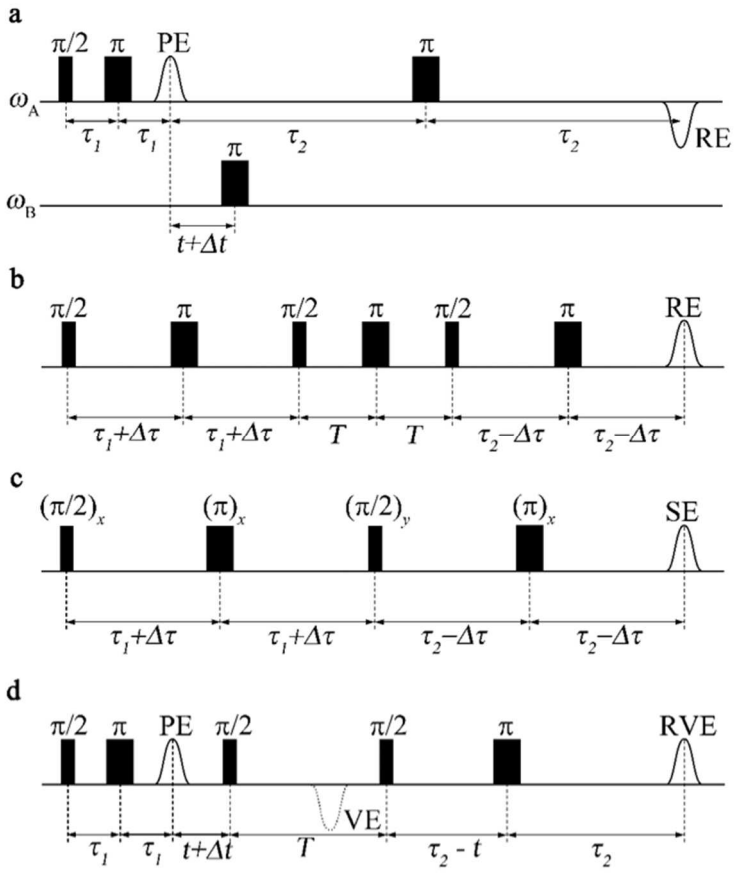

Figure 5: Pulsed EPR techniques for distance measurements (a) PELDOR (b) DQC (c) SIFTER (d) RIDME (taken from [25])

Figure 5 shows the pulse sequences of the four mentioned techniques. In the following subsections, all four techniques will be discussed.

1.3.3.1 PELDOR

The information given in this subsection is based on a number of textbooks and review articles.[7a, 23a, 33b, 34] The original PELDOR[8] experiment was proposed by Milov in 1981[35], but nowadays, the four pulse version is most widely used. Also, recent years saw the development of a five pulse version[36] as well as versions that implement adiabatic, coherent or composite pulses.[37] Here, only four pulse PELDOR will be discussed.

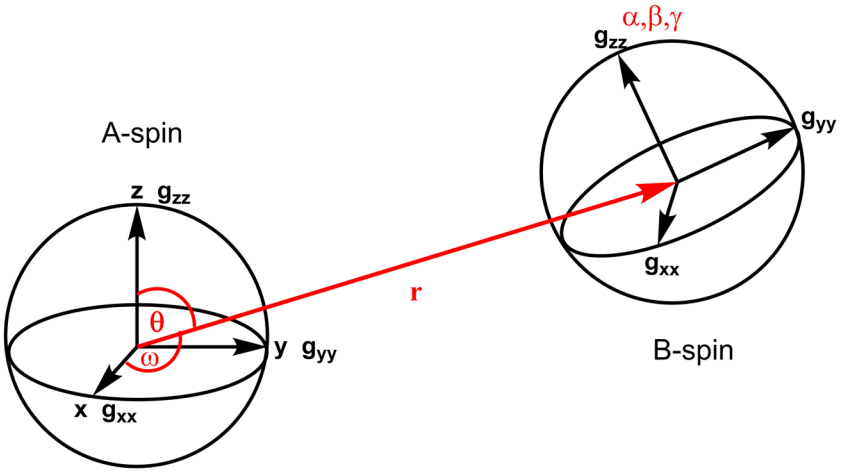

Figure 6: Geometric model of the spin pair A and B. Here, r is the inter spin distance vector, θ is the angle between the inter spin vector and the applied magnetic field, ω is the angle between the inter spin vector and the x,y-plane. The Euler angles α,β and γ give the orientation of the B spin relative to the A spin.

The PELDOR experiment is applied to a spin pair A-B, corresponding to the respective resonance frequencies ω_A and ω_B. By definition, ω_A is the detection frequency, and ω_B is the pump frequency. On the detection frequency, a three pulse sequence is applied that consists of a Hahn echo sequence and an additional π-pulse after a delay τ_2 after the echo. This leads to a so-called refocused echo at $2\tau_1$+$2\tau_2$. On the pump frequency, a π-pulse (or inversion pulse) is applied, which flips the B spin. If the spins A and B are coupled, this will induce a change in the precession frequency of the A spin by $\pm\omega_{ee}$, where ω_{ee} is the sum of the dipolar coupling ω_{AB} and the exchange coupling J between the spins A and B. As a result, the A spins will acquire a phase shift proportional to the time t at which the inversion pulse is applied. If t is linearly incremented, this phase shift is projected as a modulation of the intensity of the refocused echo as a function of t and the magnitude of the dipolar coupling constant.

$$V(t) = V_0 \cos(\omega_{ee} t) \tag{1.28}$$

The maximum intensity is achieved when the position of the inversion pulse coincides with the primary echo due to the first two pulses of the detection sequence. This is called the zero time. The intensity of the modulation is dependent on the portion of B spins that were inverted and is usually expressed by the modulation depth parameter λ, for which values of $0 < \lambda \leq 1$ can be obtained. The resonance frequency is dependent on the orientation of the spin pair relative to the applied magnetic field. Also, the spectral width of a spin is dependent on the g-anisotropy and existing hyperfine coupling constants. For these two reasons, the spectra of many commonly used paramagnetic species exhibit a greater width than possible excitations widths for commercially available spectrometers. A rectangular microwave pulse shows an

excitation bandwidth inversely proportional to its duration. The excitation bandwidth is given by Eq. 1.29.

$$\Delta\nu[MHz] \approx \frac{1.207}{t_p[\mu S]} \tag{1.29}$$

If the excitation bandwidth of the pulse is smaller than the spectral width of the spins, only a fraction of the spins correlating to a specific subset of orientations is excited, and therefore a modulation depth below one is achieved. The PELDOR signal is the product of two contributions, one arising from spins inside the same molecule, and the other from the multitude of spins in the surrounding media.

$$V_{PELDOR}(t) = V_{intra}(t) \cdot V_{inter}(t) \tag{1.30}$$

The intermolecular contribution V_{inter} is for a homogeneous sample can be described as a monoexponential decay and is easily removed during data analysis. The intra molecular signal that arises from the dipolar coupling of a single A-B spin pair is given as

$$V_{intra}(t) = V_0\{1 - \lambda[1 - cos(\omega_{ee}t)]\} \tag{1.31}$$

This expression can be expanded for an ensemble of N spins by summation of the contribution of each spin pair. For the case of a homogeneously distributed sample, such as a frozen solution or a powder, the orientation relative to the magnetic field can be taken as random and averaged accordingly.

$$V_{intra}(t) = \sum_{i=1}^{N} \int_0^{2\pi} \int_0^{\pi} V_{0,i}(\varphi,\psi) \left\{1 - \lambda_i(\varphi,\psi)[1 - \cos\left(\omega_{ee}^{i}(\varphi,\psi)t\right)]\right\} sin\varphi d\varphi d\psi \tag{1.32}$$

Where φ and ψ denote the polar angles which describe the orientation of the magnetic field in the laboratory coordinate framework. For the cases that the correlation of the orientation of the A and B spin can be neglected, the integration of the angles φ and ψ can be substituted by an integration over all θ angles with the probability density function $sin\theta$ and the sum over N can be instead expressed as the integral over the inter-spin distances with the probability density function D(r).

$$V_{intra}(t) = \langle V_0 \rangle \left\{1 - \langle\lambda\rangle \int_0^{\infty} D(r) \int_0^{\pi/2} [1 - \cos(\omega_{ee}(r,\theta)t] \cdot sin\theta d\theta dr\right\} \tag{1.33}$$

$\langle V_0 \rangle$ is the total echo intensity of all A spins at t = 0 and $\langle\lambda\rangle$ is the modulation depth parameter of the whole ensemble. The time trace that results from this signal can be transformed into the frequency domain via Fourier transformation, and from the resulting Pake pattern, the distance can be calculated. However, a much better approach is to determine the probability

function D(r) of the inter-spin distance, as it also contains information on the width of the distribution and, if several distances exist, their relative abundance. The probability density function D(r) can be obtained via Tikhonov regularization, a mathematical routine to solve ill-posed mathematical problems. This routine is implemented in the program DeerAnalysis[38].

1.3.3.2 RIDME

The RIDME experiment is, in a sense, a derivative of the PELDOR sequence for the case that $T_{1,A} \gg T_{1,B}$. As was described above, the PELDOR sequence employs two different frequencies and achieves a modulation of the time trace with the dipolar coupling constant by inverting the B spin. The RIDME experiment uses the fact that a spin will spontaneously flip its orientation given enough time. As was described already for the PELDOR experiment, this flip will induce a phase shift in the coupled A spin which contains the dipolar information. The original three-pulse RIDME experiment and its four-pulse successor were proposed by Kulik et al.[39]. It is based on the observation that in electron spin echo envelope modulation (ESEEM,[40]) experiments that are usually performed to get information about the nuclei in the environment of the electron spin, the dipolar coupling is also visible. The experiment was expanded to its current five-pulse version by M. Huber et al.[9], which is also shown in Figure 5d. The advantage of the five-pulse RIDME sequence is that it is dead time-free. The first two pulses are the classical Hahn echo sequence and give rise to a primary echo at the time $2\tau_1$. After an evolution time t, a $\pi/2$ pulse is applied, which shifts the spins and their acquired phases into the x,z-plane, where they evolve for a time T that is much longer than the T_2, which causes the x-component to vanish due to relaxation. Also, the third pulse gives rise to a so-called virtual echo at a time $2(\tau_1 + t)$, although this is not an echo in the classical sense as its describes a spin ensemble which`s transversal relaxation dephases during the time t. The fourth pulse shifts the magnetization back into the x,y-plane and creates a stimulated echo. The last π-pulse refocuses both the stimulated and the virtual echo. Both contain the complete dipolar information, but since the refocused virtual echo allows for shorter phase evolution times after the last pulse, it is generally considered to give a better signal to noise ratio and cause less distortions for small values of t. The time trace is recorded as a function of t, therefore it is important to have the greatest possible accuracy for small t values, as this will be the values near the zero time. The dipolar information is acquired during the evolution time T, during which spontaneous relaxation events cause an inversion of the B spin. The inversion probability is given by

$$\lambda = \frac{1}{2}\left(1 - exp\left\{\frac{T}{T_1}\right\}\right) \tag{1.34}$$

Where T_1 is the longitudinal relaxation time of the B spin. This shows that the longer T is, the greater is the probability for an inversion of the B spin, however, since relaxation events of the A spin as well as other effects that destroy the magnetization have to be considered, it is not possible to increase T unlimitedly. Just like the PELDOR experiment, the RIDME time trace is composed of the product of intra- and intermolecular contributions.

$$V_{RIDME}(t) = V_{intra}(t) \cdot V_{inter}(t) \tag{1.35}$$

While exact mathematical descriptions exist for the background of the PELDOR experiment, the RIDME background is much more complex and strongly dependent on the individual sample. It is usually fitted with stretched exponentials or polynomial functions.[9, 41] In addition, due to its origin in the ESEEM experiment, the time trace may contain ESEEM modulations if there are nuclei with a nuclear spin unequal zero in the vicinity of the electron spin center. Methods to remove this are described in the literature.[9, 42] An example is to record two timetraces, where one has a separation T much smaller than T_1, so that no dipolar modulation occurs, while the other has a sufficiently long T separation for dipolar modulation to occur, but uses otherwise the same parameters as the first timetrace. The second timetrace is than divided by the first timetrace to remove the ESEEM modulation. The same general idea is used when the experiment is conducted twice at two different temperatures with otherwise identical parameters. The timetrace recorded at the higher temperature is then devided by the timetrace recorded at the lower temperature. Alternatively, one can perform the experiment at a frequency band where the ESEEM modulation of the surrounding nuclei is suppressed. An example is the suppression of proton-ESEEM at Q-band frequencies.

The mathematical description of the signal that arises from a single spin pair and by extension that of an ensemble N is very similar to the PELDOR experiment. The ensemble is described by

$$V_{intra}(t) = \sum_{i=1}^{N} \int_0^{2\pi} \int_0^{\pi} V_{0,i}(\varphi,\psi)\left\{1 - \sum_k \sum_l \lambda_{kl}(\varphi,\psi)[1 - \cos\left(\omega_{ee}^{i,kl}(\varphi,\psi)t\right)]\right\} sin\varphi d\varphi d\psi \tag{1.36}$$

The expression is almost identical with Eq. 1.32 Here, the modulation depth parameter λ_{kl} arises as the product of the probability of the spin B corresponding to the spin projection m_k and the probability of changing it during the time interval T to the projection m_l. Or, to put it less sophisticated, the probability that the spin B is in an excited state at the beginning of the

time interval T and relaxes during that period. If the orientations of the A and B spin are not or only weakly correlated, the sum over the orientations can be expressed via a probability density function.

$$V_{intra}(t) = \langle V_0 \rangle \left\{ 1 - \sum_k \sum_l \lambda_{kl}(\varphi, \psi) \int_0^\infty D(r) \int_0^{\pi/2} [1 - \cos(\omega_{ee}(r, \theta)t] \cdot sin\theta d\theta dr \right\} \tag{1.37}$$

If the inversion efficiency can be expressed by a single modulation depth parameter λ, this expression is the same as the expression given for the PELDOR experiment in Eq. 1.33 and the probability density function for the inter-spin distances can be determined via Tikhonov regularization. For pairs of spins with $S = 1/2$, equation 1.31 holds true. For spin states $S > 1/2$, higher harmonics must be considered, and an explicit treatment of the modulation depth parameters for each transition must be taken into account. A more detailed discussion of the RIDME experiment is given in an excellent review by Astashkin et al.[43].

It should also be noted that while in the above discussion it was implied that the RIDME experiment was designed for two different spins with strongly different longitudinal relaxation times, this is no strict requirement. The experiment works best if the above mentioned case is fulfilled, but it was demonstrated that the experiment also works for equal spins. In that case, the evolution time T should be of equal length to the longitudinal relaxation time T_1, since this was shown to be the best compromise between modulation depth and signal-to-noise ratio.[41]

1.3.3.3 DQC

The double quantum coherence experiment for EPR distance measurement was first calculated and later successfully introduced by J. H. Freed in 1997 and 1999.[31, 44] A complete description of the experiment is not possible outside the density operator formalism, but a description in these terms exceeds the scope of this manuscript. Instead, a more qualitative description of the idea behind the experiment will be given. The first expression that needs to be clarified in order to grasp the DQC experiment is the term ‘coherence’. An explanation according to G. Jeschke and A. Schweiger`s book will be given here.[23a] Suppose a quantum mechanical spin exits in a two level system with the states α and β. If an EPR experiment is performed on a large ensemble of such spins, the result will be the expectation value of the observables corresponding to these spin states, which in a classical picture would mean the obtained magnetization vectors in x, y and z direction. While this can only hold true if at the

time of the experiment each spin exists either in the state α or β, the indeterminacy principle dictates that before the experiment, that is in the absence of an observer, the spin exists in a superposition of either states and with a corresponding wave function ψ and the respective phases ϕ_α and ϕ_β.

$$|\psi\rangle = c_\alpha|\alpha\rangle + c_\beta|\beta\rangle = \exp(i\phi_\alpha)\cdot(|c_\alpha||\alpha\rangle + \exp(-i\Delta\phi)\cdot|c_\beta||\beta\rangle \quad (1.38)$$

If the phase difference $\Delta\phi = \phi_\alpha - \phi_ß$ is identical for all spins of the ensemble, this is called a coherence. Therefore, a coherence is the coherent superposition of the eigenstates of a given spin ensemble. Coherences are categorized in zero, single, double order according to the net change of the quantum numbers of the transition associated with the coherence. Usually, higher order transitions need not be considered. In a zero quantum coherence, the net change is 0, in a single quantum coherence, the net change is 1, and for a double quantum coherence, the change is 2. Note that only single quantum coherence is associated with an observable and is closely related to the concept of transversal magnetization in the classical picture. In addition, zero and double quantum coherences correspond to forbidden transitions, but may be created by suitable pulse sequences. For a pair of coupled $S = 1/2$ spins A and B, a double quantum coherence can be created by the sequence $\pi/2 - \tau - \pi - \tau - \pi/2$, which gives

$$\sigma_2^{DQ} = -\sin(\omega_{ee}\tau)(2S_x^A S_y^B + 2S_y^A S_x^B) \quad (1.39)$$

Here, $S_{x,y}^{A,B}$ describes quantum mechanical operators that express the x and y components of the spin properties of the spins A and B, respectively. We need not further concern ourselves with these operators, but only to remember that the dipolar information is preserved in a double quantum coherence and that it is modulated by the product of the separation τ and the coupling constant ω_{ee}. The six-pulse DQC sequence is shown in Figure 5b. It can also be written as $\pi/2$- τ_p - π - τ_p- $\pi/2$-τ_2-π - τ_2 - $\pi/2$-$(\tau_m - \tau_p)$ - π - $(\tau_m - \tau_p)$ – echo, where $\tau_p = \tau_1$ and $\tau_2 = \tau_m - \tau_p$. The first three pulses of the sequence create the double quantum coherence as was discussed above. However, mw-pulses that create a double quantum coherence in an ensemble of spins also creates zero quantum coherence. The fourth pulse therefore functions as a quantum filter that refocuses the double quantum coherence and disperses the zero quantum coherence. Since double quantum coherence is not connected to an observable, it has to be converted to single quantum coherence. To this end, the fifth pulse converts the double quantum coherence to antiphase coherence, which naturally evolves into single quantum coherence due to the difference of the precession speed of the different spin

packets. The single quantum coherence is refocused to a detectable echo by the last pulse. In this sequence, τ_p is varied (it does not matter whether one starts from a large value and decrements or from a small value and increments) while τ_m is kept constant, keeping the complete length of the sequence constant. The experiment is then measured as a function of $\tau_\xi = \tau_m - 2\tau_p$ in the interval $-\tau_m$ to τ_m with its zero time at $\tau_m = 2\tau_p$. This leads to a modulated time trace which can be expressed as a probability density function and analyzed via Tikhonov regularization as was demonstrated for RIDME and PELDOR. For ideal pulses, the arising signal is given by the following expression.[23a]

$$V_{DQ}(\tau_p, \tau_m) = \frac{1}{2}\left[\cos(\omega_{ee}(\tau_p - \tau_m)) + \cos(\omega_{ee}(\tau_p + \tau_m))\right] \quad (1.40)$$

Note that for the ideal case, no modulation depth parameter is included in this description, because the double quantum coherence is only created if the spins do couple. Therefore, such a factor must equal one and is omitted. A particular challenge of this experiment is that it consists of a multitude of pulses and specifically aims at the excitation of forbidden coherence pathways. Because of this, the described result of the pulse sequence is only one of the many things that will happen to the spin ensemble if the presented sequence is applied. To eliminate unwanted contributions, the experiment is applied with a 64-step phase cycle. Only the double quantum coherence pathway remains, which is also the reason that experimental DQC data usually has a modulation depth of 95 % or higher. A small deviation from the theoretical 100 % modulation depth can arise from intermolecular double quantum coherences.

1.3.3.4 SIFTER

The SIFTER experiment is based on the solid echo sequence $\pi/2_x - \tau_1 - \pi/2_y - \tau_1 - echo$. The solid echo sequence is designed to completely refocus the magnetization of a system of coupled spins, which is usually not possible due to instantaneous diffusion. Instantaneous diffusion occurs because the spatial arrangement of a spin A is generally not identical to a second spin A$^{'}$ of the same resonance frequency. In other words, the angle and distance to adjacent spins is different between the spins A and A$^{'}$. This causes the two spins to have the same resonance frequency, but not the same dependency of their respective local magnetic fields on an applied microwave field. This causes the spins to correspond to different resonance frequencies after a microwave pulse was applied. This disperses some of the magnetization in a diffuse, that is, in a not directed way. Note that the difference is calculable for a single spin pair of known respective spatial arrangements, and gains the

diffuse character only through the observation of an ensemble, where all manners of combinations of distances and angles can randomly occur. By applying a $\pi/2_y$-pulse, the electron-electron coupling of the spins is refocused which eliminates instantaneous diffusion for small systems and reduces it for large networks of coupled electron spins. The SIFTER sequence expands the sequence by two additional pulses and varies the pulse separation times to achieve a modulation of the solid echo with the dipolar frequency. The full sequence is shown in Figure 5c. In the experiment, the amplitude of the solid echo is recorded as a function of the difference of τ_1 and τ_2. The sequence refocuses all inhomogeneties and all interactions to the solid echo regardless of this difference except the dipolar coupling. A treatment within the density operator formalism reveals that the $\pi/2_y$ – pulse does refocus the dipolar coupling, but as a function of the evolution time τ_1. The dipolar coupling is refocused as antiphase coherence which evolves during the evolution time τ_2 into single quantum coherence, therefore the final signal is a function of both evolution times.

$$V(\tau_1, \tau_2) \propto \cos(\omega_{ee}(\tau_1 - \tau_2)) \tag{1.41}$$

The observable part of the arising spin expression is given in equation 1.41. The experiment is similar to the previously described DQC sequence and has been called an allowed transition based variety of the same experiment. As such, it also requires a complete excitation of the spin system and a 16-step phase cycle to isolate the desired contributions of the experiment. Especially incomplete excitation is known to cause incomplete refocusing of interactions other than the dipolar coupling, which gives rise to modulations that are not connected to the inter-spin distance but cannot be distinguished in the analysis of the data. To assure complete excitation of the spin ensemble, the use of broadband pulses has been recently suggested.[45]

1.4 Site directed spin labeling

The distance measurement techniques described in chapter 1.3 offer a large variety of options to obtain distances between two electron spins. However, many biological relevant macromolecules like proteins and nucleic acids do not contain spin centers. Even if they do, as is the case with a number of metalloproteins, they usually contain only one spin center. Examples for such proteins are *pseudomonas aeruginosa* azurin, which contains a copper(II) center, or *pseudomonas putida cytochrome CYP101*, which contains a hemin group with an iron(III) center. Another prominent example is hemoglobin, the oxygen transporting protein of the vertebrates, and similar proteins for other kinds of animals. To gain structural information on a protein, it is therefore necessary to introduce spin centers into the biomolecule. Nowadays, a combination of site directed mutagenesis and small organic radicals, so-called spin labels, that specifically bind to a certain structural motif or functional group is regularly used.[46] This approach was first introduced in 1989 by W. L. Hubbell et al.[47] and is known as site directed spin labeling. The original procedure targets the thiol functional group in cysteine amino acids. The most commonly used class of spin labels are nitroxide radicals. These have been used for EPR studies of biological structures since 1965[48] and their most prominent representative, the MTSSL (methane thiosulfonate spin label), was introduced in 1982.[49] While this kind of spin labels have been successfully used on a large variety of structures and continue as the most widely used spin labels today, they have some shortcomings that prompted the development of new kinds of spin labels. A critical issue of EPR distance measurements is that they are usually performed in a frozen buffer solution, and therefore under conditions that greatly differ from the natural conditions under which biological structures exist. To overcome this, efforts are made to perform measurements at conditions closer to biological conditions, e.g. measurements at room temperature or in living cells. For these purposes, classical nitroxide labels are ill suited, since they are rapidly reduced to EPR-silent, diamagnetic species under in cell conditions[14, 50] and exhibit short relaxation times at room temperature, which prevents EPR-based distance measurements at this temperature. Recent years saw the development of new, sterically shielded types of nitroxide labels[51], which show both increased stability towards reducing conditions and longer relaxation times. Another type that has gained a lot of interest are gadolinium(III) based spin labels. Gadolinium(III) is the thermodynamically most stable state of gadolinium by a large margin and therefore it is resistant to any redox environment that a biological sample may survive. In the early days of gadolinium(III) spin labeling, a major

problem of these spin labels was their high cytotoxicity, but new gadolinium spin labels solved that problem by binding the metal in a chelate complex. In cell distance measurements were successfully performed with this kind of label.[14] An issue that exists with these gadolinium labels is that they are very fast relaxing as well, and therefore cannot be used for the room temperature EPR-based distance measurements. A third option that has gained increasing traction in the last decade are triarylmethyl radicals (trityls). The basic structure that is used for this kind of spin labels, the finland radical, was proposed in 1998[52] and is specifically designed to achieve long relaxation times and high persistence. The synthesis of trityl based spin labels has been a major challenge, but several working labels have been put forward.[13a, 26a, 53] These labels show long relaxation times at room temperature[54] and have been successfully used in room temperature distance measurements on immobilized nucleic acids.[26a]

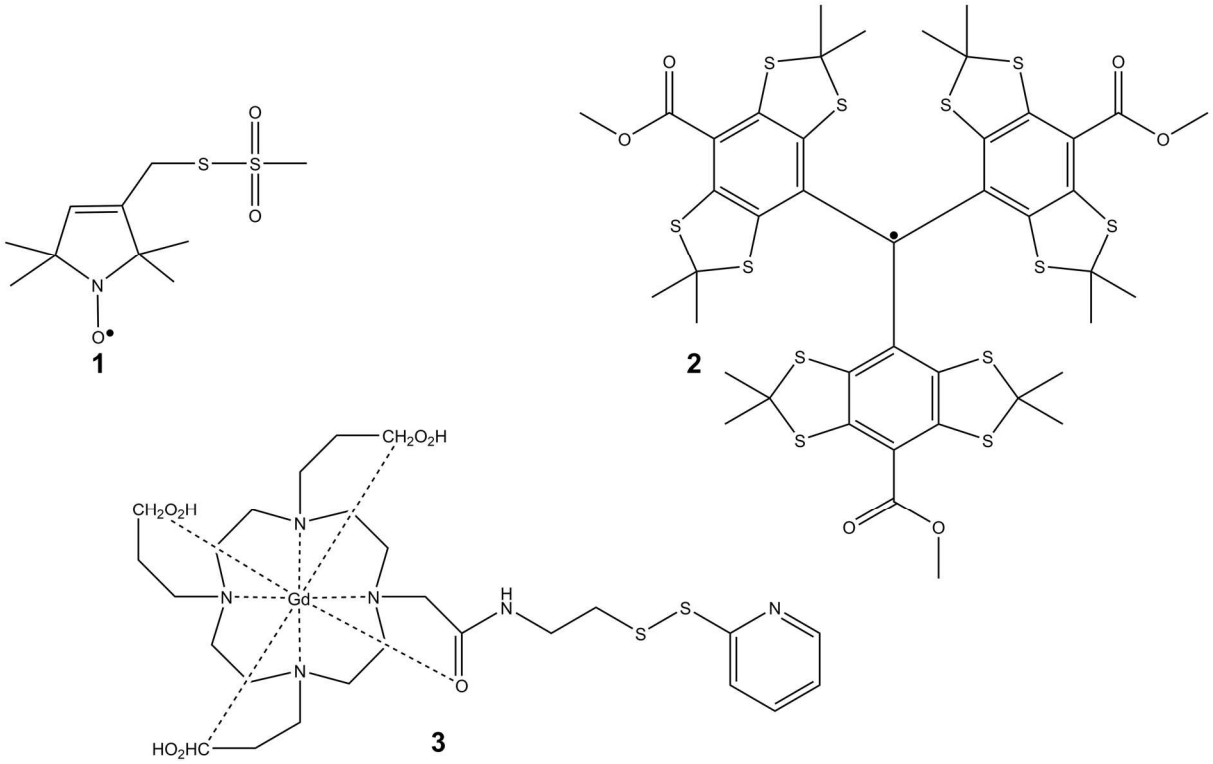

Figure 7: Chemical structures of MTSSL (**1**), a trityl radical (**2**) and a Gd(III)-complex spin label (**3**)

Most known spin labels, regardless of their class, use the methane thiosulfonate functional group to attach to proteins. This group rapidly forms disulfide bonds with offered thiol groups and therefore binds to cysteines. While this is a good approach for in vitro measurements on proteins that carry only a small number of cysteins, it poses several challenges. Firstly, a disulfide bridge is easily cleaved, making this kind of bonding strategy unsuitable for in cell measurements. Secondly, if a protein carries lots of cysteines, or some functional cysteines

that are important for the protein structure, this strategy requires either extensive mutagenesis or flat out fails. For those cases, different binding strategies have been proposed. Examples include the introduction of unnatural amino acids that carry an azide group or an alkyne or iodine group, or reactions that prompt the binding to a cysteine as a thiol ether. Azide groups can undergo click reactions to bind to alkyne carrying spin labels[55], while alkynes and iodine can undergo palladium catalyzed coupling reactions.

1.5 Electron Transfer Processes and Marcus Theory

Electron transfer is defined as the relocation of an electron from an atom or molecule to another such entity. Such reactions play an important role for many kinds of biological processes, e.g. photosynthesis[56] or the mitochondrial electron transport chain.[57] They are also key steps in a good number of organic and metal organic chemical reactions, such as Birch-reduction[58] and titanocene catalyzed epoxide opening reactions[59], and many more. For this reason, they have been thoroughly investigated and theoretically analyzed, with a major breakthrough in the understanding of electron transfer reactions in the in the 1950s and 1960s, when Henry Taube put forward experiments to demonstrate the formation of complexes as a prerequisite for electron transfer reactions.[60] This ultimately lead Rudolph A. Marcus to propose his elegant theory for electron cross reactions.[20b, 61] Despite these early successes, electron transfer reactions have such a ubiquitous appearance that they remain an interesting field of study even today. [20a, 62] As a well-established field of research, there is an abundance of literature that presents and elaborates on the Marcus theory. In the following, the outlines of the theory will be presented based on a number of standard textbooks. [63] When discussing electron transfer, it is useful to distinguish between two types of mechanisms, the inner-sphere and the outer-sphere mechanism. In an outer-sphere reaction, an electron is transferred between two reactants without breaking or building new bonds, so no major disturbances of their bonding or coordination sphere occur. In an inner-sphere reaction, the electron transfer proceeds via a shared ligand, and usually involves at least a temporary change in the binding and coordination sphere of the reactants. Inner-sphere reactions occur predominantly in metal organic complexes, and are not relevant in the scope of this work. To understand outer-sphere reactions, it is best to first consider electron self-exchange reaction. An electron self-exchange is an electron transfer where the products of the reactions are indistinguishable from the educts. A common example is the electron self-exchange of $[Fe(OH)_6]^{2+}$ and $[Fe(OH)_6]^{3+}$.

$$[Fe(H_2O)_6]^{3+} + [Fe(H_2O)_6]^{2+} \rightleftharpoons [Fe(H_2O)_6]^{2+} + [Fe(H_2O)_6]^{3+}$$

Figure 8: Electron self-exchange of hexaaqua iron-complexes

In such a reaction, the reactants join in a weakly coupled complex.

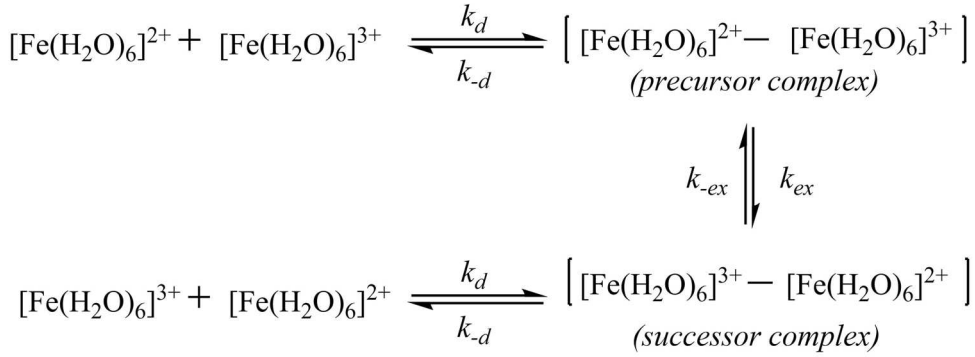

Figure 9: Mechanism of the electron self-exchange for the example of hexaaqua iron-complexes

In the precursor complex, the donor- and acceptor-orbitals must overlap to a sufficient extend to give a tunneling probability that is appreciably larger than zero. In such a case, the Franck-Condon principle can be invoked, which state that electron transitions are so fast that they take place in a static nuclear framework, meaning that during the transition, no bond length or dihedral angle changes. Staying with the example of the hexaaqua iron-complexes, this means that if iron(II) transfers an electron in its equilibrium configuration, this would mean that the resulting iron(III) complex would be in an elongated state. At the same time, an iron(III) complex at its equilibrium state to which an electron is transferred will turn into an iron(II) complex in a compressed state. The only situation in which an electron can be transferred without violating the Franck-Condon principle is when both complexes achieved a state of equal nuclear configuration through vibration. If changes of the nuclear configurations are represented as displacements along the reaction coordinate, the point where this condition is fulfilled is the intersection of the parabolic electron potentials of the two reactants.

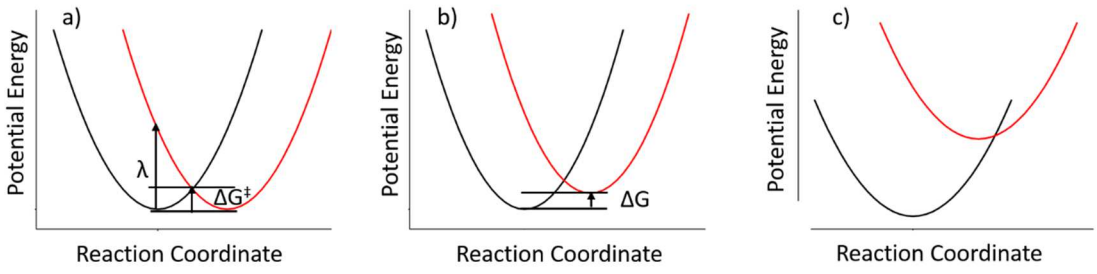

Figure 10: Potential curves for electron self-exchange (a), electron transfer reactions (b) and electron transfer reactions in the Marcus inverted region (c)

The difference in the nuclear configuration of the reactants therefore determines the reaction rates. The quantitative relation is given by the Marcus equation.

$$k_{ET} = \upsilon_N \kappa_c \cdot \exp(-\Delta G^{\ddagger}/RT) \tag{1.42}$$

Here, k_{ET} is the rate constant for an electron transfer reaction. The pre-exponential factor consists of the nuclear frequency factor υ_N, which gives the frequency with which the reactants form a precursor complex in solution in the event that they collide, and the electronic factor κ_c which gives the probability that an electron transition occurs upon the formation of a precursor complex. It is dependent on the lifetime of the precursor complex and the tunneling probability of the electron, which in turn depends on the orbital overlap of the electron-donor and –acceptor orbital. $\Delta G^{\ddagger}$ is the free enthalpy of the transition state. According to Marcus Theory, it is given by the following equation:

$$\Delta G^{\ddagger} = \frac{\lambda}{4}\left(1 + \frac{\Delta G}{\lambda}\right)^2 \tag{1.43}$$

Here, λ is the reorganization parameter which is the energy required to move the nuclei of the reactant to the position they adopt in the product immediately before the electron transfer. ΔG is the free enthalpy of the reaction, and is for an electron self-exchange by definition zero, since an electron self-exchange is a dynamic equilibrium. For an electron self-exchange reaction it follows that $\Delta G^{\ddagger} = \frac{\lambda}{4}$ is always fulfilled. If the picture is expanded from the self-exchange to cases where new molecules or ions that are different from the educts are formed through the transfer of an electron, ΔG does not equal zero. This changes the speed of the electron transfer as indicated in Figure 10b and c. With increasing driving force, the speed of the electron transfer increases, until the point is reached where the potential curves intersect at the minimum of the potential curve of the electron donor. At this point, ΔG equals the reorganization energy. A further increase in the free enthalpy will cause the intersection of the potential curves at an above minimum energy level of the electron donor, and the rate of the electron transfer decreases. This is called the Marcus inverted region.

The above explanations show that Marcus theory can be used to predict the rate of an electron transfer between reactants of the same species based on a small number of thermodynamic constants. It can also be used to predict the reaction rate for an electron transfer between different species. One of the most striking postulates of Marcus Theory is that every outer-sphere electron transfer can be expressed as the average of the self-exchange processes of each reactant. This gives rise to the Marcus cross relation

$$k_{12} = (k_{11}k_{22}K_{12}f_{12})^{1/2} \quad (1.44)$$

Here, k_{12} is the rate constant of the mixed electron transfer of the species 1 and 2, K_{12} is the equilibrium constant that can be derived from the free enthalpy of the reaction, and k_{11} and k_{22} are the self-exchange rates of the two reactants. The factor *f* is a unitless factor that is 1 for small values of ΔG, but decreases for large values of ΔG. It accounts for the fact that the free enthalpy of the transition state is not linearly proportional to the free enthalpy of the reaction.

1.5.1 EPR-detection of electron self-exchange

As is evident from the previous explications, the knowledge of electron self-exchange rate constants is essential in applying Marcus theory to model all kinds of electron transfer processes, e.g. charge transfer processes.[64] Unfortunately, the methods available to determine these important constants are limited. A possible example for the indirect measurement is magnetic field effect on reaction yield-spectroscopy (MARY). From the magnetic field dependence of the excimer fluorescence intensity, it is possible to deduce the rate constant k_{ex}. [65] A different method that can be employed for special cases of enantiomeric transition-metal complexes, are stopped-flow experiments.[66] A method that can be routinely used for the determination of electron self-exchange rates between paramagnetic species is the monitoring of line broadening effects in an EPR spectrum.[67] Since the method was first reported in the late 1950s, a good number of papers have been published on that subject.[68] In the following paragraph, a short overview of the relevant theory will be given.

Suppose a system of a radical ion species Q* and its correspondent neutral, non-radical form Q. In such a system, the rate of the electron self-exchange is given by eq. 1.45.

$$v = k_{ex}[Q^*][Q] \quad (1.45)$$

Here, [Q] and [Q*] denote the concentration of the species Q and Q*. According to literature, the ratio of the concentration of the radical ion to the concentration of the neutral species is equal to the ratio of the lifetimes τ_{Q^*} and τ_Q of the corresponding spin configurations.[69]

$$\frac{[Q^*]}{[Q]} = \frac{\tau_{Q^*}}{\tau_Q} \quad (1.46)$$

From this follows that the rate is also given as the ratio of the concentration of either species and its respective lifetime.

$$v = \frac{[Q^*]}{\tau_{Q^*}} = \frac{[Q]}{\tau_Q} \tag{1.47}$$

Combining eq. 141 and eq. 1.39, one gets:

$$\frac{1}{\tau_{Q^*}} = k_{ex}[Q] \tag{1.48}$$

Therefore, the lifetime of the spin configurations are proportional to the concentration of the neutral compound, and therefore to the amount of neutral substance that was added. Adding more of the neutral compound will shorten the lifetime of a given spin configuration, and will lead to a broadening of the EPR line corresponding to it. Provided that two neighboring ERP lines do not influence each other, that is, the change of their linewidth due to electron self-exchange is much smaller than the difference of their resonance frequencies, the line broadening can be expressed as:

$$\Delta\omega = \frac{1}{\tau_0} + \frac{1}{\tau_{Q^+}} \tag{1.49}$$

Where $\Delta\omega$ is the total line broadening, and τ_0 is the natural lifetime of the spin state without electron self-exchange. It can also be written in the classical first derivative form more common in EPR.

$$\Delta\omega = \frac{\sqrt{3}}{2}\gamma_e \Delta B_{pp}^0 + \frac{1}{\tau_{Q^*}} \tag{1.50}$$

Combining eq. 1.48 and 1.50 yields

$$\Delta B_{pp} = \frac{(1-p_i)k_{obs}}{\pi \cdot \sqrt{3}\gamma_e}[Q] + \Delta B_{pp}^0 \tag{1.51}$$

Here, ΔB_{pp} is the peak-to-peak linewidth of the self-exchange broadened EPR signal, γ_e is the gyromagnetic ratio of the free electron, p_i is a statistical population factor of the EPR line i that considers collisions of equal spin states. All distinct EPR lines correspond to a specific nuclear spin configuration, and an exchange between molecules of an equal total nuclear spin quantum number does not affect the EPR linewidths. An electron can transfer to a molecule with any nuclear spin configuration with equal probability. In a very well resolved spectrum, an individual factor and an individual line broadening can be calculated for each line, taking into account the different populations of the individual nuclear spin configurations. In many real applications, spectra are not as well resolved and all configurations are assumed to be equally populated. In such a case, the statistical factor is equal to the inverse of the total

number of distinct EPR lines, and the self-exchange rate is calculated from the average line broadening as a function of the concentration of the neutral compound.[68a, 69-70]

The equations provided here show how the observed electron exchange rate k_{obs} can be calculated from a linear plot of the linewidth against the concentration of neutral compound. However, as is evident from Figure *9*, the association and dissociation of the precursor complex as well as the diffusion of the molecules influences the speed of the electron self-exchange, and contributes to the observed rate constant. Based on the reaction scheme shown in that figure, a simple set of differential equations can be established to calculate a correction for this effect.

$$\frac{1}{k_{ET}} = \frac{1}{k_{obs}} - \frac{2}{k_d} \tag{1.52}$$

Eq. 1.52 shows the diffusion correction derived from this treatment.[70b]

2 EPR distance measurements on organic triarylmethyl radical (trityl) model compounds and biological macromolecules

2.1 Introduction

As was discussed in the general introduction, EPR has emerged as a powerful tool to determine distances between two spin centers. In organic model compounds, two radicals are attached to each other with a linker. Such model compounds are used to develop protocols to measure distances between specific combinations of spin centers. These protocols are employed for measurements on biological structures, such as proteins or oligonucleotides.[46] These kind of molecules may contain naturally occurring spin centers, often metal centers.[71] More often, spin centers are introduced in form of small organic radicals, so-called spin labels. A general introduction to spin labels and site directed spin labeling was given in chapter 1.4. In this chapter, the application of various distance measurement techniques for the determination of trityl-trityl distances in bistrityl model compounds is demonstrated and discussed in terms of SNR and the found distributions. Then, the characterization of newly synthesized trityl spin labels and their application in the measurement of a trityl-Fe(III) distance in *pseudomonas putida* cytochrome CYP101 P450 both *in vitro* and *in cells* is presented.

2.2 Comparative study of different EPR distance measurement techniques on bistrityl model compounds

The synthesis of the discussed model compounds and preliminary EPR measurements were also included in the bachelor thesis of Sebastian Spicher.

Triarylmethyl radicals have emerged as a new kind of spin probe during the last two decades, ever since the basic structure of all currently used trityl species, the finland radical, was proposed.[52] Their main characteristics include a narrow spectral width and comparatively long relaxation times[17], which made them a focus of research aimed at room temperature distance measurements by means of pulsed EPR.[72] Apart from that, their EPR linewidth is strongly dependent on the oxygen concentration of the surrounding medium, which led to their application in oximetry.[73] In addition, they can be used as pH sensors and for imagine in biological tissue.[74] The performance of trityl radicals in various distance measurements techniques has been studied on a number of model compounds e.g. by the groups of Prisner and Schiemann,[13b, 29a, 75] but all these studies focused on a certain section of the available distance measurement techniques. Here, a study that applies PELDOR, RIDME, SIFTER and DQC is presented.

To this end, rigid model compounds were synthesized by Sebastian Spicher (see Figure 11 and Figure 12)

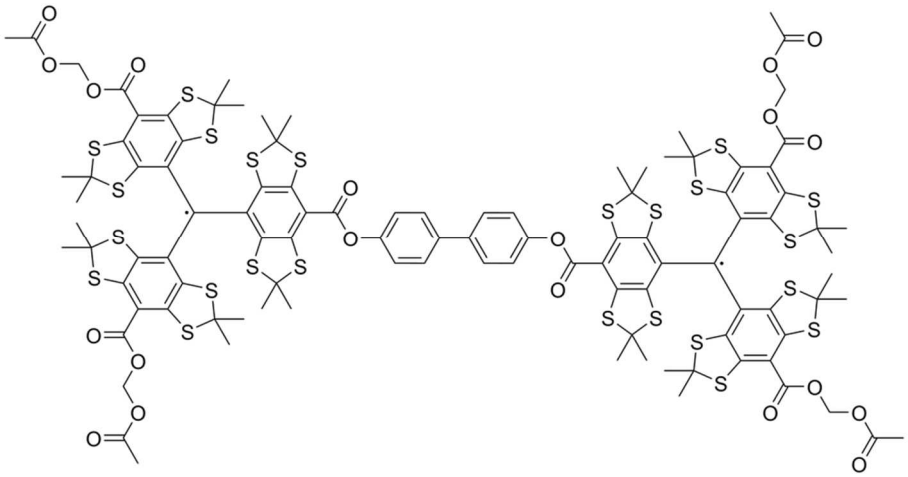

Figure 11: Bistrityl model compound **4**

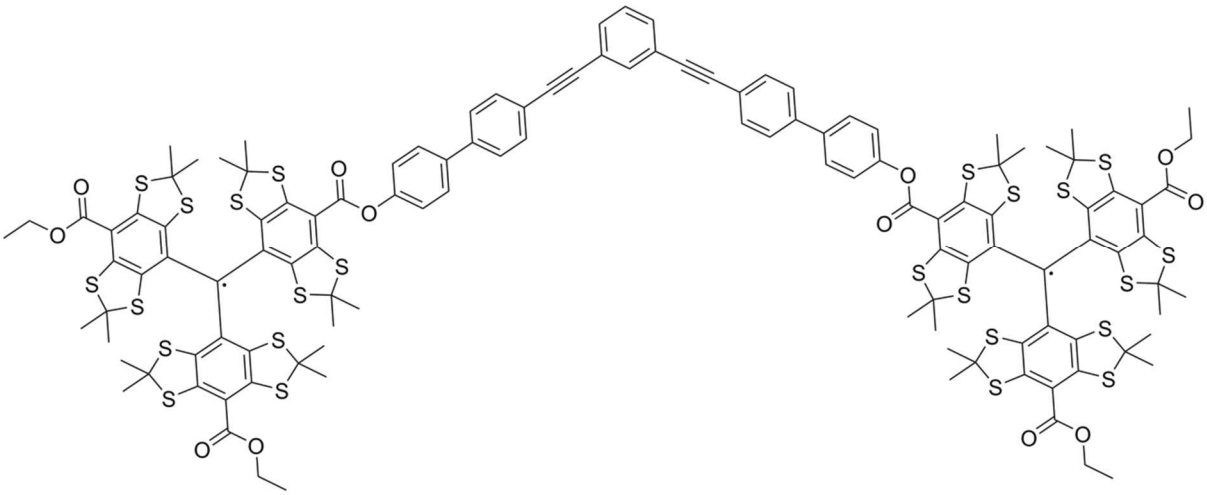

Figure 12: Bistrityl model compound **5**

The two model compounds were estimated based on DFT geometry optimizations (see appendix C) to have an inter spin distance of 2.2308 nm and 3.6106 nm, respectively. Compound **4** consists of two trityl radicals connected by a short biphenyl linker. Such a compound can be expected to be very rigid, which will lead to a long-lived dipolar modulation in the timetraces of EPR distance measurement techniques.[23a] However, the short inter spin distance combined with the linear alignment of the radicals may lead to a large *J* coupling constant. In addition, the short inter spin distance leads according to eq. 1.11 to a large calculated value for the dipolar coupling constant ω_{dd} of 4.7 MHz, since it is proportional to the inverse cube of the inter spin distance. On the other hand, it was previously discussed in section 1.4 that trityls were selected as spin labels among other reasons for their narrow spectral width. It can be as small as 1 G or approx. 2.8 MHz.[76] As was discussed in section 1.2.1, this may lead to a violation of the high field approximation, and coupling in the strong or intermediate coupling regime may have to be considered. From eq. 1.13 follows that in case of strong coupling a 50 % larger dipolar coupling constant will be determined. If the distance distribution is calculated from this value using Tikhonov regularization, a mean distance of only 87 % of the actual inter spin distance is obtained. Therefore, if dipolar coupling in the strong dipolar coupling regime occurs, a mean distance of 1.9408 nm should be obtained. Compound **5** shows a longer inter spin distance which corresponds to a calculated dipolar coupling constant of 1.1 MHz. At this distance, coupling in the strong coupling regime is not expected. Since *J* coupling is even stronger dependent on the distance between the spins, it is also unlikely to contribute significantly. However, the angular structure of **5** makes it more flexible than **4**, and broader distance distributions are expected as well as a stronger dampening of the dipolar modulation.

2.2.1 *cw*-EPR of **4** and **5**

As a first step towards the EPR distance measurements of the two bistrityl model compounds, they were characterized by means of X-band *cw*-EPR. To assure that no saturation effects distort the recorded spectra, power plots were measured for both compounds and the optimal power determined.

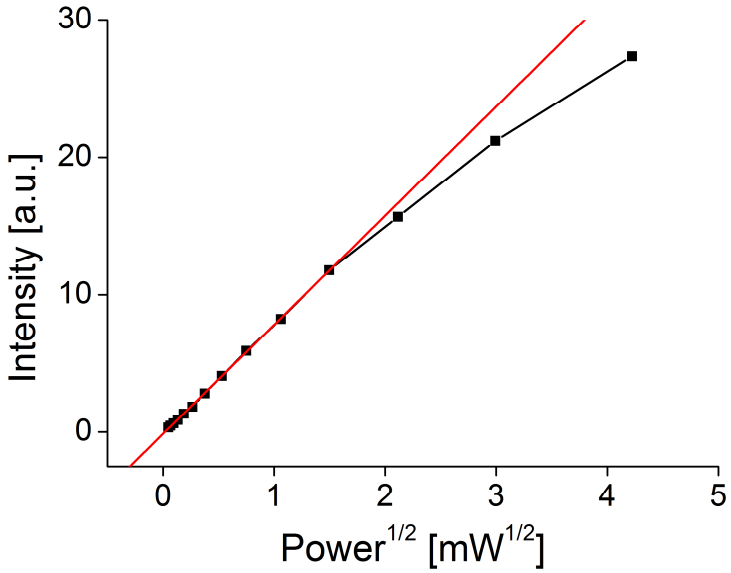

Figure 13: Power plot of **4** at X-band and room temperature

Table 1: Data of the power plot of **4** at room temperature

Intensity [a.u.]	**Power [mW]**	**Power$^{1/2}$ [mW$^{1/2}$]**	**Attenuation [dB]**
17.8	4.22	27.3	10
8.95	2.99	21.2	13
4.48	2.12	15.7	16
2.24	1.50	11.8	19
1.123	1.059	8.23	22
0.561	0.749	5.90	25
0.282	0.531	4.07	28
0.141	0.376	2.81	31
0.0706	0.266	1.84	34
0.0354	0.188	1.34	37
0.0178	0.133	0.879	40
0.00891	0.0944	0.641	43
0.00447	0.0669	0.455	46
0.00224	0.0474	0.331	49

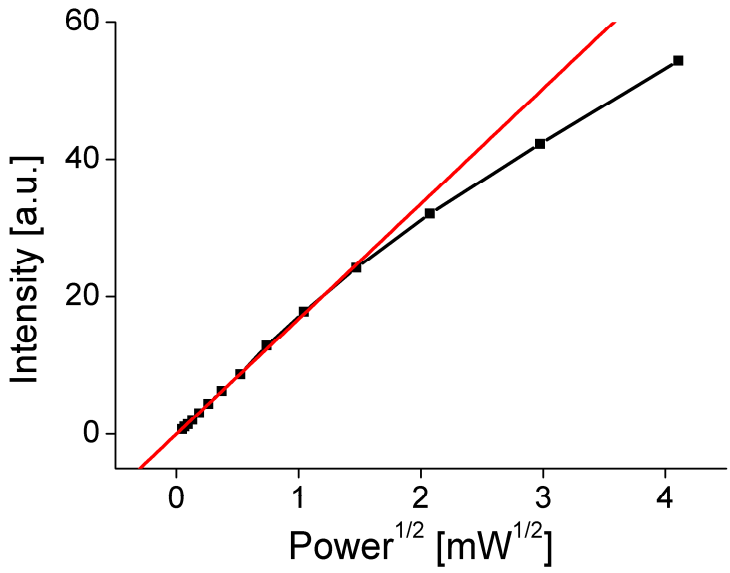

Figure 14: Power plot of **5** at X-band and room temperature

Table 2: Data of the power plot of **5** at room temperature

Intensity [a.u.]	**Power [mW]**	**Power$^{1/2}$ [mW$^{1/2}$]**	**Attenuation [dB]**
54,339	4.22	27.3	10
42,234	2.99	21.2	13
32,07	2.12	15.7	16
24,19	1.50	11.8	19
17,806	1.059	8.23	22
12,853	0.749	5.90	25
8,7035	0.531	4.07	28
6,2539	0.376	2.81	31
4,4007	0.266	1.84	34
3,0613	0.188	1.34	37
2,0577	0.133	0.879	40
1,4206	0.0944	0.641	43
1,0787	0.0669	0.455	46
0,70856	0.0474	0.331	49

The power plots show a linear proportionality of the signal intensity to the square root of the microwave power in the absence of saturation. When the transition is saturated, the intensity increase is lower than the linear progression would predict. Figure *13* and Figure *14* show near identical saturation behavior of **4** and **5**. Both compounds show no or negligible saturation at 1.5 mW microwave power, but do saturate at powers above that value.

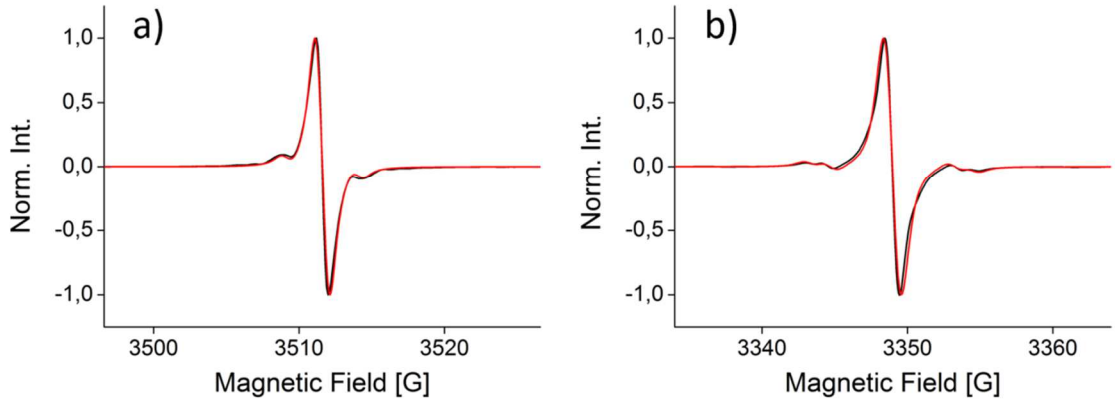

Figure 15: X-band cw-EPR spectra (black) and Easyspin simulation (red) of **4** (a) and **5** (b)

Table 3: Spectroscopic parameters of **4** and **5**

Sample	g-value	lwpp [G]	HFC ^{13}C [MHz]	HFC ^{13}C [MHz]
4	2.0032	0.73	13.5	-
5	2.0034	1.06	31	24

The spectra recorded of the two model compounds are shown in Figure 15, the spectroscopic parameters as determined by simulation in Table 3. It is immediately obvious that there is a strong difference between the HFCs obtained for **4** and **5**. Also, the peak-to-peak linewidth of **4** is 0.33 G smaller than the linewidth of **5**. This is noteworthy inasmuch that for isolated trityls, similar HFCs are obtained with only little influence of the substitution pattern of the respective radicals.[13b, 27, 76-77] As was discussed above and in section 1.2.1, *J* coupling in the strong coupling regime is likely to occur in **4**, and such a biradical is better described as a delocalized triplet. In that case, the hyperfine interaction is also delocalized and the HFCs are halfed. Comparing the obtained spectra, it is of course obvious that the HFC that was used in the simulation of **4** is not the exact half of either of the two HFCs obtained for **5**. However, two HFCs are resolved in the spectrum of **5**, while for **4**, only one was resolved. It is a reasonable assumption that instead of one resolved HFC, the superposition of two HFCs was obtained. The half of the mean of the HFCs found for **5** is 13.75 MHz. The value obtained for **4** is slightly smaller than this value. This can be interpreted in two ways. Either it is assumed that the small deviation from the exact half value is due to minor uncertainties in the simulation, or it is assumed that the values are correct as obtained. In the former case, this is indicative of strong coupling regime *J* coupling, in the latter case, this indicates an intermediate coupling regime. Either interpretations suggest that for subsequent distance

measurements on **4,** the pseudo-secular terms of the electron-electron interaction must be taken into account. This is consistent with the previously provided reasoning.

Building on the above results, it was an attempt was made to determine the inter spin distances of **4** and **5** by means of *cw*-EPR. The general approach for this kind of experiments was outlined in section 1.3.1.

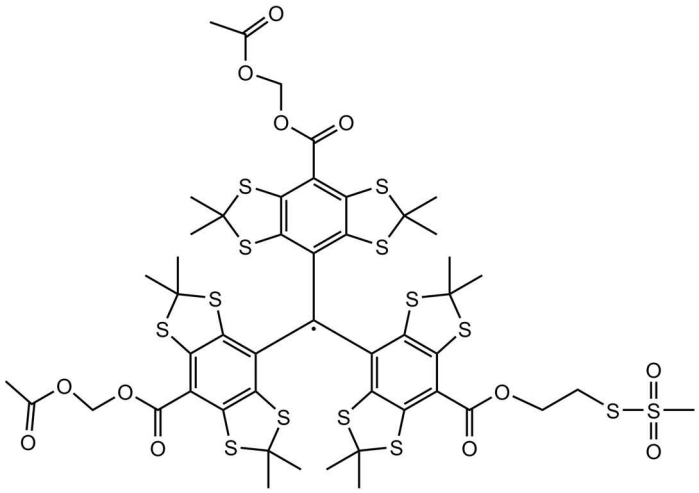

Figure 16: Chemical structure of compound **6**

As a reference for the line width in the absence of electron-electron coupling, compound **6** was chosen. The reason for this choice is the great similarity of the chemical structures of the trityl bodies of **4** and **6**. It was especially important that the reference has no open carboxyl groups, since it was assumed that the acidic proton adds another resolvable HFC which is absent in the model compounds. Experiments that confirm this will be discussed in section 2.3. In order to exclude contributions of oxygen to the line width, samples of **4**, **5** and **6** were degassed prior to the measurements as described in the method section (appendix A.I)

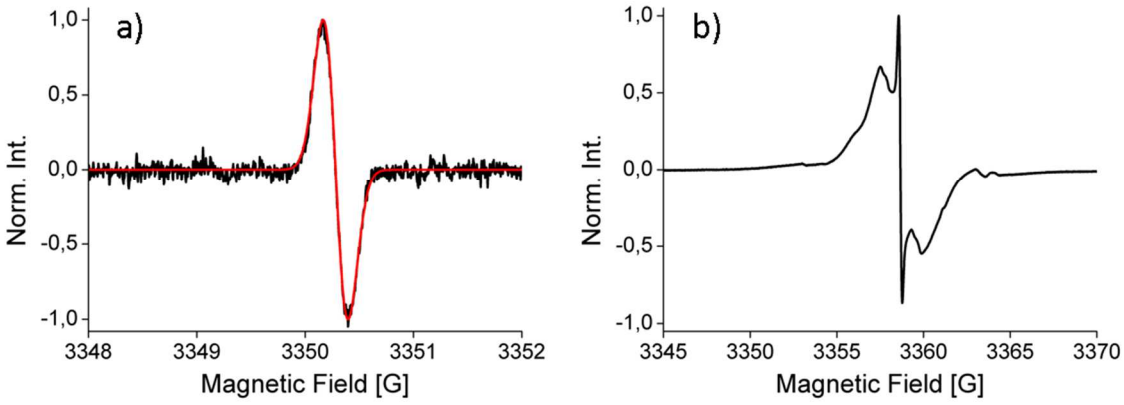

Figure 17: X-band cw-EPR spectrum of **6** (black, a) and its Easyspin simulation (red). X-band cw-EPR spectrum of **4** at 50 K (b)

The *cw*-EPR spectrum of **6** is shown in Figure 17. Simulation via Easyspin revealed a peak-to-peak linewidth of 0.23 G and an isotropic g-value of 2.0029. HFCs are not resolved but were taken to be equal to the HFCs determined for **5** for the sake of simulations. These values were chosen rather than the values obtained for **4** because the monoradical **6** cannot exhibit *J* coupling. The low temperature *cw*-EPR spectrum of **4** (see Figure 17) shows a significantly broadened spectrum with a peak-to-peak linewidth of 2.5 G. This is a significant increase relative to the value obtained for the reference compound, which is due to the fact that in a solid state, the dipolar interaction does not average out. The spectrum shows distinct shoulders, which indicate a partial resolution of the Pake pattern. However, the spectrum also shows a sharp line in the center with a peak-to-peak linewidth of 0.22 G. To determine the relative amount that this sharp signal contributes to the overall spectrum, its double integral was determined as 0.03686 arbitrary units as well as the double integral of the entire spectrum as 7.19096 arbitrary units. For the determination of the intensity of the sharp central line, the spectrum was integrated between the field values of 3358.19 G and 3359.24 G. The integration shows that this sharp line accounts for 0.5 % of the total signal intensity. The most probable explanation is that the recorded spectrum shows the superimposed spectra of two radical species. The first species, which accounts for most of the signal intensity, is **4**. The other species has a g-value and line width consistent with an isolated trityl. It can therefore be surmised that it is a leftover from the synthesis of **4**.

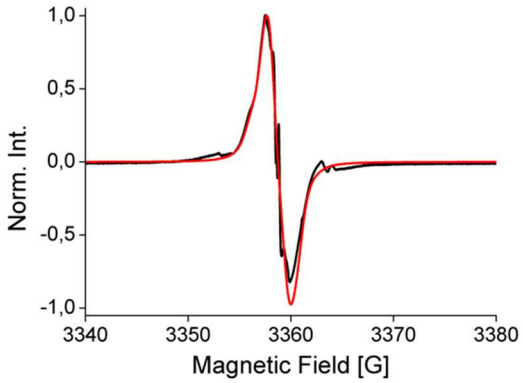

Figure 18: Spectrum(black) and simulation(red) of the cryogenic temperature cw-EPR spectrum of **4** after the removal of the impurity signal.

To obtain the spectrum of **4**, the spectrum of the impurity signal was simulated on the assumption that it would behave like the reference **6** and subtracted from the experimental data. The result was simulated using the spectroscopic parameters of **6** under additional inclusion of the electron-electron coupling. (see Figure 18) The simulation gave a value for the dipolar coupling of 7 MHz and a *J* coupling of 12 MHz. The found dipolar coupling

constants corresponds to a distance of 1.9532 nm. However, it was already demonstrated that the spins are not in the weak coupling regime, and a 50 % larger dipolar coupling constant will be obtained, or a distance value of 87% of the actual inter spin distance. Taking this into account, the measured dipolar coupling constant corresponds to a distance of 2.2451 nm, which is in excellent agreement with the expected distance. It should be considered though that this result was obtained using a large amount of previous knowledge of the system. Had the inter spin distance not been known from theoretical calculations, there would have been an ambiguity to what distance the obtained dipolar coupling constant corresponds to. In this specific case, DFT calculations, determined HFCs and the dipolar coupling constant form a consistent picture, but none of the results can stand without the support of the other two. This shows that *cw*-EPR requires very good data and ideally a fully resolved Pake pattern to give unambiguous results.

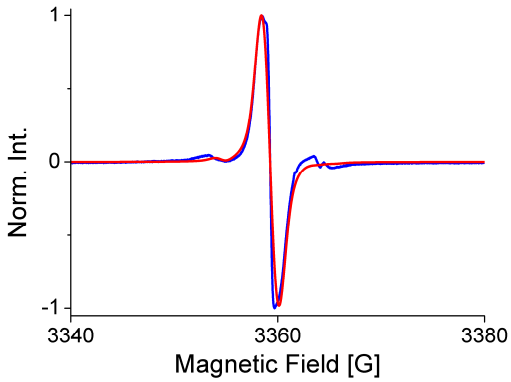

Figure 19: Spectrum (blue) and simulation (red) of the cryogenic temperature cw-EPR spectrum of **5**

In order to determine the inter spin distance of **5**, a cryogenic temperature spectrum was measured following the exact same procedures previously employed for **4**. However, the spectrum showed only minimal broadening, which does not allow assigning a specific value for the dipolar coupling constant. The attempt to determine the inter spin distance of **5** via *cw*-EPR was therefore aborted.

2.2.2 PELDOR of **4** and **5**

After the completion of the *cw*-EPR characterization, this study will continue to present the application of pulsed distance measurement techniques. It should be noted that while the *cw*-EPR experiments were performed at X-Band, the pulsed experiments were performed at Q-band. The main advantage of this is the significant increase of signal-to-noise ratio due to the higher population difference between the spin states. The most widely used pulsed technique for EPR distance measurements is the PELDOR sequence, also known as DEER.[8] The experiment is described in detail in the introductory section of this work, but for this section it is important to keep in mind that the PELDOR is a pump-probe experiment where one spin is monitored via echo detection while a different spin is inverted via a microwave pulse. Commonly, the detection spin is referred to as the A spin, while the inverted spin is referred to as the B spin. For the proper function of the experiment, it is necessary to excite the two spin independently of each other. This requirement does not pose a complication for nitroxide radicals, which regularly exhibit spectral widths of roughly 60 G or 180 MHz at X-band frequencies. At the same frequency band, the average width of the main transition of a trityl spectrum is no more than 3 G wide.[27] At Q-band, this is issue is reduced, with a larger total width of close to 7 G or about 20 G if the full width of the signal arising from ^{13}C-statellites are also considered. In MHz, this is 19.8 MHz and 56.6 MHz. However, on most regions of the spectrum, there is only very low signal intensity, which makes them unsuitable for the PELDOR experiment.

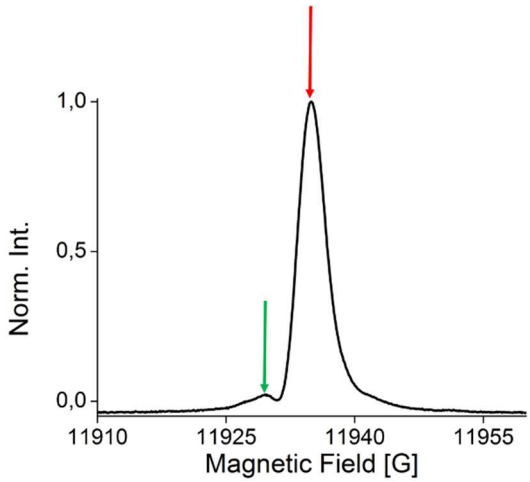

Figure 20: Pump-Probe scheme of the PELDOR experiment. The red arrow denotes the field position of the pump-pulse, the green the field position of the detection sequence.

To achieve a maximal modulation depth, it is important that a large number of spins are inverted by the pump pulse, therefore it is beneficial to set the pump pulse to the maximum of

the trityl spectrum. In order to avoid pulse overlap, the detection sequence must be applied to the outer fringes of the spectrum, that is, the signal arising from the ^{13}C-satellites. The pump-detection scheme is shown in Figure 20. Even at this positions, the separation of the two pulses is no more than 5 G. To avoid the aforementioned pulse overlap, the excitation width of the microwave pulses must be considered.

$$\Delta\nu[MHz] \approx \frac{1.207}{t_p[\mu S]} \tag{2.1}$$

As can be seen from the above equation, the excitation width of a pulse is inversely proportional to its length. [23a] Since a difference in the magnetic field of 1 G converts to a difference in the frequency domain of about 2.8 MHz, , the frequency separation of the A-spin and the B-spin for the given case is about 15 MHz. Based on that, a π-pulse length of 64 ns and an inversion pulse of 64 ns was chosen. This corresponds to an excitation width of 18.85 MHz. This appears to be a contradiction to the previous statement that pulse overlap should be avoided, but in fact is not if the excitation profile of a standard rectangular pulse is also considered.

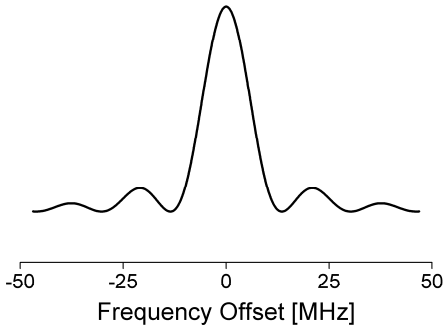

Figure 21: Example of the excitation profile of a rectangular microwave pulse.

The excitation profile of a rectangular microwave pulse is shown in Figure 21. The larger the frequency deviates from the nominal frequency at which the pulse is applied, the less it affects the magnetization of the spins it is applied to. As a result, the overlap at the outlying frequencies affected by the pulse is not critical, since the effect on the spins can be neglected.

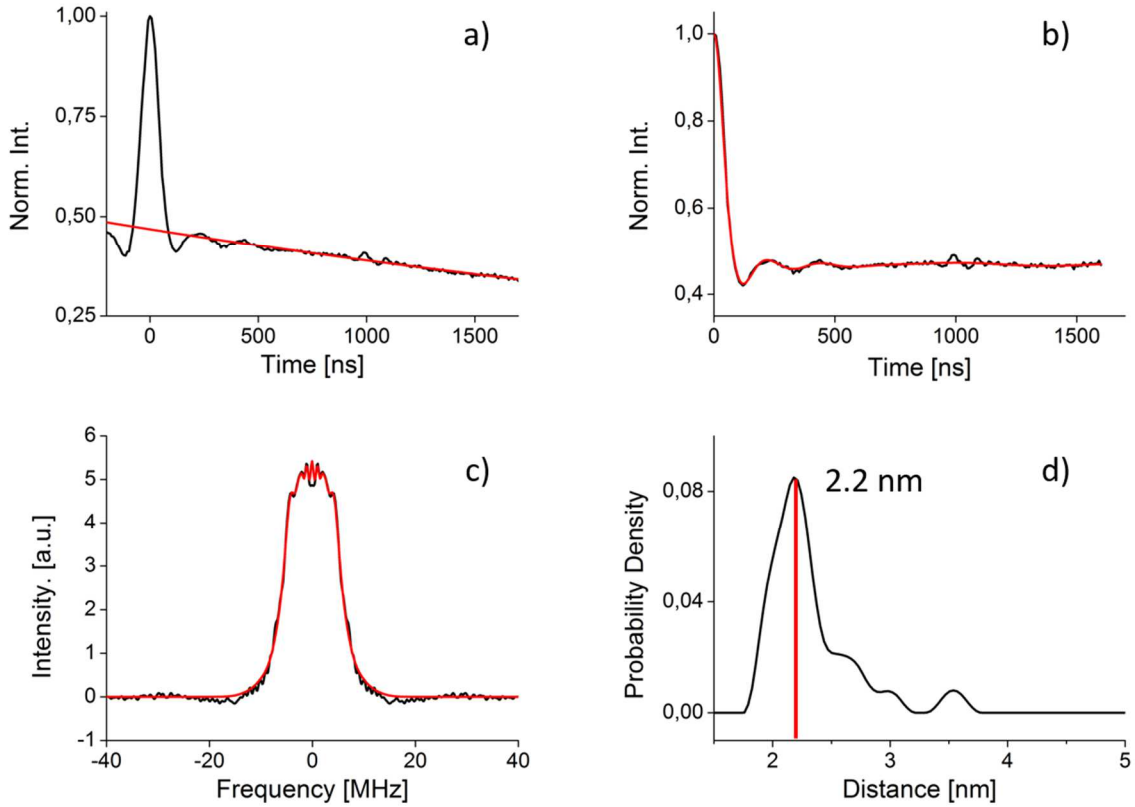

Figure 22: a) Original PELDOR time trace (black) and fitted exponential background (red) b) background corrected time trace (black) and DeerAnalysis2015 fit (red) c) Pake pattern (black) and its DeerAnalysis2015 fit d) distance distribution as determined via Tikhonov regularization (DeerAnalysis2015) of **4**

The results of the PELDOR measurement are shown in Figure 22. The modulation depth is 56 % with a SNR of 9.63 $min^{-1/2}$. For details how the SNR was calculated, see Appendix A.I. The timetrace shows strong dampening with only two clearly visible modulation periods. This goes against the previously made assertion that the molecule is very rigid. However, additional dampening may occur as a result of strong or intermediate coupling if the electron spins. Especially intermediate coupling, where the extend of the coupling is a complex determined by the relative orientations of the spin, can lead to a broad distribution of the dipolar interaction frequencies, which would explain the strong dampening of the timetrace. Looking at the frequency domain spectrum obtained in the experiment, it does not resemble the expected form of the Pake pattern, but shows a strong overrepresentation of frequency values close to zero. It also does not show two clear singularities, but the frequencies at the edge of the spectrum match expectations from DFT calculations of **4**. This distortion of of the Pake pattern may be due to the effects of the limited excitation bandwidth of the narrow pulses used here.[78] The distance distribution obtained via Tokhonov regularization shows a clear main distance peak at 2.1778 nm with a width a full width half-maximum (FWHM) of ~0.46 nm. The obtained distance is in good agreement with DFT predictions. The distance

distribution also shows smaller peaks at 2.6, 3.0 and 3.6 nm as well as hints ad a shoulder of the main peak at 2.0 nm. These peaks are most likely a result of the overrepresentation of low frequencies in the Pake pattern.

Proceeding on **5**, the experiment was repeated with the same parameters, with the exception that for a longer distance, a longer time trace is required.

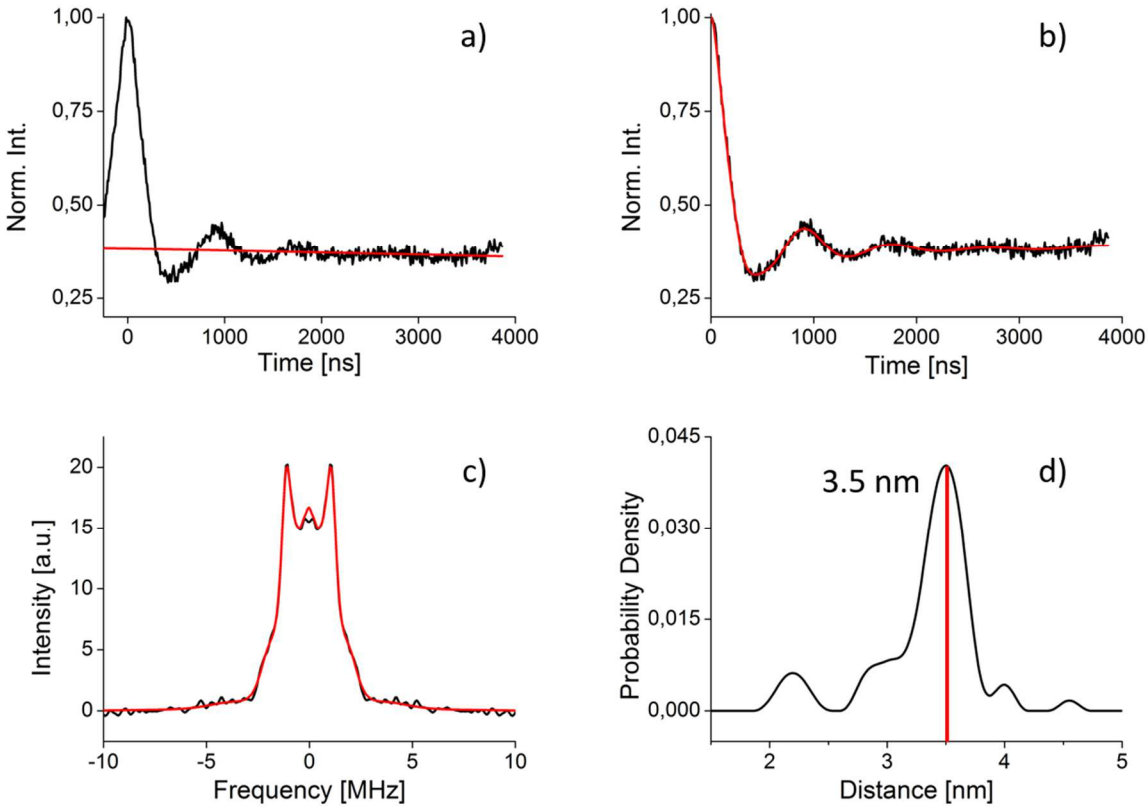

Figure 23: a) Original time trace (black) and its exponential background (red) b) background corrected time trace (black) and DeerAnalysis2015 fit (red) c) Pake pattern (black) and its DeerAnalysis2015 fit (red) d) distance distribution as determined via Tikhonov regularization (DeerAnalysis2015) of **5**

The results of the PELDOR measurements are shown in figure Figure 23. With the described approach, a modulation depth of 63 % and a SNR of 4.22 $min^{-1/2}$ was achieved. The SNR achieved is lower than what was achieved for **4** by a factor of 2.3. This is due to the longer timetrace that was recorded. For a longer timetrace to be recorded, a longer evolution periode of the spin system is required. For the period, the spin system will experience T_2 relaxation is which decreases the signal intensity, which will naturally reduce the SNR. The Pake pattern that was obtained shows no significant overrepresentation of any frequency region which allows for the conclusion that at the conditions of the experiment, no significant contributions of orientation selectivity exist. The data could be nicely simulated and Tikhonov regularization yielded a distance distribution with a main distance peak that shows a main

distance of 3.5051 nm and a FWHM of ~0.44 nm. The distance found deviates from the DFT prediction by roughly 1 Å, which is within the accuracy of DFT predictions for large molecules a good agreement.

2.2.3 RIDME of **4** and **5**

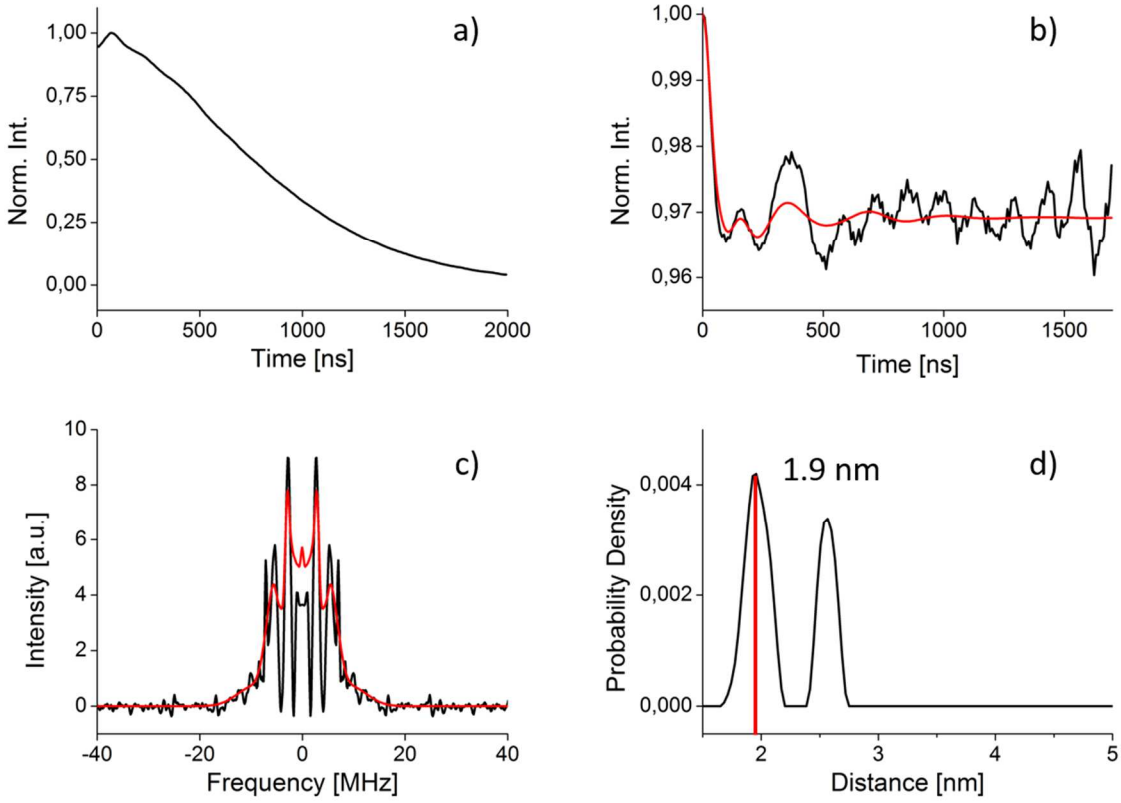

Figure 24: a) Original RIDME time trace (black) b) background corrected time trace and DeerAnalysis2015 fit (red) b) Pake pattern (black) and its DeerAnalysis2015 fit d) distance distribution as determined by Tikohonov regularization of **4**

For the RIDME measurements, two factors dominate the result of the experiment. The modulation depth is mostly determined by the length of the delay time T relative to the longitudinal relaxation time T_1. The longer the waiting periode T, the greater the modulation depth, up to the maximum when all spins that are not excited by the RIDME sequence relaxed exactly one time. After that, no further gain can be achieved through a longer waiting period, and negative effects such as spin diffusion will dominate. The longer the period T is the longer is the time in which relaxation effects can also dissipate the coherence and thereby the intensity of the echo. This means in effect that the longer the delay time T, the noisier is the acquired time trace. It was shown in a study by Yulikov et al. that for a RIDME experiment with two equal spins, the optimal compromise between these competing effect is reached when T equals T_1.[41] However, this result was obtained for gadolinium-gadolinium distance

measurements. Gadolinium (III) spins have relatively short T_1 and T_2 times[15, 79], while trityl radicals have very long T_1 times, but only moderate T_2 times.[77, 80] To determine the T_1 of **4** and **5**, inversion recovery experiments were performed. To determine the T_2 times of the compounds, 2-pulse-ESEEM experiments were performed.

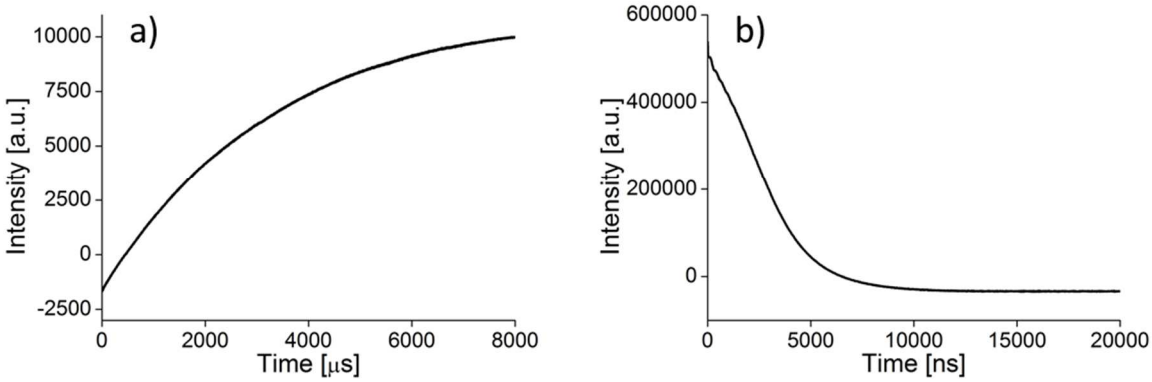

Figure 25: Inversion Recovery(a) and 2-Pulse-ESEEM of **4** in a 2:1 mixture of dichloromethane and methanol at 50 K

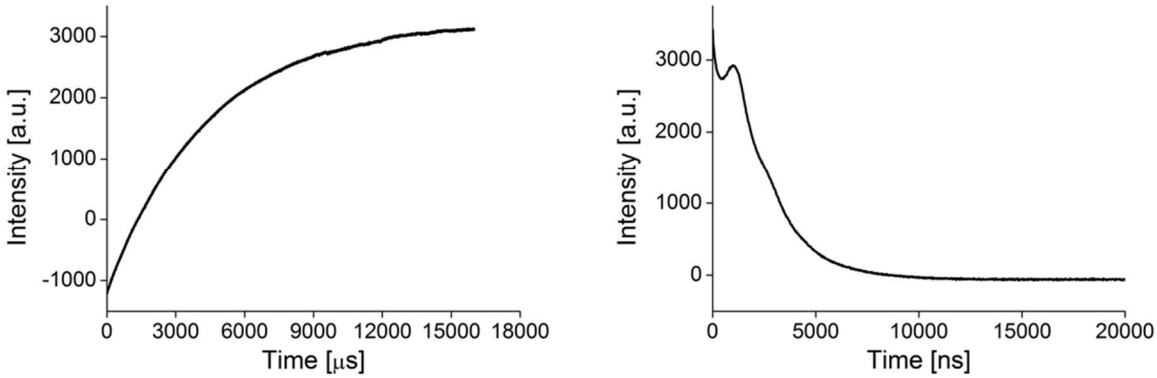

Figure 26: Inversion Recovery(a) and 2-Pulse-ESEEM of **5** in a 2:1 mixture of dichloromethane and methanol at 50 K

For **4**, a T_1 time of 3300 μs and T_2 times of about 2.8 μs were determined at 50 K. For **5**, a T_1 time of 4300 μs and T_2 times of about 2.7 μs were determined at 50 K. At so great disparities between the transversal and longitudinal relaxation times, it must be considered that while in the ideal case the spin ensemble only evolves under the influence of T_1, evolution periods in the ms regime allow for the occurrence of unlikely spontaneous events such as sin diffusion that will destroy the coherence in the x,y-plane. As a compromise, a time T of 100 μS was chosen. The results of the RIDME measurement of **4** is shown in Figure 24. For the bistrityl spin pair at the given condition, only a very small modulation depth of about 3 % was achieved. Further, the strong background of the RIDME experiment in conjunction with the low modulation depth causes artifacts in the time trace that are interpreted as an additional distance. The experiment therefore yields two distances, one at 1.9429 nm and one

at 2.5571 nm. The shorter distance is consistent with the distant that would be expected for a strongly coupled spin pair, the longer distance must be an artifact. Based on these results, it is fair to say that the experiment failed. In order to find a way to perform the experiment successfully, a change of the experiment conditions was needed. This can be approached from two different angles, either a change of the spectrometer settings, or a change to the spin system. A change of spectrometer settings allows for a wide variety of changes in terms of pulse lengths (shorter or longer), temperature, separation lengths of the various separations of the experiment, or microwave power. However, due to the many different options in absence of a clear hypothesis as to what caused the experiment to fail, it was decided that a moderate modification of the sample itself was a more promising approach. A modification of the chemical structure of **4** was however not considered, as any result obtained this way would be for a different molecule. This would have been not directly comparable to the other results presented here, and would defeat the purpose of this study. The least invasive change of the sample was a change of solvent. The previously presented measurement was performed in a frozen solution of two part dichloromethane and one part methanol. This mixture freezes as a glass, in which case no preferential relative orientations of the spins exist due to the unordered structure of the sample. In addition, frozen glasses can increase relaxation times, because relaxation mechanisms that rely on the transfer of energy to a surrounding lattice, e.g. via exciting lattice vibrations, are hindered.[77, 81] A sample of **4** was prepared in an identical fashion to the previously prepared sample, but instead of a mixture of methanol and dichloromethane, pure dichloromethane was used.

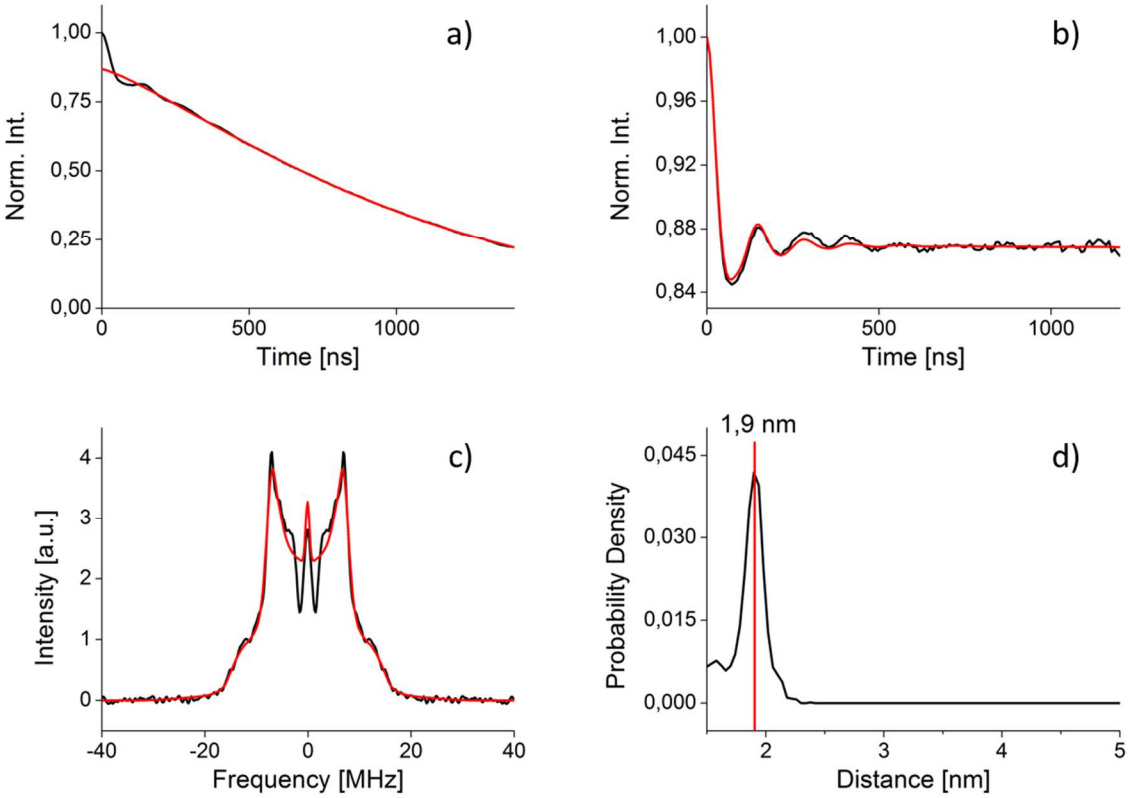

Figure 27: a) Original RIDME time trace (black) and its 3rd order polynomial background (red) b) background corrected time trace and DeerAnalysis2015 fit (red) b) Pake pattern (black) and its DeerAnalysis2015 fit d) distance distribution as determined by Tikohonov regularization of **4** at 50 K

The result of the measurement on this new sample is shown in Figure *27*. With the employed conditions, a modulation depth of 14 % along with a SNR of 3.98 $min^{-1/2}$ was achieved. The experiment delivered a single distance peak corresponding to a mean distance of 1.9386 nm and a width of 0.20 nm at FWHM. This is in good agreement with the expected distance under the assumption of dipolar coupling in the strong coupling regime. The width of the distribution is in accordance to the expected low flexibility of the compound. The timetrace is modulated for its entire length, although after three periods, the bad SNR starts to mask the modulation. This also supports that the molecule is very rigid. The modulation depth is still comparatively low, which can be understood because T was much smaller than T_1, and therefore only a relatively small fraction of spins invert during the experiment. Still, the result was considerably better than the originally obtained result shown in Figure *24*. To investigate the reason for the different results with the different solvent, the relaxation times of the sample in pure dichloromethane were determined via inversion recovery and 2-pulse-ESEEM

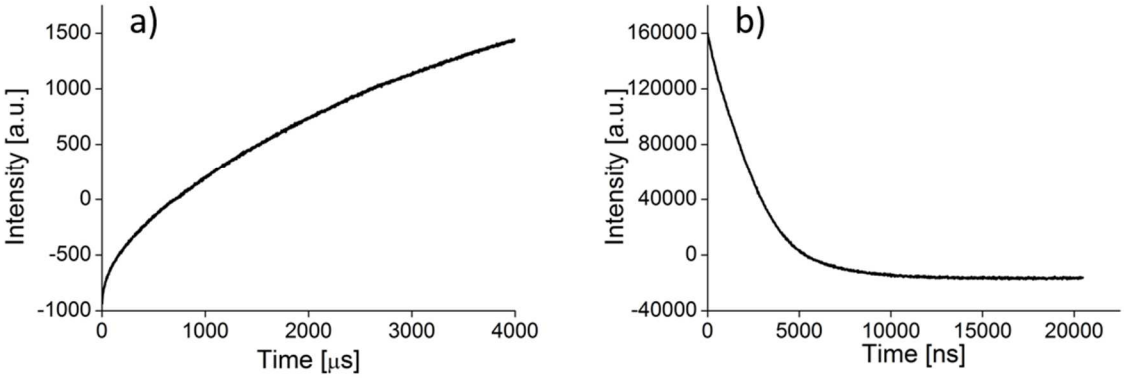

Figure 28: Inversion Recovery (a) and 2-Pulse-ESEEM (b) of **4** in dichloromethane at 50 K.

The T_1 time was determined to be 3300 μS with a T_2 time of 2.5 μS. From this, it is clear that the difference in performance is not due to a difference in the relaxation behavior. However, a distinct difference in the spectral width was observed.

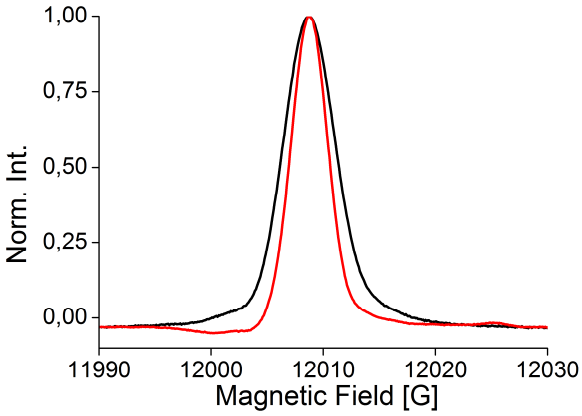

Figure 29: Echo-detected field sweep of **4** in dichloromethane (black) and 2:1 dichloromethane and methanol (red).

As is shown in Figure *29*, the sample of 4 in dichloromethane shows a spectral width at FWHM of ~5.2 G, while in a mixture of dichloromethane and methanol, a spectral width of ~3.7 G is observed. The spectral width in an EPR experiment on an ensemble of spins is usually dominated by the anisotropy of the g-value and by the hyperfine coupling tensor. Also, the lifetime of the spin states have an effect, since it determines the intrinsic linewidth of the spins. In a glass, all orientations are represented and experience a magnetic field in accordance to their relative orientation to the applied magnetic field. In a solution that did not freeze as a glass, the effect is the same as if water is frozen, where several domains exist where a crystalline structure exists, but not a unit cell which can represent the whole solid by means of translation. This also means that there are areas at the junctions between different crystallized domains. All this influences the local magnetic field that a spin experiences, and

leads to a broader distribution of resonance frequencies. This causes a larger spectral width.[23a] The most likely explanation why this increase in the line width improved the modulation depth and overall result of the experiment is that the RIDME experiment observes the effect of spontaneously occurring relaxation events on the part of the spin ensemble that is excited by the pulse sequence. According to Eq. 2.1, the used 24 ns pulses excite 41.6 MHz or 14.7 G, although this effect wears off towards outlying frequencies affected by the pulse as was discussed in section 2.2.1. This leaves very few spins outside the excited part of the spectrum that can affect the observed spins. With a broader spectrum, more spins remain unaffected by the microwave pulses, and can contribute to the dipolar modulation.

Based on this finding, it was concluded that the issue with the original attempt to measure a RIDME was that the pulses affected most spins, leaving only very few spins to flip to yield a dipolar modulation. Under this assumption, the obvious solution was to rerun the experiment on the original sample with narrower pulses. Based on Eq. 2.1, a π-pulse length of 80 ns with an excitation bandwidth of 12.5 MHz was estimated to yield a good compromise between modulation depth and SNR.

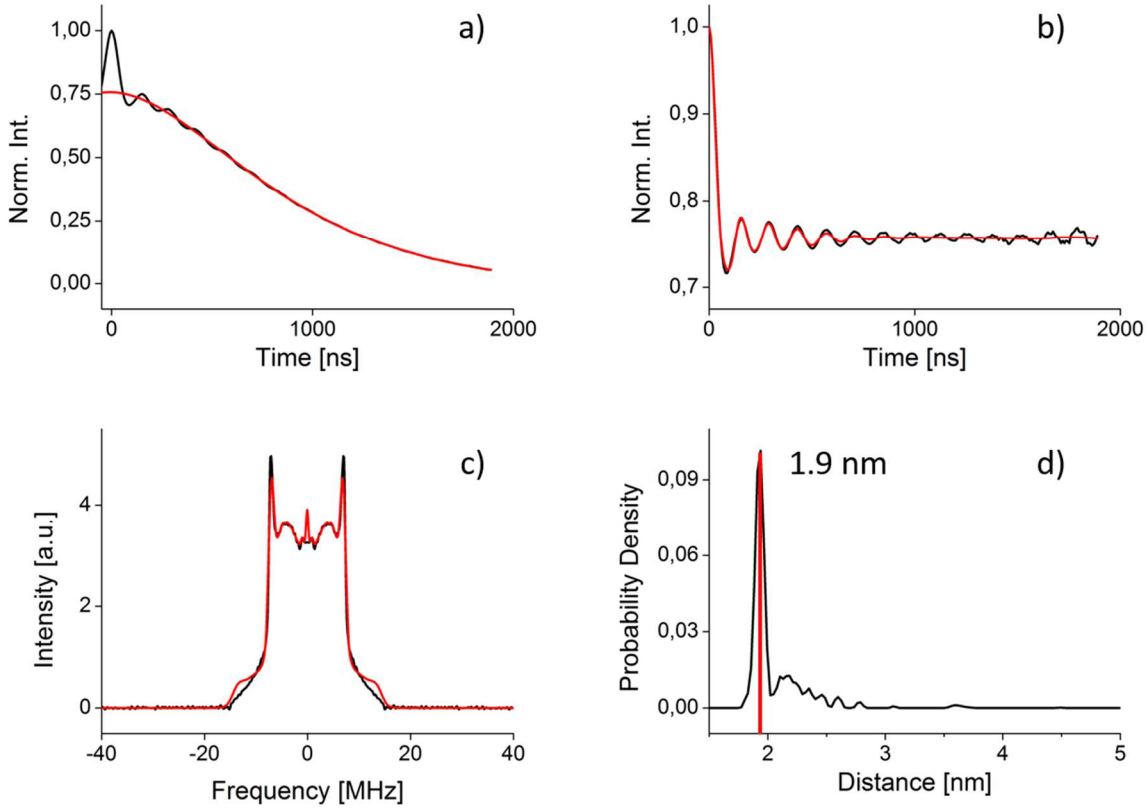

Figure 30: a) Original RIDME time trace (black) and its 3rd order polynomial background (red) b) background corrected time trace and DeerAnalysis2015 fit (red) b) Pake pattern (black) and its DeerAnalysis2015 fit d) distance distribution as determined by Tikohonov regularization of **4** at 50 K for 80 ns π-pulses.

With the changed measurement conditions RIDME was performed yielding a well-modulated time trace. A modulation depth of 25 % was achieved together with a SNR of 5.38 $min^{-1/2}$. The distance distribution shows a main distance peak at 1.9388 nm with a standard width of ~0.11 nm, as well as a smaller peak with a mean distance of 2.1582 nm and a width of ~0.27 nm. The relative intensities of the distance peaks indicate a relative occurrence of 78 % to 22 %. The main distance peak indicates that for the analysis of the timetrace, the pseudo-secular terms of the dipolar coupling must be considered. This is also supported by the Pake pattern, which shows a strong singularity at 7.1 MHz. The smaller peak corresponds to ~4.7 MHz, which is indicative of coupling outside the strong coupling regime. The exact value of the coupling constant depends on the relative orientation of the coupled spins, as was discussed in section 1.2.1. A likely explanation for the occurrence of the second distance peak is therefore that some spin pairs show a dipolar coupling in the intermediate coupling regime. The timetrace is well modulated with 13 well resolved modulation periods and a relatively good SNR for its entire length. These results show that a good way to measure RIDME on bistrityl model compounds with an inter spin distance of ~2 nm was successfully established on **4**. Since the RIDME experiment is highly dependent on the relaxation behavior of the involved spins, and the relaxation times strongly depend on the temperature, it was decided to repeat the experiment at 80 K. First, the relaxations times were determined as shown before via inversion recovery and 2-pulse-ESEEM. A T_2 time of 2.3 μs and a T_1 of 1130 μs were determined.

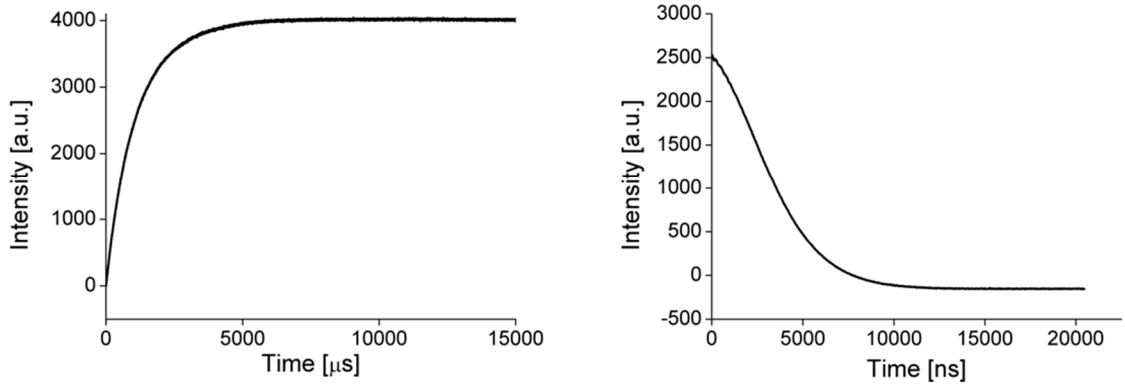

Figure 31: Inversion Recovery (a) and 2-Pulse-ESEEM (b) of 4 in a 2:1 mixture of dichloromethane and methanol at 80 K.

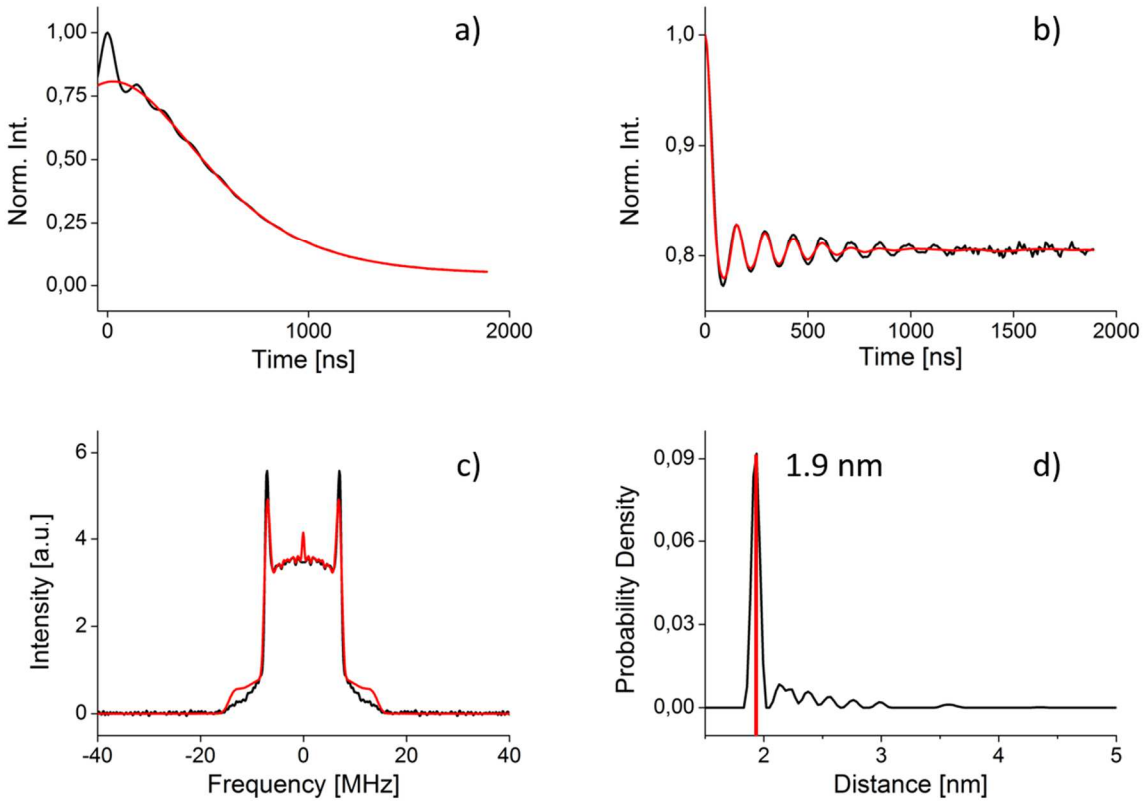

Figure 32: Original RIDME time trace (black) and its 3rd order polynomial background (red) b) background corrected time trace and DeerAnalysis2015 fit (red) b) Pake pattern (black) and its DeerAnalysis2015 fit d) distance distribution as determined by Tikhonov regularization of **4** at 80 K for 80 ns π-pulses.

The results of the measurement at 80 K are shown in Figure 32. In contrast to expectations, the modulation depth did not increase, but rather decreased slightly. The time trace shows a much stronger signal decay, which was to be expected for higher temperature. The results show that the stronger signal decay outweighs all possible gains from the shortened relaxation times and that the RIDME experiment for the bitrityl model compound performs better at 50 K.

Since the overall performance of the RIDME experiment was superior at 50 K, it was decided to attempt to measure RIDME on **5** at that temperature with a similar set of parameters to that which lead to a success for **4**. In deviation to the parameters for the RIDME on **4**, pulse separations were chosen to result in a significantly longer time trace as is required to record a longer distance.

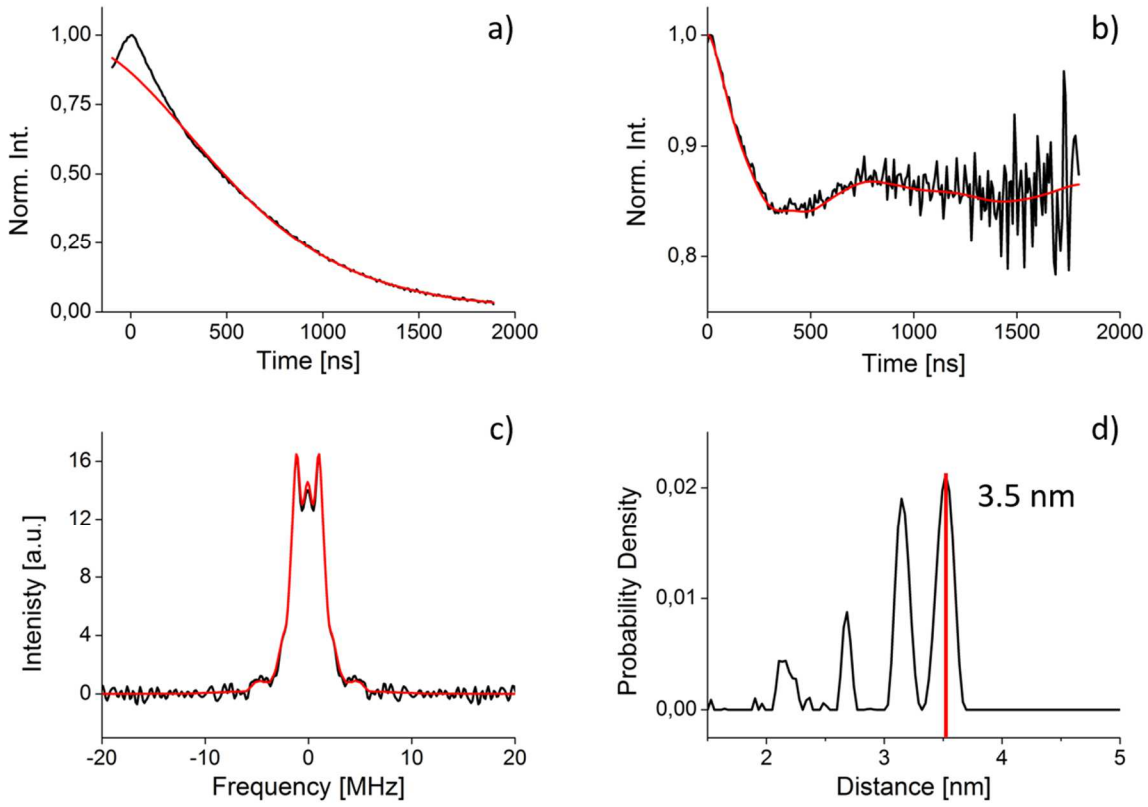

Figure 33: a) Original RIDME time trace (black) and its 3rd order polynomial background (red) b) background corrected time trace and DeerAnalysis2015 fit (red) b) Pake pattern (black) and its DeerAnalysis2015 fit d) distance distribution as determined by Tikhonov regularization of **5**

The results of the attempted RIDME on **5** are shown in Figure 33. A timetrace of dubious quality was obtained with a modulation depth of 15 % and an SNR of 1.65 $min^{-1/2}$. This is noticeably worse than the result on **4**, with a modulation depth of 10 % less and only about ¼ of the SNR. Tikhonov regularization reveals four distance peaks at mean distances of 3.5222 nm, 3.1466 nm, 2.6844 nm and 2.1355 nm. The peaks show a respective width of 0.17 nm, 0.14 nm, 0.12 nm and 0.17 nm. The ratio of the intensity of the peaks is 1 : 0.89 : 0.41 : 0.16 starting from the right in Figure *33*d. The longest obtained distance matches predictions from DFT calculations, but the other peaks must be artifacts of the measurement. A probable cause for this is the low SNR. Especially in the segment of 1000 ns to 2000 ns, the SNR is so low that it poses a significant difficulty for the analytical treatment of the data. For example at about 1300 ns, there is a rise of the mean signal intensity that was interpreted by the simulation software as a small modulation, but is more likely a noise artifact. In addition, it has been reported that both longitudinal relaxation and slow intramolecular motion can cause artifacts in a RIDME time trace.[39b, 39c] The longer molecule should be more prone especially to the latter, and this may have distorted the time trace, so that possibly the confluence of the mentioned effects may have caused the distance measurement to yield a wrong result where

the experiment yielded a correct result for **4**. A factor that may also have an effect is that only one and a half periodes of the modulation have been recorded. Attempts to measure a longer time trace were unsuccessful because the echo intensity relaxed to zero after 2 μs, and even at the current length, the noise reached unacceptable levels at the end of the timetrace.

2.2.4 SIFTER of **4** and **5**

In contrast to the PELDOR experiment, where a part of the spectrum is refocused and the effect of the inversion of another part of the spectrum is observed, and to the RIDME experiment, where a part of the spectrum is refocused and the effect of spontaneous effects on the rest is observed, the SIFTER experiment refocuses the entirety of the spectrum. The modulation depth of the experiment is therefore limited by the excitation with of the microwave pulses. In case of complete excitation, the limit for the modulation depth is 100 %, which is not possible with neither PELDOR nor RIDME. In practice, such high modulation depth can only be achieved on highly purified model compounds where all spins exist in pairs. When there are monoradicals present, their intensity is also refocused in the solid echo without contributing to the modulation. An additional issue is that incomplete excitation of the spectrum leads to artifact peaks, which is wrong distances that arise from unwanted coherence pathways.[32] Therefore, it is clear that for a good SIFTER, it is necessary to achieve as complete excitation of the spectrum as possible. This has been achieved for nitroxide radicals using arbitrary wave function generators (AWG)[45], but the narrow spectral width of the trityl spectrum allows sufficient excitation even without such a device, as was demonstrated by a previous study.[75]

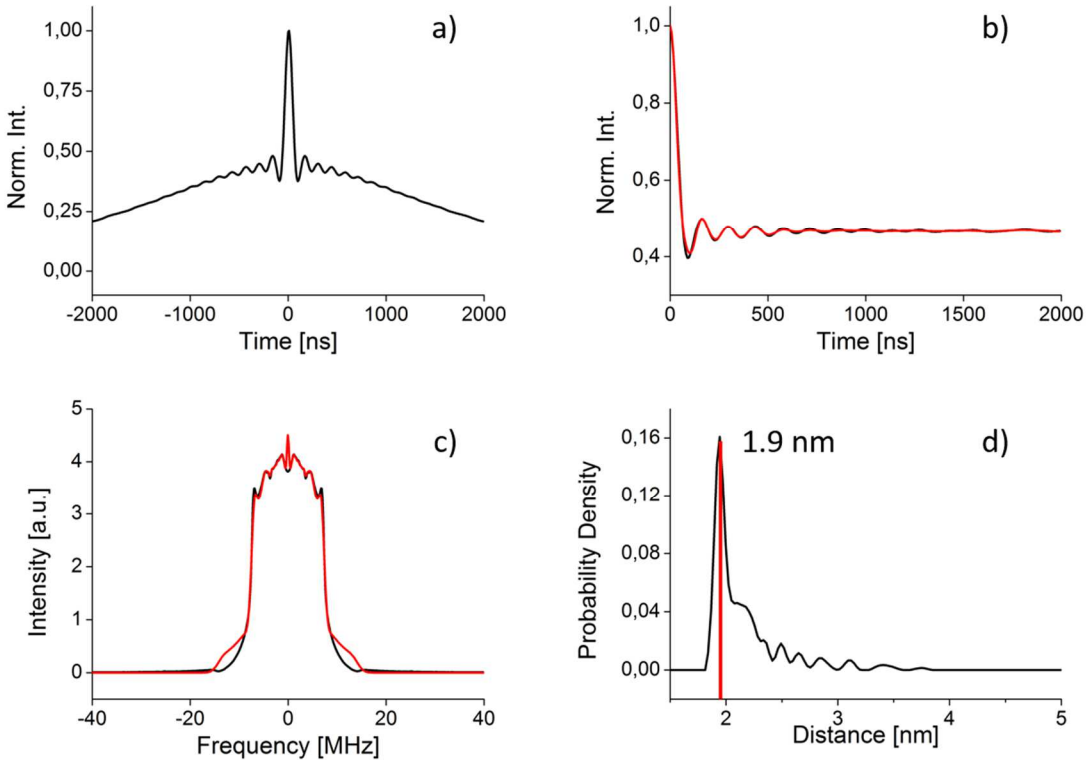

Figure 34: a) Original SIFTER time trace b) background corrected time trace (black) and DeerAnalysis2015 fit (red) b) Pake pattern (black) and its DeerAnalysis2015 fit (red) d) distance distribution as determined by Tikhonov regularization (DeerAnalysis20015) of **4**

The results of the SIFTER measurement are shown in Figure *34*. They show a modulation depth of 55 % along with a SNR of 22.05 $min^{-1/2}$. The modulation depth is lower than was expected, which indicates that the excitation of the spectrum was incomplete. Since a π-pulse of 24 ns was used, the excitation band width was calculated to be 50 MHz or about 17 G, which is well above the width of the trityl spectrum. As was discussed above, the excitation profile is such that the greater the frequency deviates from the mean excitation frequency, the lesser is the excitation gained from that pulse. As a result, the excitation of the trityl spectrum was most likely incomplete. This could be remedied by the introduction of shaped pulses with an AWG, as was successfully demonstrated by Schöps et al.[45], and more recently by Spindler et al.[82], where modulation depths of 95 % were achieved. Regardless, the SIFTER experiment gave an excellent result with a very good modulation depth and an excellent SNR. The edges of the Pake pattern show a frequency of 7.0 MHz, but also an overrepresentation of smaller frequencies. The distance distribution shows a main distance peak corresponding to a distance of 1.9437 nm with a width of ~0.12 nm (FWHM) as well as a strong shoulder at a distance of 2.1526 nm, which has a relative intensity to the main peak of 0.27. The distance distribution also shows a series of low intensity peaks towards larger distances. The main peak show a distance that is 87.1 % of the distance expected from DFT calculations, which

matches expectations for the dipolar coupling frequency under inclusion of the pseudo-secular terms perfectly. The shoulder corresponds to the result that is expected if the pseudo-secular terms are not considered. As was already discussed for the RIDME experiment, this is most likely due to spin pairs in that show dipolar coupling in the intermediate coupling regime. The small peaks may arise also from intermediate coupling, since intermediate coupling is difficult to predict and depends on the exact orientation of the spins to each other and the applied magnetic field, as was discussed previously. They may also arise due to the incomplete excitation of the spectrum.

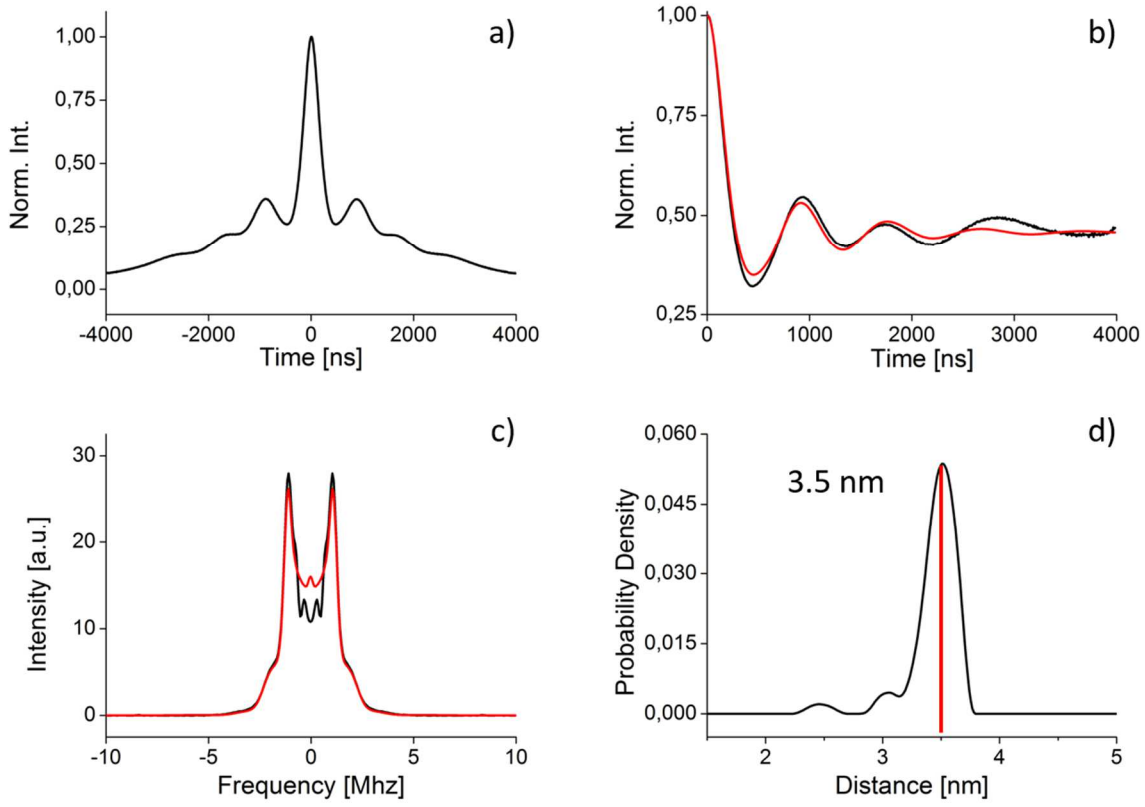

Figure 35: a) Original SIFTER time trace b) background corrected time trace (black) and DeerAnalysis2015 fit (red) b) Pake pattern (black) and its DeerAnalysis2015 fit (red) d) distance distribution as determined by Tikohonov regularization (DeerAnalysis20015) of **5**

The results of the SIFTER on **5** are shown in Figure 35. The experiment yields a well-modulated timetrace with a modulation depth of 63 % and a corresponding SNR of 23.04 $min^{-1/2}$. The Pake pattern is well-resolved and shows clear singularities at 1.1 MHz. The distance distribution shows a clear distance peak at 3.5060 nm with a width of ~0.31 nm. Two very small peaks at 3.0501 nm and 2.4639 nm with a relative intensity to the main peak of less than 10 % are also present. They may stem from incomplete excitation of the spectrum, but due to their low intensity, they are irrelevant to the analysis of this data. This result is

comparable to the result obtained on **4**, so it was demonstrated that SIFTER gives excellent results for bistrityl model compounds in the investigated distance range. However, the time trace rises after ca. 2500 ns again, which is due to the SIFTER background. Unfortunately, no exact mathematical description of the background exists today, which makes the analytical treatment of the data difficult. To solve this issue, two approaches were tried. First, the time trace was cut at 2300 ns, so the data before the background artefact was analyzed.

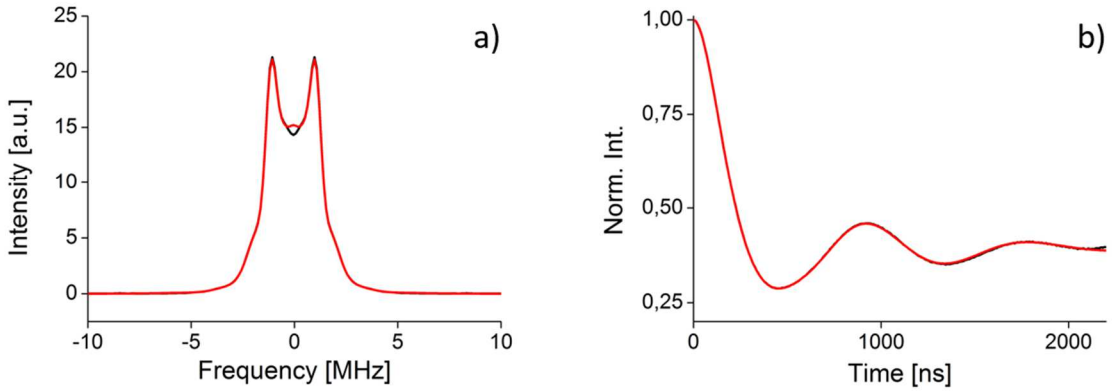

Figure 36: Pake pattern (a) and background corrected time trace (black) and DeerAnalysis2015 fit (red) (b) of the cut SIFTER time trace of **5**

The second approach was to manually fit two different 3rd order polynomials to the time trace to model the background.

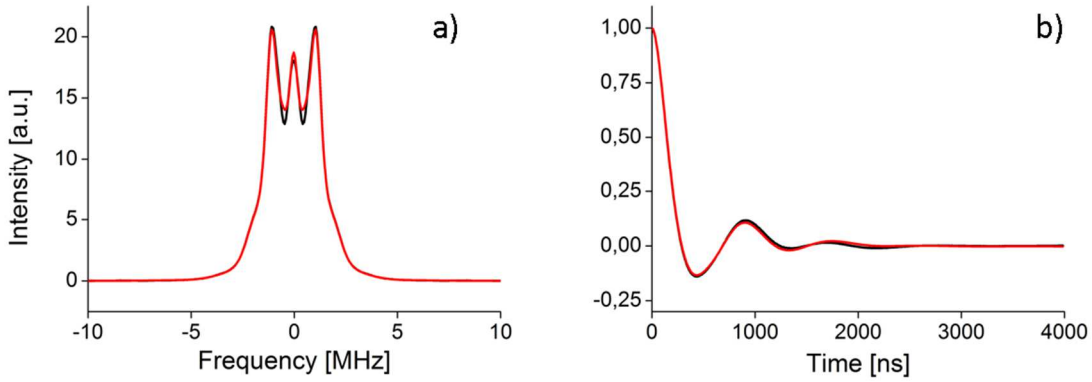

Figure 37: Pake pattern (a) and background corrected time trace (black) and DeerAnalysis2015 fit (red) (b) of the manually background corrected SIFTER time trace of **5**

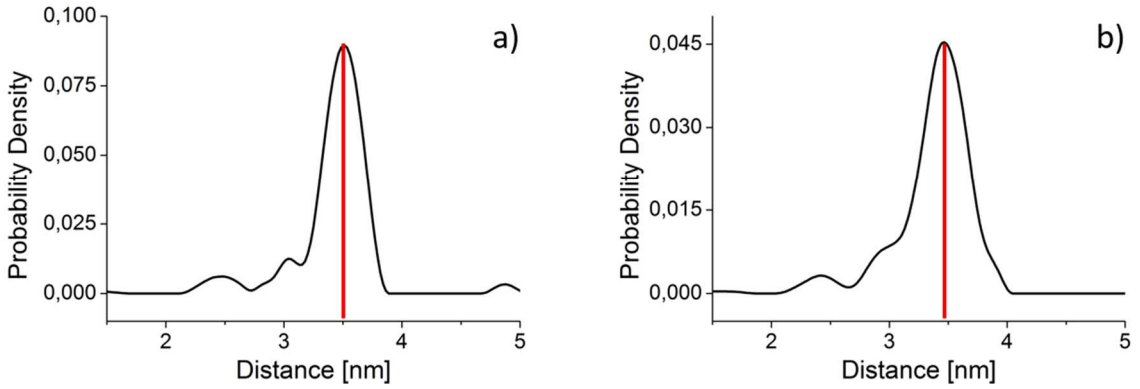

Figure 38: Distance distributions of the SIFTER experiment on **5** employing a) a cut time trace b) a manually background corrected time trace.

To assess the improvement of the DeerAnalysis2015 fit as a result of this data treatment, the root mean square error of the fit (RMSE) of all three fits are compared. The initially shown fit of the background corrected data in Figure *35*b shows a RMSE of 0.01643. The fit of the cut timetrace shown in Figure *36*b exhibits a RMSE of 0.00163, and the fit of the manually corrected timetrace shown in Figure *37*b has a RMSE of 0.00671. This shows that both alternative methods of data treatment improve the quality of the fit by a factor of ~10 and ~2.4, respectively. However, the effects on the obtained distance distributions must also be considered. For the cut timetrace, a main distance peak with a main distance of 3.5091 nm width a width of 0.38 nm was obtained, while for the manually corrected timetrace, a mean distance peak at 3.4669 nm with a width of 0.43 nm was obtained. Comparing this to the treatment of the original data, this is a deviation of 0.0031 nm from the mean distance and an increase of the width of the distribution by ~0.07 nm for the former, and a deviation of 0.0391 nm and an increase of the width of distribution by ~0.12 nm for the latter. From this, it can be concluded that cutting the timetrace after two modulation periods has only negligible effects on the obtained mean distance, but leads to a sizeable increase in the width of the distribution. One would expect this effect as the mathematical result of Fourier transformation upon cutting the data in the time domain. Keeping in mind that EPR distance measurements are ultimately used to gain structural information on biological macromolecules and statements about the flexibility of an investigated domain are made on the grounds of the width of the distribution, this poses no small problem for biological applications of this method. Also, the applied data treatment limits the interpretation of the timetrace to a length of 2.3 μs, which reduces the access to longer distances. The removal of the background via two manually fitted 3rd order polynomials appears to cause more significant changes. The change of the mean distance by almost 0.4 Å can, depending of the application, be not negligible. The increase in

the width of the distribution by close to 40 % is significant and brings with it all the issues mentioned above for the cut timetrace, only more so. From this analysis it is clear that both methods of data treatment are problematic, and future use of the SIFTER experiment will require the development of a mathematical description of the background function. Based on the data presented here, it is unclear what causes the background to rise again, and if this issue is specific to trityls or also occurs in different spin systems. No mention of such issues was made in previous publications on SIFTER on bisnitroxide and bistrityl conpounds, although it was suggested to remove the background by measuring a SIFTER on a monoradical compound of the same type (here: a single trityl) and dividing the data by this timetrace.[45, 75]

2.2.5 DQC of **4** and **5**

The DQC experiment is in many regards very similar to the SIFTER experiment. It also depends on the excitement of as large a part of the spectrum as possible. In contrast to the SIFTER experiment, where a solid echo is created and modulation is induced by a pulse along the y-axis, DQC relies on inducing coherence on a forbidden double quantum transition which evolves with the offset frequency of the two coupling spins. If this coherence is transformed into an echo, its amplitude is modulated with the sinus of the combined dipolar and scalar coupling at the function of the evolution time. However, as a forbidden transitions is much less likely to occur than any given allowed coherence pathway, the experiment requires a double quantum filter to eliminate all other contributions.[31] For a more detailed discussion of the involved physics and math, see the introductory section. The relevant information for this section is that the experiment is supposed to give a very high modulation depth, but requires a number of conditions to be met to produce a result. The most important condition for the experiment is that the phase coherence between the pulses must be maintained at all times.[31] In most pulse sequences, this is optimized by maximizing the amplitude of a transient echo arising from the applied pulses. Such an optimization is fairly complicated to do on the DQC sequence, as the desired double quantum echo only emerges after the phase cycle and can therefore not be observed in a transient. Since the DQC sequence is rather similar to the SIFTER sequence, it can be interpreted as the same detection sequence with a so-called DQ coherence sandwich instead of a pulse along the y-axis to induce dipolar modulation. DQC has the same phase as the SIFTER experiment, so that pulses and phases can be optimized on the SIFTER sequence and the results then transferred to the DQC experiment.

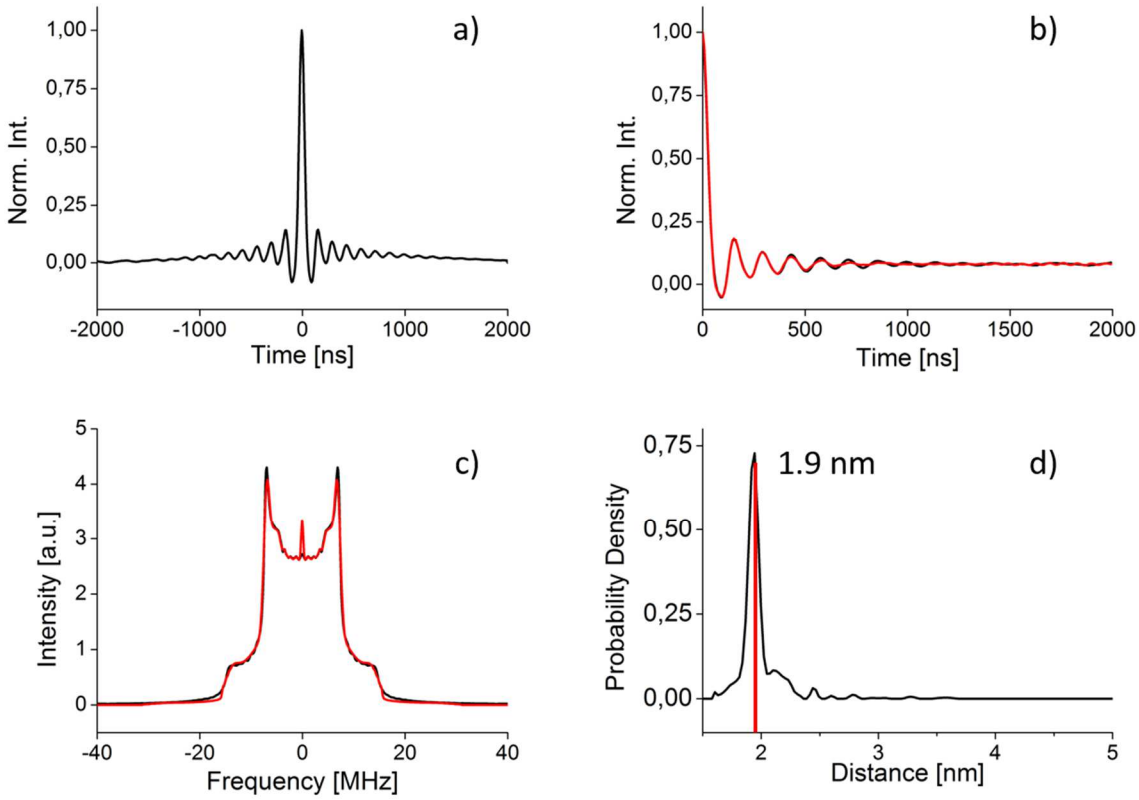

Figure 39: a) original DQC time trace b) background corrected time trace (black) and DeerAnalysis2015 fit (red) b) Pake pattern (black) and its DeerAnalysis2015 fit (red) d) distance distribution as determined by Tikhonov regularization (DeerAnalysis20015) of **4**

The result of the DQC on **4** are shown in Figure 39. A modulation depth of 99 % and a SNR of 26.83 $min^{-1/2}$ was achieved. The very high modulation depth is due to the 64-step double quantum filter, which eliminates all signal contributions that do not show dipolar coupling. It should be noted that in order to analyze the data with DeerAnalysis, a constant offset of 0.04 was added, and therefore the background corrected time trace shows an apparent modulation depth of 95 %. . The Pake pattern is clearly resolved, and shows a clear singularity at 7.1 MHz. The distance distribution shows a main distance peak at 1.9437 nm with a width of ~0.11 nm as well as a shoulder at 2.1004 nm with a relative intensity to the main peak of 11.5 %. It also shows a number of peak of negligible intensity corresponding to longer distances. The result in terms of the distance distribution is very similar to the results obtained via SIFTER and RIDME. It stands to reason to explain the result of the experiment in the same fashion, namely that the main peak corresponds to the distance that one would expect from DFT calculations if the pseudo-secular parts of the dipolar coupling are considered. The most likely explanation for the shoulder and the minor peaks is intermediately coupled spins.

Following the same procedure, the DQC of **5** was measured.

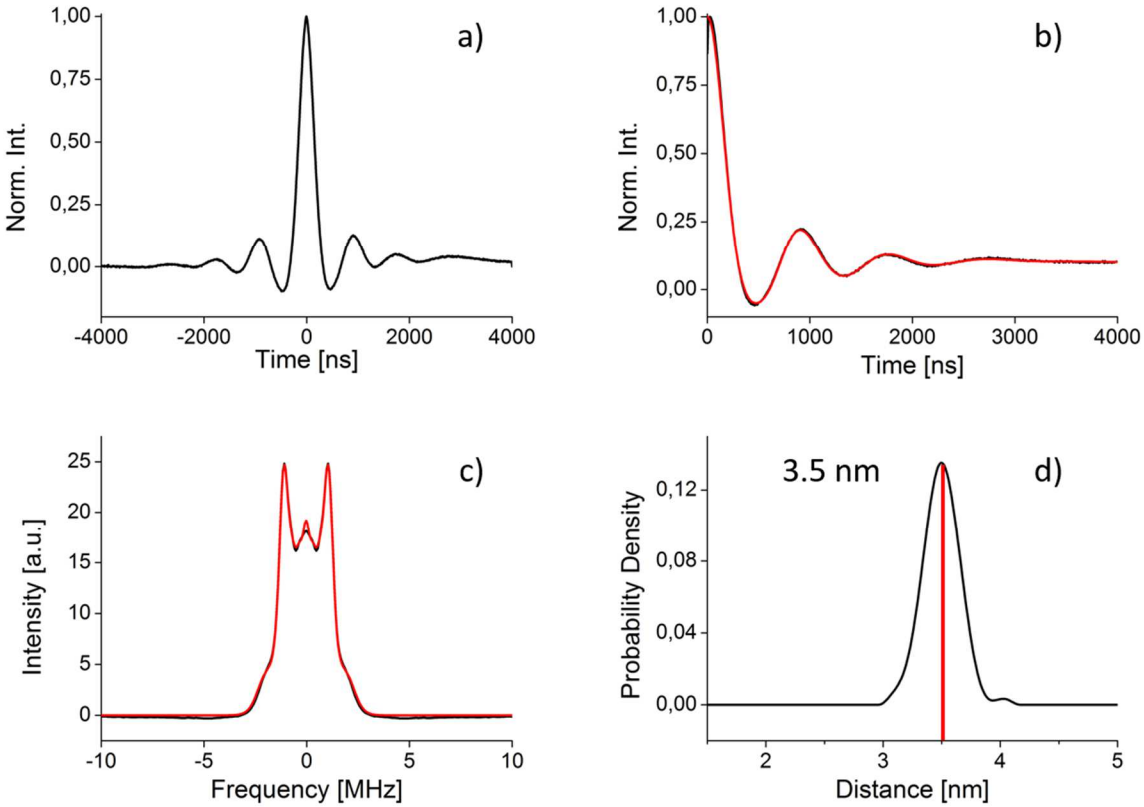

Figure 40: a) original DQC time trace b) background corrected time trace (black) and DeerAnalysis2015 fit (red) b) Pake pattern (black) and its DeerAnalysis2015 fit (red) d) distance distribution as determined by Tikohonov regularization (DeerAnalysis2015) of **5**

The results of the DQC for **5** are shown in Figure 40. The modulation depth is 99 % with a corresponding SNR of 20.93 $min^{-1/2}$. Again, a constant offset of 0.04 was added for the analysis of the data with DeerAnalysis. The Pake pattern is well resolved and shows a clear singularity at 1.1 MHz, although the parallel component of the Pake pattern is less pronounced. Similar deformations of the Pake pattern have been explained as due to uncertainties of the background function in the literature.[75] The distance distribution shows one peak with a mean distance of 3.5060 nm and a width of 0.35 nm. This is a good match with the predictions derived by DFT calculations.

Table 4: Overview of the results of the pulsed EPR distance measurements on **4** and **5**

Compound	Method	Δ [%]	SNR [$min^{-1/2}$]	<r> [nm]
SSMDV1	PELDOR	56	9.63	2.2
	RIDME	25	5.38	1.9
	SIFTER	55	22.05	1.9
	DQC	99	26.5	1.9
SSMDV2	PELDOR	63	4.22	3.5
	RIDME	10	1.65	3.5; 3.15
	SIFTER	63	23.04	3.5
	DQC	99	20.93	3.5

In the previous parts of this section, the individual performances of the various possible methods for EPR distance measurements were presented and discussed. In the following, the relative performance of the demonstrated measurement techniques will be discussed.

In section 2.2.1., *cw*-EPR was performed to determine the inter spin distance of **4** and **5**. While this was done successfully for **4**, the achieved result required a large part of additional knowledge that was gained from DFT calculations and other *cw*-EPR experiments that hinted at coupling in the strong coupling regime. While *cw* distance measurements are known from literature, and have been successfully performed on bistrityl compounds[76], it was shown to give ambiguous results under the applied conditions and for the used model compound. Although the inter spin distance determined in the end was a good match to DFT calculations, the experiment as demonstrated here would not be able to stand without the supporting experiments that were performed. For **5**, it was not possible to determine a dipolar coupling constant.

Looking at the pulsed EPR experiments, they can be easily devided into two pairs. The first pair, comprised of PELDOR and RIDME, did perform significantly worse than the other pair, SIFTER and DQC. PELDOR gave for both **4** and **5** the correct mean distance, but suffered from bad SNR in both cases, which was worse than SIFTER and DQC by at least a factor of 2, and significantly more so for the longer distance. RIDME, on the other hand, produced relatively low modulation depths, which is of course to be expected for spins with so long T_1 relaxation times as the trityl radical. In terms of the SNR ratio, it performed worse than the PELDOR experiment for **4** and **5**. The RIDME experiment also failed to deliver an unambiguous distance distribution for **5**, showing two different distance peaks of near identical intensity. This makes it the worst of the tested experiments for the determination of

trityl-trityl distances. For the distances tested here, the SIFTER and the DQC experiment perform almost equally well in terms of SNR, although DQC shows a higher modulation depths. It should be noted though that the similar performance in terms of SNR is only so because the DQC has a much larger modulation depth. The noise level is actually lower for the SIFTER time trace, so if modulation depth were disregarded, the SNR of the SIFTER time trace would actually be better. This is in accordance with a study by Schöps et al.[75], that found that if broadband excitation is used and near 100 % modulation depth is achieved for SIFTER, a higher SNR than for DQC is achieved. The findings to the relative performance of PELDOR to DQC is also consistent with previous studies by Reginsson et al.[13b, 76] The SIFTER, DQC and RIDME experiments on **4** showed main distance peaks with a mean distance of ~1.94nm, which is ~87 % of the distance expected from DFT calculations. As was discussed with the individual experiments, this stems from dipolar coupling in the strong coupling regime. Interestingly, PELDOR showed a main distance of ~2.17 nm, which is much closer to the distance expected from DFT calculations, which is ~2.23 nm. The single frequency experiments excite a large part of the spectrum, and the obtained distance distribution indicate that most spins show coupling in the strong coupling regime. PELDOR excites only a fraction of the spectrum, and in this case, this fraction corresponds to spins that predominantly show coupling in the intermediate coupling regime. This conclusion is also supported by the unusual strong dampening found for the PELDOR timetrace. It needs to be stressed that this connection between PELDOR and the intermediate coupling regime is purely coincidental. It is also coincidental that the dipolar coupling frequencies that were obtain correspond to distances closer to the DFT predictions. The results do not infer an intrinsic advantage of PELDOR. The particular benefit of the results presented here is that while other studies have applied various techniques to a variety of model compounds, no other study exists today that has used all four major pulsed distance measurement techniques, much less on the same sample. Given that today only a scarce hand full of papers exist that deal with the use of trityl radicals in EPR distance measurements[13b, 17, 72, 75-76, 83], this study is a significant step towards the understanding of the scope and limitations of the various distant measurement techniques with regards to trityl-trityl distance measurements.

2.2.5 Summary

cw-EPR was used for the determination of the inter spin distance of two bistrityl model compounds. It was found that if additional information from other experiments is used, it can be successfully employed to determine the inter spin distance of a model compound of with a inter spin distance of ~2.2 nm, but not for a model compound with an inter spin distance of ~ 3.5 nm. Four different pulsed techniques for the measurement of an inter spin distance were tested on the same model compounds. Of the pulsed techniques, SIFTER and DQC performed significantly better than PELDOR and RIDME. Under the given conditions and for the given samples, DQC performs comparably to SIFTER, although the absolute noise levels of the recorded time traces indicate that for cases where complete excitation of the spectrum can be achieved, e.g. with adiabatic pulses and an AWG, SIFTER may perform better. All these findings are consistent with previous studies known from literature. [13b, 75-76]

2.3 Characterization of new trityl spin labels and their application in in vitro and in-cell EPR distance measurements

The contents of this section have also been published in J.-J. Jassoy[+], A. Berndhäuser[+], F. Duthie, S. P. Kühn, G. Hagelueken, O. Schiemann[*], *Angew. Chem. Int. Ed.* **2017**, 56, 177-181.

Structure determination of biomacromolecules is an important task for the investigation of many biological functions, such as apoptosis [84] or the opening and closing of ion channels in cell membranes [85] and many others. A method that has emerged as a useful tool in this endeavor is EPR. The details of this method and the need for site specific spin labeling was discussed in the introduction, where trityl were presented as a new class of spin labels. The use of tritys in EPR distance measurements has seen tremendous advances especially in the last five to ten years.[13b, 17, 72, 75-76, 83] Nonetheless, the labeling of biomolecules with tritys today is still very limited, and the available options suffer from drawbacks such as low labeling efficiencies [53] or they label only the terminal positions of an oligonucleotide. [13a]

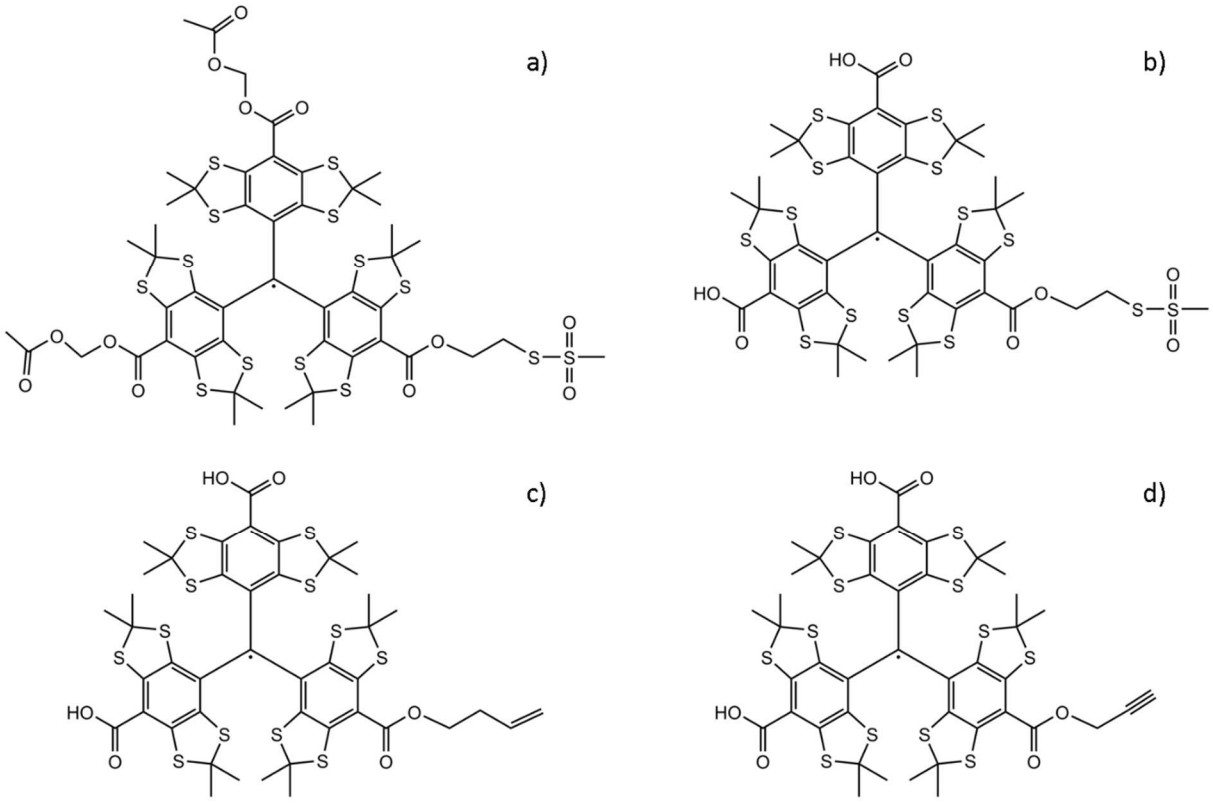

Figure 41: Trityl spin labels for the labeling of proteins and oligonucleotides **6** (a), **7** (b), **8** (c) and **9** (d)

To expand the range of available trityl spin labels and to overcome the limitations mentioned above, four different trityl spin labels (see Figure 41) were synthesized by Dipl. Chem. Jean-

Jacques Jassoy. In this chapter, the characterization of these spin labels by EPR spectroscopy and their labeling efficiencies in modified standard labeling procedures is shown. The labeling conditions will be included for the sake of clarity (see appendix C), but are the work of B. Sc. Fraser Duthie. The performance of **7** and **8** in *in vitro* Fe(III)-trityl RIDME on *pseudomonas putida* CYP101 is shown and compared to the performance of the commercially available MTSSL nitroxide spin label (**1**, see Figure *7*). The performance of the trityl spin labels is compared to other available trityl labels based on previously published results and *in silico* predictions. Then, the first in-cell measurement between a spin label and a native metal cofactor is shown using **8** and *pseudomonas putida* CYP101, which is at the same time the first *in cell* measurement using trityl spin label, and the first *in cell* RIDME.

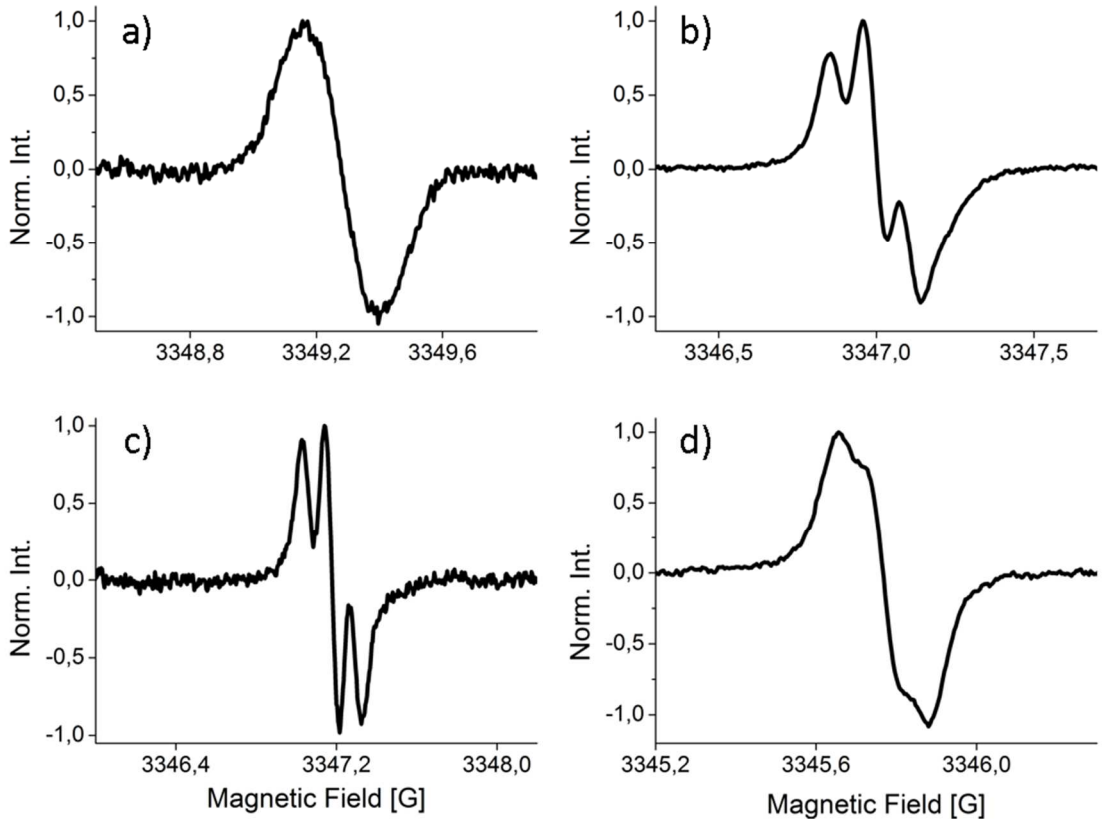

Figure 42: X-band cw-EPR spectra of degassed samples of a) **6** b) **7** c) **8** and d) **9** in methanol at room temperature

The X-band *cw*-EPR spectra of the spin labels TSL1-4 are presented in Figure 42. In contrast to what is usually found in the literature, the samples were thoroughly degassed to avoid contributions to the linewidth from oxygen. Under the applied conditions, the hyperfine coupling constants to the acid protons can be at least partially resolved, as can be seen in Figure 42 b-d. From the obtained spectra, the spectroscopic characteristics of the labels were determined via simulations using the program Easyspin.[86] Since in the frozen state several

characteristics such as the hyperfine tensor differ, e.g. because anisotropic parts are not averaged out in the frozen state, spectra were also recorded at cryogenic temperatures.

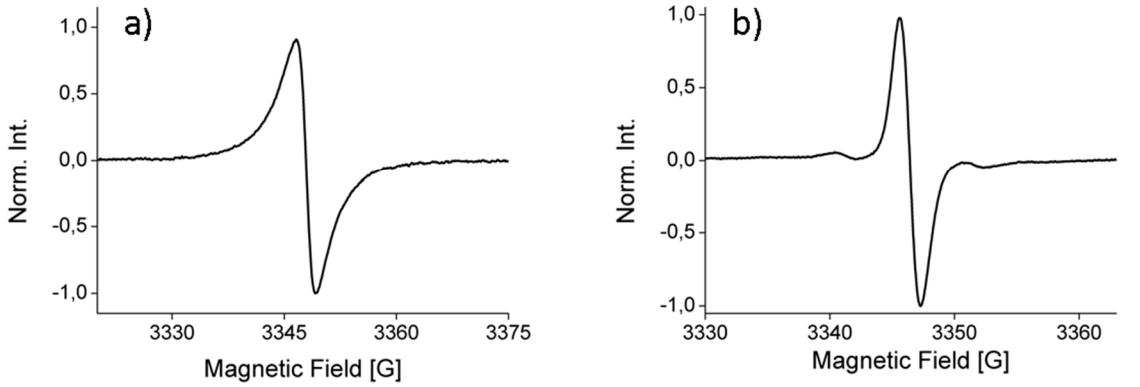

Figure 43: X-band cw-EPR spectra of **6** (a) and **7** (b) in methanol at 80 K

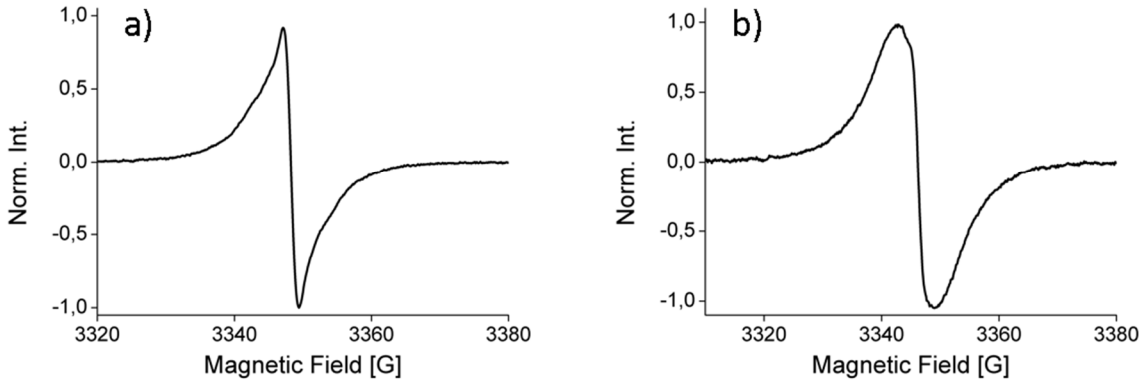

Figure 44: X-band cw-EPR spectra of **8** (a) and **9** (b) in methanol at 80 K

Table 5: Spectroscopic parameters of **6-9** at room temperature as determined by Easyspin

Compound	**g-value**	**Line width [G]**	**HFC (^{13}C) [MHz]**	**HFC (^{1}H) [MHz]**
6	2.0026	0.23 0	26.9	-
7	2.0027	0.09	26.9	0.3
8	2.0027	0.09	26.9	0.3
9	2.0028	0.09	26.9	0.2

Table 6: Spectroscopic parameters of **6-9** at 80 K as determined by Easyspin

Compound	**g-value**	**Line width [G]**	**HFC (^{13}C) [MHz]**	**HFC (^{1}H) [MHz]**
6	2.0027	4	[26.9; 50]	-
7	2.0027	3.3	[26.9; 50]	-[a]
8	2.0028	3.2	[26.9; 50]	-[a]
9	2.0028	3	[26.9; 50]	-[a]

a = cannot be resolved

The spectroscopic characteristics of **6-9** can be seen in Table 5 and Table 6. Having determined the g-value, line width and the resolved hyperfine coupling constants of the labels, their stability under the conditions of the labeling process had to be measured. To that end, samples were prepared in DMSO at ambient oxygen, dry degassed DMSO, degassed TRIS buffer, and TRIS buffer at ambient oxygen. Due to its low solubility in water, **6** was only tested in DMSO. The stability of the spin labels under the respective conditions was than monitored as the integrated intensity of the EPR signal of the trityl label against time.

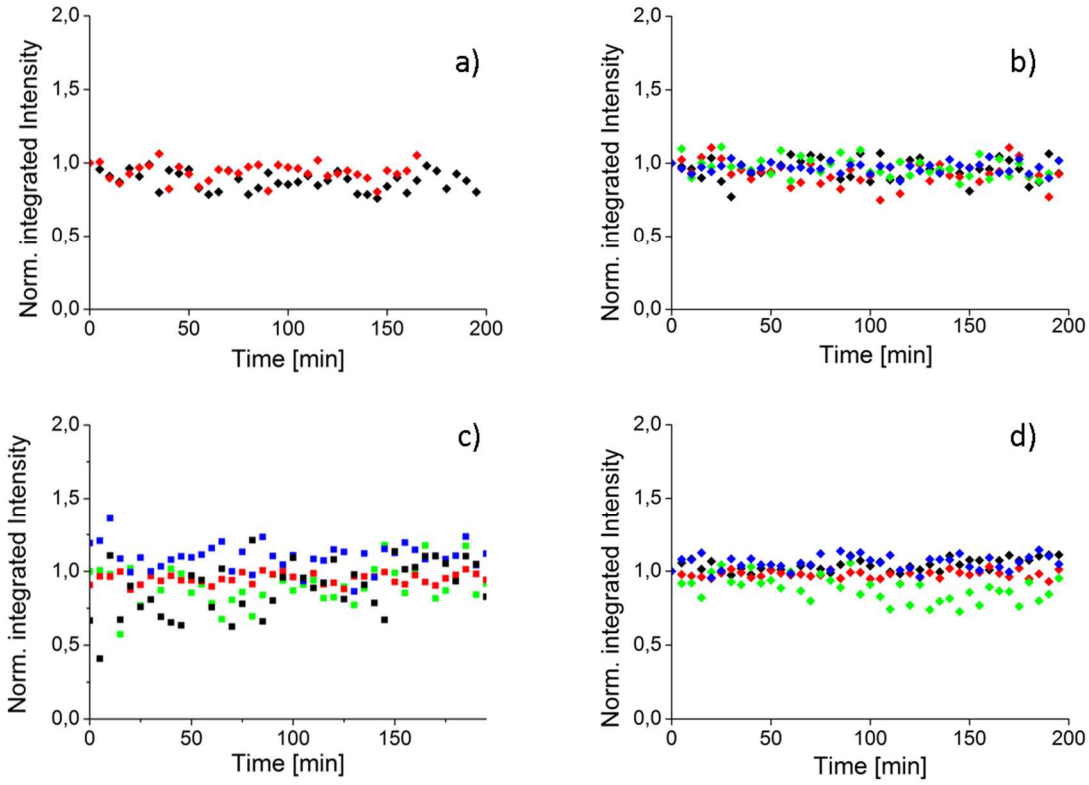

Figure 45: Stability of **6** (a), **7** (b), **8** (c) and **9** (d) in DMSO (red), degassed DMSO (black), TRIS buffer (blue) and degassed TRIS buffer (green)

Figure 45 shows the results of the stability time series. The signal intensity was monitored for 3 h for each case. Under the tested conditions, no signal decay could be detected for any of the spin labels, therefore it is concluded that **6-9** are stable in the given media within a time frame relevant to the labeling procedures.

Having established that the labels will survive the labeling conditions, a suitable labeling position on the protein of choice, *pseudomonas aeruginosa* cytochrome CYP101, needed to be determined. From a previous study, it was known that C58 was a good labeling position for labeling with **1**.[87] The chemical structure of the trityl itself is a lot bulkier than that of **1**, but it also should be considered the linker that builds that binds to the protein is longer than for **1**.

This makes it difficult to transfer information of the accessibility of a labeling site for **1** to a trityl label. Therefore the accessibility of the C58 residue for trityl spin label had to be independently determined. To that end, two sets of samples of cytochrome CYP101 labeled at the C58 residue with **7** (CYP101 C58T$_1$) were prepared. Both samples were prepared to have a protein concentration of 50 μM. One of these sets was treated with urea prior to the labeling procedure, the other was not changed in any way. The urea causes the protein to uncoil, so that virtually all steric inhibition for the labeling is eliminated. For the actual labeling procedures, see appendix D. For the two sets of samples, *cw*-EPR spectra were recorded at X-band and the double integrated signal intensity was determined. To account for statistical errors, the experiment was repeated ten times for both sets of samples.

Table 7: Double integrated intesity of CYP101 C58T1 samples at a protein concentration of 50 µM with and without treatment with urea prior to labeling. The error is given as the standard error of the mean.

Sample Nr.	**Double Integral (urea)**	**Double Integral (no urea)**
1	$4.4 \cdot 10^{-3}$	$6.9 \cdot 10^{-3}$
2	$5.1 \cdot 10^{-3}$	$6.8 \cdot 10^{-3}$
3	$7.1 \cdot 10^{-3}$	$7.0 \cdot 10^{-3}$
4	$7.0 \cdot 10^{-3}$	$7.2 \cdot 10^{-3}$
5	$5.1 \cdot 10^{-3}$	$6.3 \cdot 10^{-3}$
6	$7.2 \cdot 10^{-3}$	$7.2 \cdot 10^{-3}$
7	$5.5 \cdot 10^{-3}$	$7.2 \cdot 10^{-3}$
8	$7.1 \cdot 10^{-3}$	$6.8 \cdot 10^{-3}$
9	$7.2 \cdot 10^{-3}$	$6.6 \cdot 10^{-3}$
10	$6.9 \cdot 10^{-3}$	$7.4 \cdot 10^{-3}$
	$\emptyset = (6.3 \pm 0.35) \cdot 10^{-3}$	$\emptyset = (6.9 \pm 0.10) \cdot 10^{-3}$

As can be seen in Table 7, and disregarding the standard error arising from the variance of the two acquired data sets, the obtained mean values for the double integrated signal intensities differ by $0.6 \cdot 10^{-3}$. The error of the individual values of each data set is computed via Gaussian error propagation assuming a 5 % error of the protein concentration and an error of

5 % of the used volume. Errors of the EPR signal intensity due to minor changes of the placement in the resonator as well as possible errors of the double integration routine of the used software (Bruker Xenon) are disregarded: Using this approach, an error of $\sim 0.7 \cdot 10^{-3}$ is calculated. This shows that the obtained mean double integral intensities are identical within the accuracy of the experiment. From this data, it is concluded that the labeling site is readily accessible for the trityl labels.

The labeling efficency of **6-9** was determined using the inbuild spin counting experiment of the Bruker EMX nano *cw* X-band EPR spectrometer. The labeling efficency was calculated as the the ration of the spin concentration and the protein concentration as determined by UV/Vis spectroscopy. The spectra recorded for this purpose are shown in appendix A.

To determine the labeling efficency of **6-9**, the in-built spin counting experiment of the Bruker EMX nano cw X-band EPR spectrometer was used to determine the spin concentration of a given sample. The labeling efficiency was then calculated as the ratio of the spin concentration and the protein concentration as determined by UV/Vis spectroscopy. The spectra recorded for this purpose are shown in appendix A.

Table 8: Labeling efficiencies for the labeling of CYP101 C58 with **1**, **6**, **7** and **8** and the labeling of FeoB with **9**

Label	**1**	**6**	**7**	**8**	**9**
[%]	80	78	85	36	56

The labeling efficiencies are shown in Table 8. For **9**, the *E. coli* FeoB mutant R152 with the unnatural amino acid 4-azido-L-phenylalanine was used, because **9** specifically targets unnatural amino acids and no suitable mutant of CYP101 was available at the time. The labeling efficiencies of **6** and **7** match those of the commercially available **1**, which makes them very well suited for protein labeling. **8** shows only a modest labeling efficiency of 36 %, which is lower than results for labels employing the same labeling strategy for which labeling efficiencies up to 70 % were reported.[88] This is attributed to the relatively mild labeling conditions that were used here. This comparatively low labeling efficiency will make distance measurements for the determination of trityl trityl distances in doubly labeled protein difficult. However, while **1**, **6** and **7** form bonds to cyteins via relatively unstable disulfide bridges that will be broken under reducing conditions, **8** forms thioethers, which are more stable against a large variety of conditions and allow the use of this label for measurements within cells.[14, 89] **9** allows for the targeting of unnatural amino acids via click reactions[90] where it performs similar to an analogous approach used for an Alexa fluorophore and an inversely

functionalized nitroxide spin label.[91] Its characteristics make it especially suited for orthogonal labeling strategies and for proteins that contain cysteines in essential positions that cannot be removed without rendering the protein dysfunctional. In addition, it can attach to oligonucleotides either via click reactions or via palladium catalyzed cross coupling reactions.[92]

Having demonstrated to which efficiencies the synthesized spin labels will label, the next obvious step is to put them to a test in an actual distance measurement. The protein used so far, *pseudomonas putida* CYP101, carries a heme group which contains an iron(III) cation. Measurements between spin labels and native metal cofactors are very desirable, because such cofactors are often vital for the biological function of a protein. It has been demonstrated that EPR derived distance constraints can be used to localize a metal center in a protein, and thereby deliver valuable insights into a biological process.[93] Iron(III) is a d^5-system which can exist in a $S = {}^5/_2$ high spin state or a low spin $S = {}^1/_2$ state. In the absence of a substrate that can bind to the heme group, the iron exists usually in the low spin state. For the sake of EPR distance measurements, this is an advantage, since the high spin state opens a large number of different relaxation pathways that lead to so fast relaxation times that this poses a difficult to overcome challenge for the distance measurement. Either way, a CYP101 protein labeled with a trityl shows a combination of a very fast relaxaing spin (iron) and a rather slow relaxing spin (trityl). For such disparate spin systems, the RIDME experiment is uniquely suited for the distance measurement. In the previous section, it was concluded that of the commonly used distance measurement techniques, RIDME was the least suited to determine a trityl-trityl distance. In that instance, two very slow relaxing spins were investigated. While successful RIDME was demonstrated in section 2.2.3, this is a difficult condition for the experiment. Here, on the other hand, one spin relaxes significantly faster than the other does, so that a case is constructed where one spin for all intends and purposes completely relaxes and the other does not show relaxation. This constitutes the ideal fringe case for the RIDME sequence. The superiority of the RIDME sequence for the determination of label-iron(III) distance has been previously demonstrated on the same protein labeled with **1**.[87] This previous study showed that a good temperature to perform nitroxide-iron(III) RIDME is 25 K.[87] At this temperature, the iron(III) spin relaxes completely in 30 µs or less. Accordingly, the RIDME experiments were performed with a separation T of 25 µs for trityls and 30 µS for nitroxides, an initial τ_1 of 350 ns and a τ_2 of 1.6 µS. The reason for the minor difference in T between trityls and nitroxides is that for trityls, the iron (III) seemed to relax

slightly faster, so that complete relaxation was reached at a shorter value. Since a shorter T improves the SNR, the shorter time was chosen for the trityls.

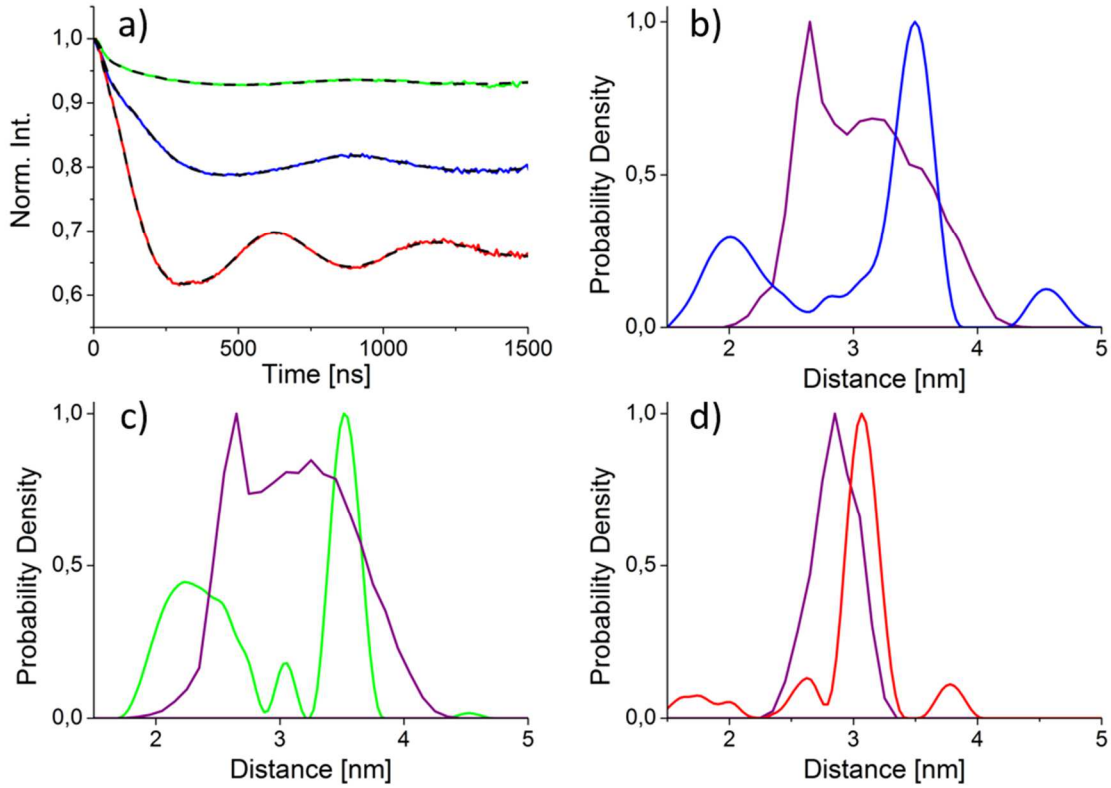

Figure 46: Q-band RIDME time traces of CYP101 mutant C58 labeled with **7** (blue solid line), **8** (green solid line) and **1**(red solid line) overlayed with the corresponding DeerAnalysis fits (black dashed lines). The corresponding distance distributions are shown in b) for C58T1, c) C58T3 and d) C58R1. The purple lines are the mtsslWizard predictions.

RIDME was performed on CYP101 using **7** ($C58T_1$) , **8** ($C58T_3$) and **1** ($C58R_1$) for reference. These labels were chosen because **7** is the direct analogue to **1**, and **8** enables in cell distance measurements, which will be important at a later point. The time traces and derived distance distributions are shown in Figure *46*. For $C58T_1$, a well modulated time trace with a modulation depth of 20 % and a corresponding SNR of 20.84 $min^{-1/2}$ was obtained. For $C58R_1$, a higher modulation depth of 35 % was obtained, with a SNR of 13.08 $min^{-1/2}$. Thus, TSL1 gives a 60 % better SNR than **1**, which matches expectations since in the experiment, virtually all of the trityl spectrum can be excited, while only 40 % of the wider nitroxide spectrum can be excited. For $C58T_3$, a modulation depth of only 7 % was achieved, with a SNR of 10.85 $min^{-1/2}$. The decrease of SNR relative to $C58T_1$ is due to the lower labeling efficiency. The modulations depth of the three samples differs greatly, from the rather good value of 35 % to the rather poor 7 %.

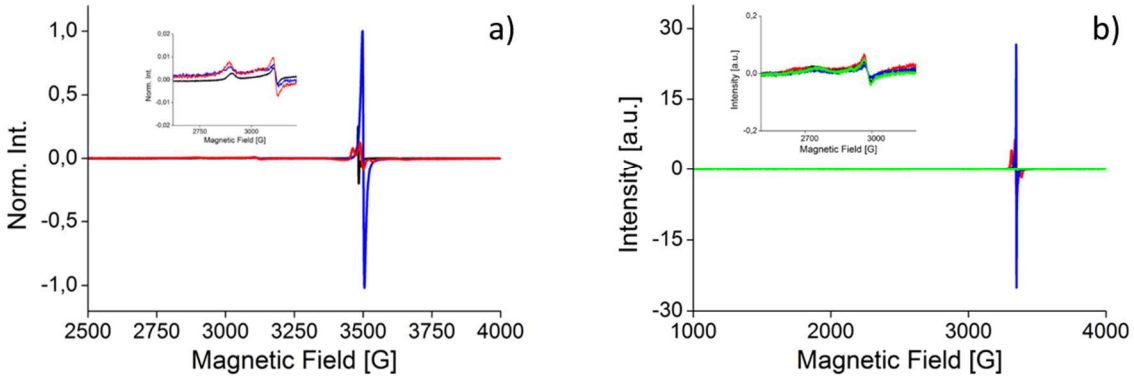

Figure 47: a) X-band cw-EPR spectra of the samples used for the RIDME experiments of CYP101 C58R_1 (red), CYP101 C58T_1 (blue) and CYP101 C58T_3 (black) at 10 K. The inset shows a magnified part of the iron signal. The spectra were normed on the maximum intensity of the trityl signal of CYP101 C58T_1. b) X-band cw-EPR spectra of samples of CYP101 C58R_1 (red), CYP101 C58T_1 (blue), CYP101 C58T_3 (black) and unlabeled CYP101 at 10 K. The inset shows a magnified part of the iron signal.

A know issue with *pseudomonas putida* CYP101 is that the iron(III) content of the protein can vary greatly, because not all proteins of an expression batch will carry a heme group. During the purification process following the expression of the protein, steps were taken to separate those proteins that did carry a heme group from those that did not to achieve the highest possible iron(III) content for the samples. Still, a difference in the iron(III) concentration is the most likely explanation for the differences in modulation depth. To test this hypothesis the relative iron content of the CYP101 samples was determined by recording the cw X-band EPR spectra of the respective samples of equal protein concentration (200 µM) and equal sample volume (80 µL). The relative iron contents were determined as the ratio of the double integrals of the iron (III) signals. The EPR signals gave integrated intensities of 263 a.u. (CYP101 C58R_1), 171 a.u. (CYP101 C58T_1) and 91 a.u. (CYP101 C58T_3). The ratios of the double integrated iron (III) signals match the ratios of the modulation depths. To ensure that the difference in the iron content is a random effect of the expression in different batches of proteins and not the consequence of the labeling procedure or label-heme interactions, a second set of samples was prepared were protein from the same batch was labels with **7**, **8**, **1** and not at all. The intensity of the iron (III) signal was determined as described above. A superposition of the respective spectra is shown in Figure 47b. It was determined that within the accuracy of the experiment, the intensity of the iron (III)) was identical for all three samples. To ensure the reproducibility of the result, all RIDME measurements were repeated with the new set of samples. (see Appendix B) For CYP101 C58T_1 and CYP101 C58R_1, modulation depths of 26 % and 30 % were achieved. The difference is within the error one would expect due to experimental circumstances and uncertainties in the background

correction. CYP101 C58T$_3$ was, unfortunately, only at 6 %. This indicates that differences between **7** and **1** are satisfyingly explained by differences in the iron (III) content, while for **8**, different effects need to be considered. Unpublished work by J.-J. Jassoy on different proteins indicates that **8** suffers from unspecific labeling. This means that some spin labels bind non-covalently to the surface of the protein. These unspecifically bound spin labels would contribute to the signal intensity, but due to their random placement on the protein surface, they would not contribute to the dipolar modulation. This would explain the reproducable difference in the modulation depth. The distance distributions obtained through Tikohonov regularization of the RIDME time traces are shown in Figure *46*b-c, together with *in silico* predictions made using the program mtsslWizard[94]. For CYP101 C58T1, a bimodal distance distribution with mean distances of 2.0 nm and 3.5 nm with standard deviations of 0.2 nm and 0.15 nm was obtained. A similar distribution with mean distances of 2.4 nm and 3.5 nm with standard deviations of 0.25 nm and 0.12 nm was attained for CYP101 C58T3. In contrast, a monomodal distribution was obtained for CYP101 C58R1, with a mean distance of 3.06 nm with a standard deviation of 0.11 nm. The difference in the mean distance and the width of standard deviation between the trityl labels and **1** is readily explained by the difference in linker length. The T1 chain of the trityl label is three bonds longer than the R1 chain. Since a C-C single bond has an approximate length of 154 ppm or 1.54 nm, this matches the difference in the mean distance, and also explains the larger width of the distribution.

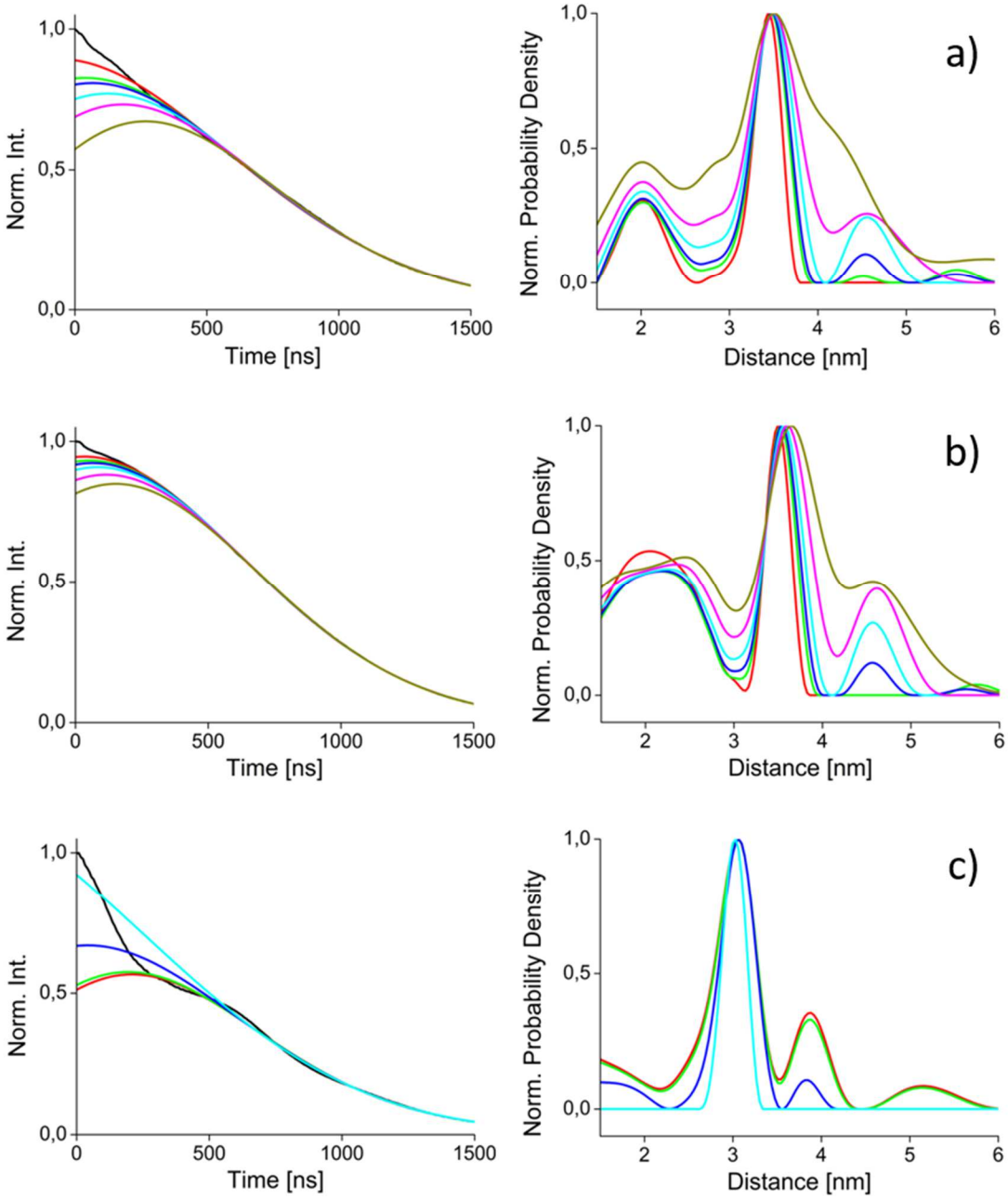

Figure 48: Original RIDME time traces (black) and different background 3rd order polynomials and the accompanying distance distributions for CYP101 C58T1 (a), CYP101 C58T3 (b) and CYP101 C58R1

The longer linker cannot explain the bimodality seen in the trityl derived distance distributions. To explain this, it must first be established that the bimodality is indeed a real feature and not an artifact of the background correction. To do so, several 3rd order polynomials have been fitted to each timetrace. The raw data was divided by the different background functions and the distance distribution extracted via Tikhonov regularization (DeerAnalysis2016) To ensure the comparability of the distance distributions, the regularization parameter was fixed to 100 for all timetraces. Only features that prevail regardless of the background function are assumed to be real. For the results of this process,

see Figure 48. The results demonstrate that the bimodality is a real feature. To explain it, the *in silico* conformer clouds generated by mtsslWizard must be taken into account.

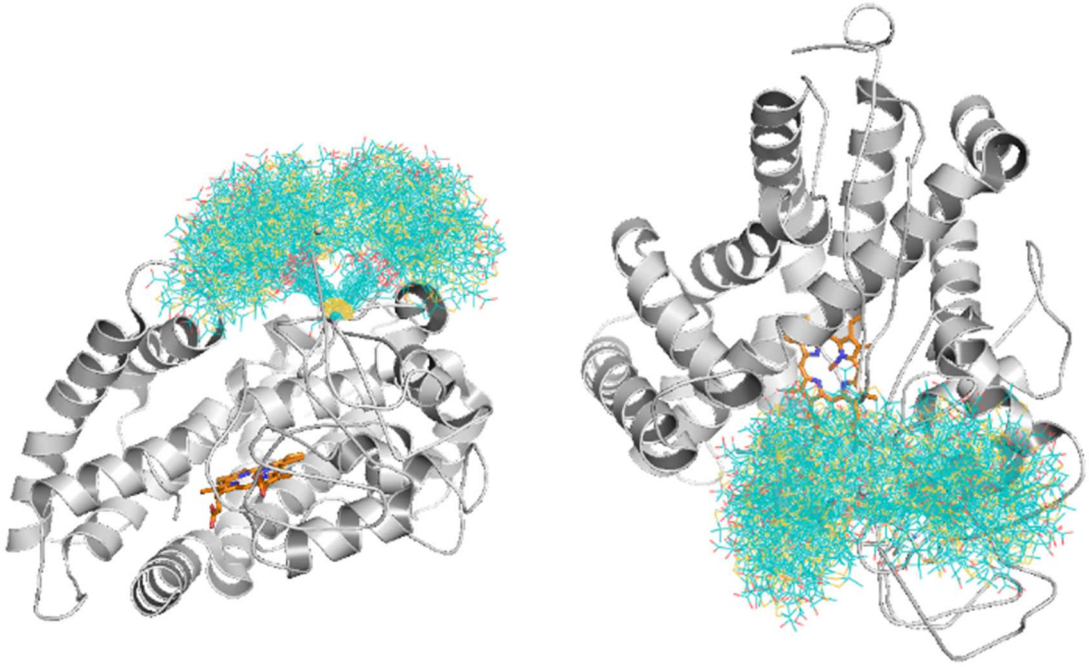

Figure 49: mtsslWizard conformer cloud for CYP101 C58T3 from two different angles.

In the in silico predictions based on a crystal structure (pdb 3L61) it is clearly visible that two distinct conformer clouds are formed. This is because a loop reaches into the space in between the two clouds and prohibits the bulky trityl to occupy that space. The sterically less demanding **1**, on the other hand, is much less affected by this loop, and therefore can assume a monomodal distribution.

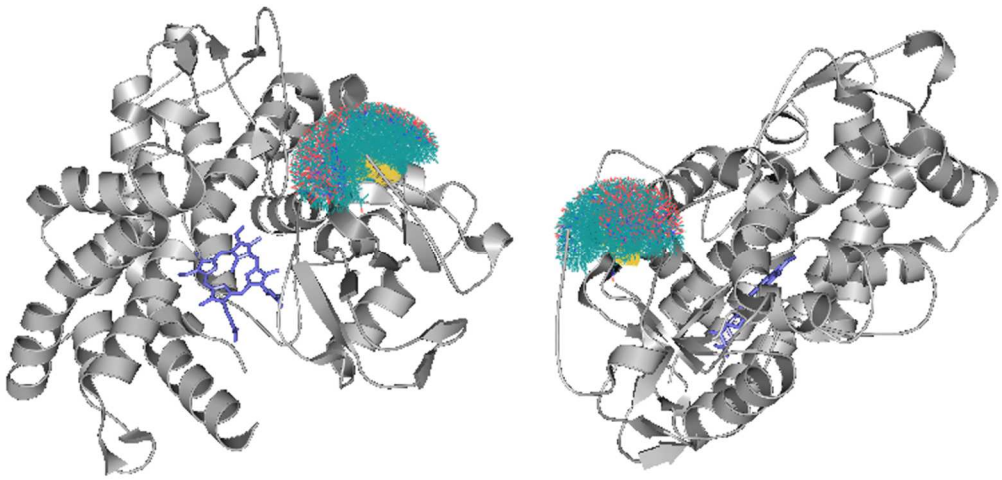

Figure 50: mtsslWizard conformer cloud for CYP101 C58R1 from two different angles.

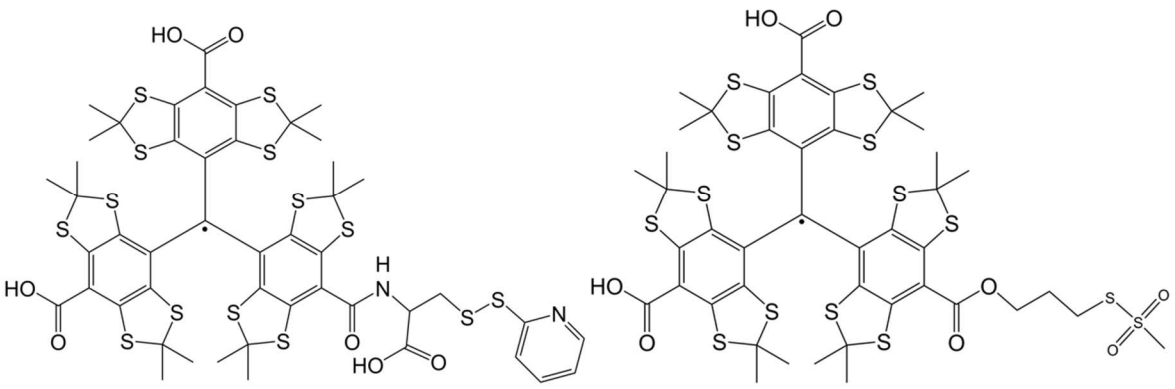

Figure 51: Chemical structures of literature trityl labels **10** (left) and **11** (right).

In the literature, two other trityl spin labels for proteins, **10**[53] and **11**[83], have been used. The distance distribution obtained for **10** shows a standard deviation of 0.37 nm, the distance distribution for **11** shows a standard deviation of 0.19 nm. These distributions are broader than the distributions that were obtained for **7** and **8**, which showed standard deviations of 0.15 nm and 0.12 nm, respectively. It is easily understood that **11** exhibits a wider distribution than **7**, since its linker is longer by one CH_2-group. This cannot be the reason for the much larger distance distribution of **10**, since it has the same number of rotatable bonds as **7**. However, the width of a distance distribution depends on the labeled protein and the labeling site. A direct comparison of results that were obtained on different kinds of samples does not necessarily yield a meaningful result.

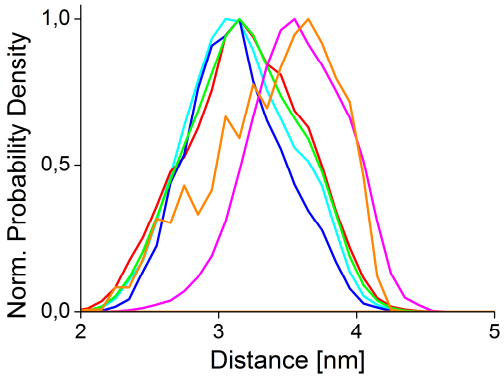

Figure 52: In silico distance distributions for CYP101 C58T1 (cyan), C58T3 (green) as well as the same mutant labelled with **6** (blue), **9** (magenta), **10** (orange) and **11** (red)

In order to produce a realistic estimate of the of the relative performance of the various spin labels in terms of the width of their distributions, **10** and **11** were incorporated into the mtsslWizard. In silico distance measurements on CYP101 C58 were performed for **6**, **7**, **8**, **9**, **10** and **11**, in which the label-iron(III) distance was determined (see Figure *52*). The results indicate that **6**, **7**, **8** and **11** give distance distributions of similar width, although **11** shows the

widest distribution of these four by a small margin. The narrowest predicted distance distribution was obtained for 9, but at a longer mean distance than all other labels by approx. 0.6 nm. This demonstrates that the label is very rigid. **11** gives the widest distance distribution, which is much wider than the predictions obtained for all other labels.

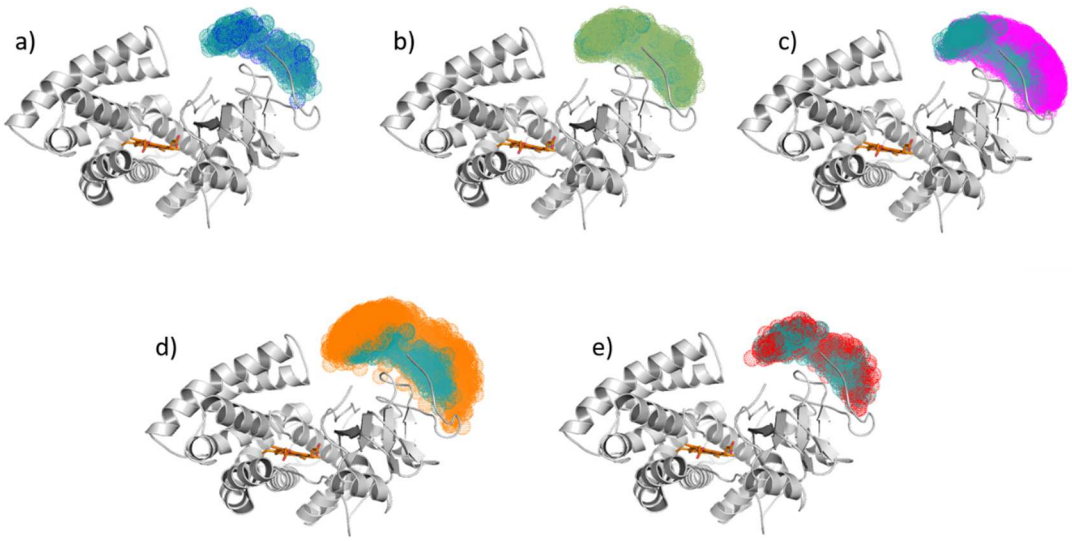

Figure 53: Superposition of the conformer clouds generated by the mtsslWizard for CYP101 C58T1 (cyan) with a) CYP101 C58 labeled with **6** (blue) b) CYP101 C58T3 (green), c) CYP101 C58 labeled with **9** (magenta) d) CYP101 C58 labeled with **10** (orange) e) CYP101 C58 labeled with **11** (red).

Table 9: Calculated accessible volumes for labels **6**, **7**, **8**, **9**, **10** and **11**

Label	**6**	**7**	**8**	**9**	**10**	**11**
Volume [Å^3]	1687	2779	4220	3863	7887	3317

As a means to illustrate the different flexibilities and the accessible volumes for each spin label, the conformer clouds generated by mtsslWizard were superimposed (see Figure 53) To quantify the difference of the accessible volume, the program VVV[95] was used to calculate the volumes of the individual conformer clouds (see Table 9). From this calculations, it can be concluded that **6** and **7** show a smaller accessible volume than **11**, which can be explained by the fact that they have a linker that is shorter by one CH_2-group. The smaller volume of **6** relative to **7** is likely due to the ester group, because it increases the steric demand of the trityl. The volumes of labels **8** and **9** are larger than that of **11** by a small margin, which in turn my be rationalized because they have slightly longer linkers. For **10**, a volume twice the size as the average volume of the labels **6-9** and **11** was calculated. This highlights that this label appears to give very broad distance distributions, which is in good agreement with published experimental data.[53] The comparison presented here shows that **6** and **7** perform

better than previously published spin labels, if the width of the predicted distance distributions and their accessible volume are considered.

To demonstrate that in cell EPR distance measurements are feasible with trityl radicals, *xenopus laevis* oocytes were injected with a solution of CYP101 C58T3 in TRIS buffer using a Drummond Nanoject II microinjector following the protocol published by Azarkh et al.[50] For details, see materials and methods. The thusly-prepared sample was subjected to trityl-iron(III) RIDME as described for the *in vitro* measurements. In contrast to the in vitro measurements, which were averaged for 2.3 h each, the significantly reduced effective spin concentration causes a severe drop in SNR, and therefore the RIDME time trace was averaged for 80 h.

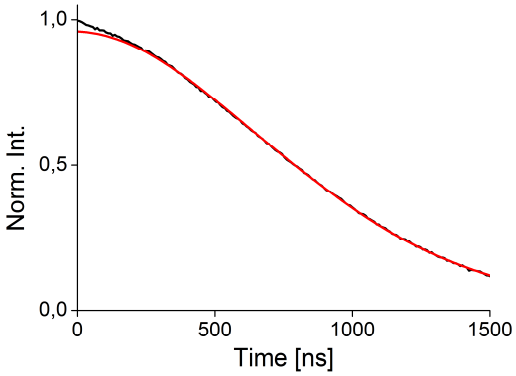

Figure 54: Original timetrace of the in-cell RIDME on CYP101 C58T$_3$ (black) and its DeerAnalysis fit (red)

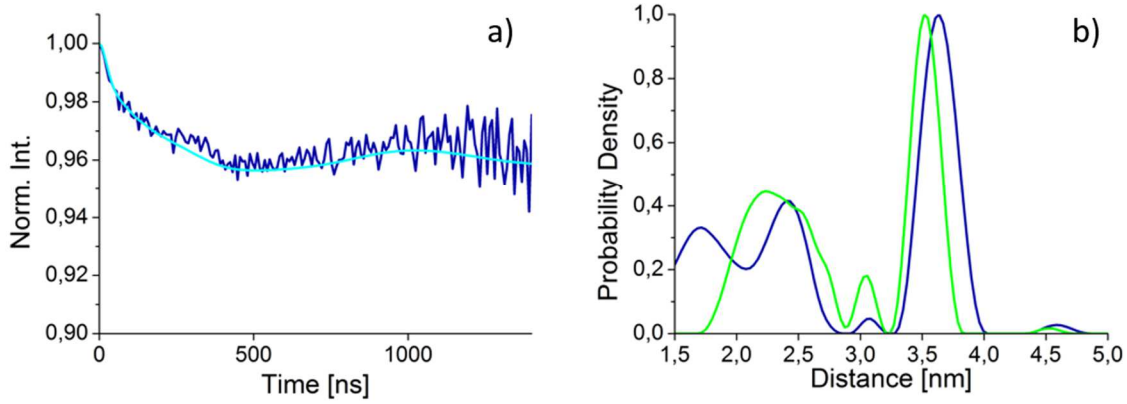

Figure 55: a) The background corrected timetrace of the in-cell RIDME on CYP101 C58T$_3$ (dark blue) and its DEER Analysis fit (cyan). b) The corresponding distance distribution (blue line) overlayed with the in vitro distribution (green line).

The obtained RIDME time trace was background corrected using a polynomial of the same order as for the in vitro time trace revealing a modulation depth of 4% and a SNR of $1.97\text{min}^{-1/2}$. Compared to Q-Band PELDOR results published for gadolinium(III) spin

labels[14], a modulation depth of the same order of magnitude was achieved. It should be stressed though that the low modulation depth is due to the difficult to control iron content of the CYP101 protein. In addition, the *xenopus laevis* oocytes contain 40 μM of manganese(II). This may reduce the modulation depth as a result of relaxation enhancement of the iron center compared to the in vitro experiments of the identically labeled protein. The SNR achieved for the in cell measurement is lower than the SNR obtained for the in vitro experiment by a factor of 10. This is due to the fact a lower amount of proteins by roughly a factor of 10 was injected into the proteins. No exact SNR value was given for the previously mentioned Q-band gadolinium(III) PELDOR measurements, but its SNR is visibly better than the value achieved in the measurement presented here. The most likely reason for this is the 10 fold higher label concentration used for the protein sample in the Gd(III) case. For an in cell PELDOR measurement on a gadolinium(III) model compound, a very good SNR was achieved. Again, a spin concentration one order of magnitude higher was used, if labeling efficiencies are also taken into account. Other works on Gd(III)-Gd(III) distance measurements in *E. coli* cells show a slightly increased SNR. However, these works suffer from a weak modulation depth of 0.6% or less, while being performed at *in cell* concentrations which are again one order of magnitude higher than what is presented here.[96] Concentrations of this order of magnitude could not be achieved for CYP101, and also, they are beyond relevant in cell concentrations. However, distance measurements on gadolinium(III) at W-band have been reported which show better SNR than the timetrace presented here, while using spin concentrations as low as 20 µM. These results are very encouraging, although the reported timetraces did not show any modulations, except the zero time and the initial signal decay, and also yiedeld distance distributions that were very broad. In defense of this studies it should be stressed that the broad distributions obtained there are due to the high flexibility of the investigated samples.[97]

The distance distribution acquired from the in cell RIDME is very similar to the distance distribution obtained from the in vitro experiment using the same spin label. This supports that the background treatment is correct and reproducible between different sample preparations. The mean distances of the distribution are 3.6 nm and 2.45 nm with respective standard deviations of 0.16 nm and 0.2 nm. Further distance peaks of low intensity at 1.8 nm and 3.1 nm are interpreted as noise artifacts. The mean distance of the in cell distribution is shifted by roughly 1 Å against the in vitro distance distribution, and the obtained distance distribution is also slightly broader. This can be rationalized either as the effect of the noise on the Tikhonov regularization performed and the DeerAnalysis fit. A different possible

explanation is a slight conformational change of the CYP101 under in cell conditions. Based on the current data, it is not possible to distinguish between the two cases, but future studies on different labeling positions will allow to estimate if structural changes occur under in cell conditions, and if so, to which extend. The distance of 3.5 nm measured in the trityl-iron(III) distance measurement reported here represents the current upper limit for distances that can be accessed reliably using trityl spin labels. After a recorded time periode of 1000 ns, the SNR decreases significantly, and the noise reaches a level where distance measurements without previous knowledge of the expected mean distance become unreliable. Especially in combination with the low modulation depth, this is a severe issue, but should be much less of a problem in cases where a high modulation depth is achieved. This stresses the point that future research will have to focus on an improvement of the labeling procedures, since higher labelling efficiencies will also lead to a better SNR.

2.3.1 Summary

In this chapter, four new trityl spin labels were presented and characterized by *cw*-EPR. Their first application in EPR distance measurements at the example of a trityl-iron(III) RIDME on *pseudomonas putida* CYP101 was presented both in vitro and in cell. To the best of my knowledge, this is the first in cell distance measurement using trityl spin labels ever reported as well as the first in cell distance measurement between a spin label and a native metal cofactor. It was demonstrated that the presented trityl spin labels work very well for the RIDME experiment, and exhibited a better SNR than nitroxide labels. Compared to gadolinium(III) labels, they allow the extraction of unambiguous distance distributions, while distance measurements on gadolinium(III) labels can be difficult to interpret due to higher harmonics of the dipolar coupling which cause additional peaks in the distance distribution. It has been demonstrated in the literature though that at least for model compounds, these higher harmonics effects can be compensated for.[15, 98] An additional drawback of gadolinium(III) labels is that they cannot be used for room temperature distance measurements because they show very fast relaxation times.[79] For the discussed advantages over other kinds of spin labels, the presented trityl spin labels are a valuable addition to the spin label repertoire available for EPR distance measurements and hold promise for future studies under truly biological conditions.[98]

2.4 Conclusion

In this part of the thesis, protocols for the use of four different pulsed distance measurement techniques as well as *cw*-EPR distance measurements were established and their relative performance in terms of modulation depth and SNR were compared for two bistrityl model compounds. It was found that DQC and SIFTER perform best, while PELDOR suffered from significantly worse SNR and RIDME did not deliver unambiguous results for model compound **5**. Further, four new trityl spin labels were characterized by means of *cw*-EPR and their spectroscopic characteristcs were determined. Their labeling efficiency was determined for a *pseudomonas putida* CYP101 mutant , where it was found that labels **6** and **7** perform equally well as the commercially available **1**. Labels **8** and **9** showed a significantly lower labeling efficiency. All trityl labels were tested for degradation during the labeling procedures, and none was found. Labels **7** and **8** were used in trityl-iron(III) RIDME distance measurement under *in vitro* conditions. The results were compared to measurements using **1**. It was found that **7** performs equally well as **1** in terms of modulation depth and better in terms of SNR. **8**, unfortunately, performs worse in terms of modulation depth, but comparable in terms of SNR. Lastly, **8** was used for the first *in cell* EPR distance measurement using a trityl spin label. The measurement was performed after injecting the protein solution into *xenopus laevis* oocytes. The measurement achieved a better modulation depth than published in cell measurements on gadolinium(III) spin labels and modified nitroxide labels. It was possible to conduct these measurements at a significantly lower protein concentration than previous measurements using other labels, although this lead to a lower SNR.

3 Single electron transfer processes monitored by EPR

3.1 Introduction

A chemical reaction in general involves the exchange and redistribution of electron density between the reaction partners. While this is often only a principal shift of polarities in a closed shell, many processes are known were single electron transfer steps play a crucial part in a reaction. The easiest example for such a reaction is a redox reaction, e.g. involving metal ions of different electrochemical potential. When these kind of reactions occur in inorganic salts or oxides, these processes are well understood and in the form of redox chemistry subject of the basic training all undergraduate students of chemistry receive, but electron transfer processes also occur in organic or metalorganic complexes and reaction cycles[99], where most often these reactions go via transient intermediates with short live spans that are not easily detected. For such reactions, often only the educt and product of a reaction are certain, but the mechanism is obscure and several competing proposed mechanisms are discussed. In many cases, the understanding of a process or the knowledge of the structure of an intermediate can greatly improve the application of a process. Where these proposed mechanisms or assumed molecular structures contain open shell species, they can be investigated via EPR spectroscopy. As was mentioned previously, EPR is uniquely suitable for the investigation of radical species, since it can give a definite answer whether a moiety contains a radical or not, and often allows detailed conclusions about the kind of radical that is detected, e.g. via the g-value and the assigned hyperfine coupling constants. However, an issue that must be taken into consideration when dealing with radical intermediates is their short life span, which may lead to an overall low concentration of the radical species. While EPR has a high sensitivity compared to other spectroscopic methods such as FTIR or NMR, commercially available X-band EPR spectrometers require a minimum concentration of 1000 spins/G according to the manufacturer, which is not easily realized. In order to overcome this limitation, a known approach is to stop the reaction by shock freezing it and thus preserve a state where a sufficiently high radical concentration still exists (rapid freeze quench). This method has been successfully demonstrated to work e.g. for the intermediates of biochemical reactions.[100] Another approach is to generate the radical continuously inside the EPR spectrometer or in a fashion that it will be transported there immediately after its generation. The latter approach can in many cases be realized via electrochemical oxidation or by using chemical oxidation reagents.

Here, the designs for two different setups for the electrochemical generation of radicals and their subsequent detection by EPR are presented. One is a classical three electrode electrolysis cell and the other an electrochemical flow through cell for bulk electrolysis. Both setups were then initially tested with tetramethylphenyldiamin (Wurster`s reagent, **12**). Then, they were applied in the investigation of the electronic behavior of radical salts of bis(2-pyridylmethyl)azine (BMPA, **13**) and bis(2-pyridylmethyl-5-tert-butyl)azine (tBu-BMPA, **14**), in mechanistic investigations of copper catalyzed coupling reaction on tetrahydroisoquinolinone (THIQ, **15**), and in the investigation of the mechanism of the McMillan catalytic cycle.

3.2 Design of combined electrochemical/EPR setups

3.2.1 Potentiostatic electrolysis cell (electrochemical setup 1)

The aim in the development of this setup was to assemble a cheap, easy to handle potentiostatic electrolysis cell to generate organic radicals inside an EPR spectrometer and immediately detect them, thus giving access to the EPR spectra of short lived organic radicals.

The general setup for any potentiostatic cell consists of a working electrode, a counter electrode and a reference electrode. In this setup, the current flows between the working and the counter electrodes, whereas only a small current flows between the working- and

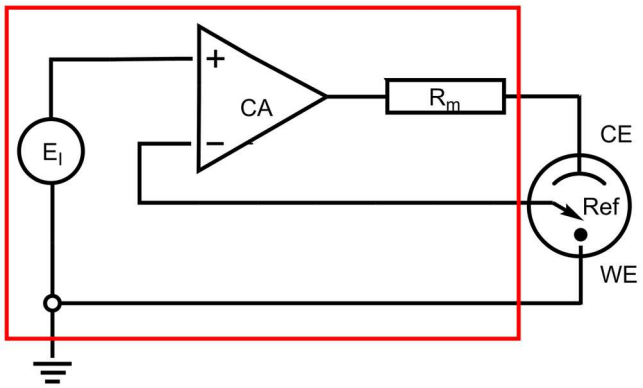

Figure 56: Schematic representation of a potentiostatic three-electrode setup. Here, WE is the work electrode, CE is the counter electrode, Ref is the reference electrode. R_m is the current measurement resistor, CA is the control amplifier, and E_i is the input source. The parts inside the red box are a possible, and very basic, arrangement for a potentiostat.

reference electrodes.

This general scheme leaves five components to be considered in the design of the electrochemical cell, as they will determine its electrochemical behavior. These components are the three mentioned electrodes that comprise the cell, the potentiostat, and the actual cell itself.

For the work- and the counter electrodes, the requirements to be considered are that their material is a good conductor, and is resistant to both chemical reaction with the intended investigated compounds and solvent, and also, they must be resistant to redox reactions. To avoid an offset in their electrochemical potentials, the same material has to be used for both electrodes. In the present work, a platinum wire with a diameter of 0.1 mm was used for both electrodes. The wire of the counter electrode was chosen to be 15 cm long, while for the working electrode, the wire was isolated with shrink tube with the exception of the last 3 cm. The reason that a counter electrode with a much larger surface than the work electrode is used

is that the polarization of the work electrode is controlled by adjusting the current at the counter electrode. If the surface of the counter electrode is large, than only a comparatively low current density is needed for that, and the associated potential drop is small. The latter part is important for two reasons. If the counter electrode is polarized for a very high potential, it is likely to cause unwanted side-reactions. Also, all potentiostats operate with a maximum inner voltage, the so-called compliance voltage. If the application of the full compliance voltage to the counter electrode is not sufficient to maintain the desired potential at the working electrode, it will not be possible to achieve this voltage at the working electrode. This is especially important for badly conducting solvents, where a severe potential drop at the solvent(the so-called IR-drop) is expected.[101]

A reference electrode has to have a constant potential and must reach its equilibrium potential shortly after the change to the applied voltage. Several such systems are known in literature, e.g. the normal hydrogen electrode or the silver-silverchloride electrode or calomel electrodes. For the reference electrode, a saturated calomel electrode was used. The electrode was calibrated against the ferrocene/ferrocenium ion pair (SCE vs. Fc/Fc^+ = 3.03 V in acetonitrile).

As a potentiostate, a home-build device was used. The potentiostate has a compliance voltage of 15 V and an operating voltage range of +/- 2 V. It works in the current range between 1 µA and 10 mA.

For an electrochemical cell, the EPR flat cell by Wilmad Glass was used. Due to its narrow solution film in the flat measurement window, it allows for the detection of *cw*-EPR spectra of lossy samples. However, it has an unusual and impractical design for electrochemistry, since it facilitates an inhomogeneous potential in the cell due to the difference of the distance between the counter electrode and different points along the working electrode, especially since in badly conducting solvents a considerable IR drop is to be expected. The IR drop is the electrical potential difference between the two ends of a conducting phase during a current flow. This voltage drop across any resistance is the product of current (I) passing through resistance and resistance value (R).

Figure 57: Potentiostate, glassware and work- and counter electrode, and saturated calomel reference electrode (from left to right)

To test the functionality of the setup, tetramethylphenyldiamin (**12**) was used. This compound, commonly known as Wurster`s reagent, forms distinct blue radical cations (Wurster`s blue) under electrochemical oxidation at an oxidation potential of 0.276 V against a standard hydrogen reference electrode, which results in a theoretical oxidation potential of 0.035 V against a saturated calomel reference electrode.[102] Wurster`s blue was chosen as a test substance because both its electrochemical and EPR properties are know from literature, and it had previously been used as a test system for combined electrochemical and spectroscopic applications.[103] For the test, a 1 M solution of **12** in HPLC grade acetonitrile (VWR) with added 0.01 M of tetrabutylamoniumphosphate hexafluorophosphate was used. The applied potential was varied in a range of 0.05 V and 0.5 V. Between each experiment, the flat cell was emptied and washed to avoid contaminations from the previous run. The electrolysis was run for 5 minutes, and then an EPR spectra was recorded on a Bruker EMX micro X-band *cw*-spectrometer with a HS4118 resonator. It was found that the best resolution in terms of the hyperfine coupling constants of the amine was achieved with a potential of 0.1 V. The rational for that is that with a lower potential only small concentrations of radical were generated, so that the obtained spectra were very noisy, and also radical was only present in close proximity to the working electrode, were the magnetic field was influenced by the platinum wire. With higher potential applied, the signal-to-noise ratio was much better, however, the linewidth increased probably because the radical is only generated along the surface of the working electrode, so was inhomogeneously distributed with a high local concentration, which is likely to have caused a broadening of the EPR spectrum.

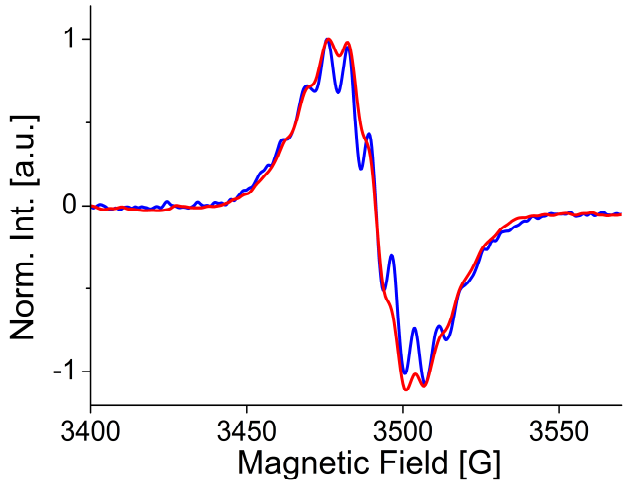

Figure 58: X-band *cw*-EPR spectra of Wurster`s blue generated with the potentiostatic setup at 0.1 V (blue) and at 0.5 V (red)

Via double integration of the recorded spectra, relative spin concentrations of the two measurements were obtained and a ratio 14 :1 was found. This supports the previous statement about the cause of the increase in linewidth for higher voltages. It should be stressed that with the used flat cell and the high losses of microwave intensity due to the polar solvent, absolut values for the spin concentration cannot be given. Since the detection of unstable radicals requires their continuous generation to balance out losses due to decomposition, the EPR spectra were also acquired during continuous electrolysis within a time span of 30 minutes at 0.1 V and 0.3 V. It was found that at a voltage of 0.1 V a maximum signal intensity was reached after 10 minutes, which was then kept stable within the accuracy of the experiment for 70 minutes, after which monitoring was stopped. Surprisingly, for a voltage of 0.3 V the signal intensity, after reaching a maximum after 4 minutes, dropped until after 15 minutes, a stable intensity was reached. Since Wurster`s blue is a persistent radical in the time frame of the experiment, all intensity losses are ascribed to diffusion and convection, which causes the radical to be outside the resonator. A possible explanation for the behavior of the signal intensity under constant use is that due to high currents, the local concentration of tetramethylphenyldiamin is reduced, which causes the signal intensity to drop until after 15 minutes, a diffusion controlled equilibrium is reached.

To summarize, a potentiostatic electrolysis cell in which *in situ* generated radicals can be immediately detected via *cw*-EPR was constructed and characterized using a stable and well described radical. However, the presented setup faces some limitations, which should be kept in mind for its applications. In the current setup an aqueous reference electrode is used, which induces a junction potential between the organic and watery phase of the cell, which is

dependent of the used solvent, cannot be measured and may change over time. Therefore, all oxidation potentials one could obtain with this setup must be considered to contain a small error. The size of that error can be estimated if the potential is measured in the presence of an internal standard, e.g. ferrocene. It is also possible to calibrate the reference electrode with such a standard prior to a measurement.

3.2.2 Electrochemical flow cell (electrochemical setup 2)

The shortcomings of the setup described in 3.2.1 became obvious during testing and application (see chapters 3.3, 3.4 and 3.5). It was therefore decided to separate the electrochemical cell from the EPR cell to achieve optimal conditions for both parts of the experiment. Still pursuing the goal to detect short-lived radicals, a flow through system where a solution of the radical precursor compound was pressed through an electrochemical flow cell to be oxidized was envisioned. From there, the freshly generated radical should flow through the EPR cell so that a spectrum could be recorded.

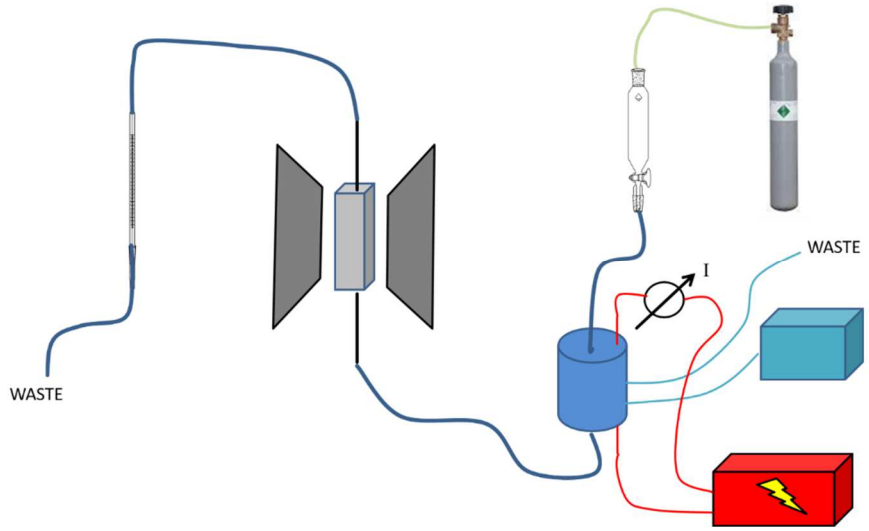

Figure 59: Schematic build of the electrochemical flow cell setup

The setup was constructed along the example of a setup that was previously used by Grampp et al.[70b], although the electrolysis cell was chosen to be of a larger circumference. This gives a larger electrode surface and allows for a higher throughput.

Figure 60: Electrochemical Flow cell

The electrolysis setup for the flow-cell consists of a PCTFE cylinder with two compartments, which are separated by an inner cylinder made from porous PTFE (pore size 50 μm). Both compartments are filled with coal fleece, which is contacted with otherwise isolated tungsten wire. The coal fleece is the electrode material for both working- and counter-electrode. The actual inner volume of the porous PTFE cylinder can be changed via a PTFE inset according to the requirements of the application, ranging from as large as 20 mL (for an empty cylinder) to as little as 2 mL. The electrolysis is controlled by a Korad KA3005D laboratory power supply unit. The power supply unit sets limitations for the maximum voltage and current, stopping wherever the set maximum is reached first, thus allowing to limit the voltage for cases where over oxidation might be an issue. The counter-electrode compartment is filled by a separate pump circuit with the same solvent and supporting electrolyte as used for the sample solution. The sample solution is pressed through the flow cell`s working electrode compartment via an adjustable nitrogen gas pressure. From the working electrode compartment the solution is pressed through a capillary placed in the resonator of the EPR spectrometer. Since the setup does not include a reference electrode, and also, the homogeneity of the potential inside the electrochemical flow cell cannot be guaranteed, the best parameters for a given electrochemical compound need to be tested individually for each application.

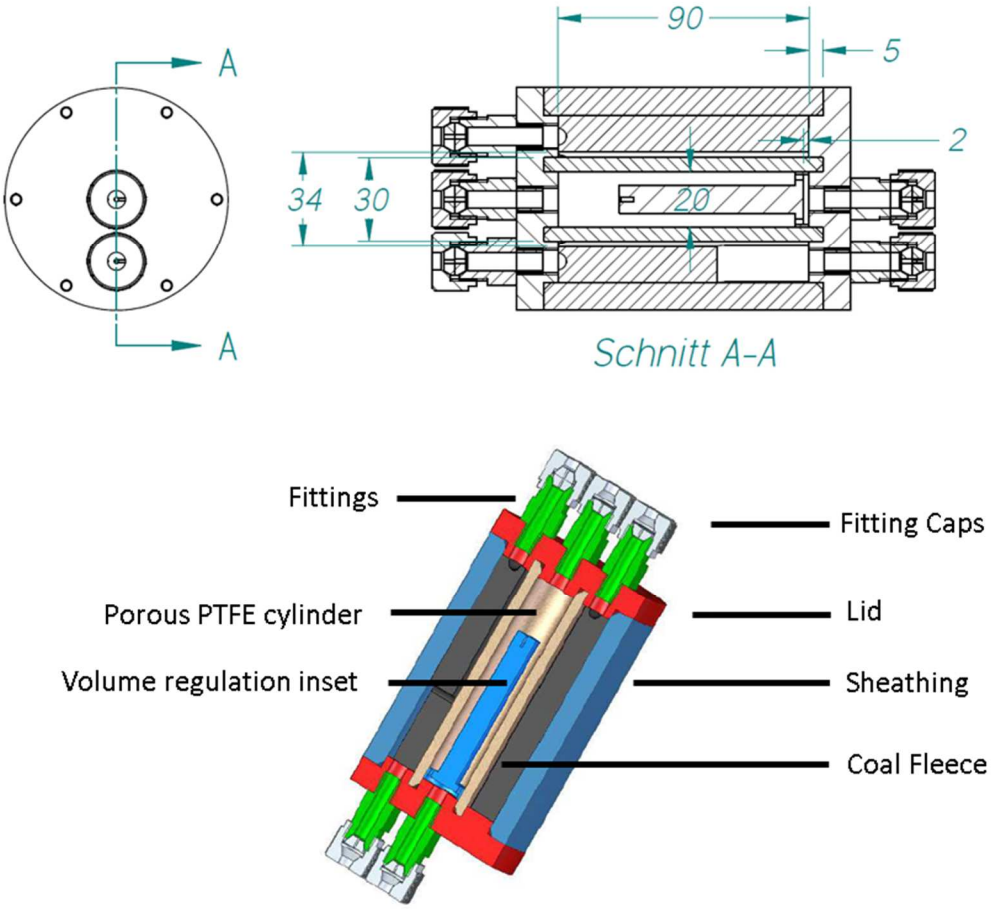

Figure 61: Construction schematic of the electrochemical flow cell. Sheathing and volume regulation inset are blue, coal fleece is black, porous PTFE cylinder is bronze, bottom and top lid are red, fittings are green, and fitting caps are grey. All dimensions are given in mm.

The system was again characterized using **12**. It was tested separately for the acquisition of the EPR spectrum with stopped flow and while flowing.

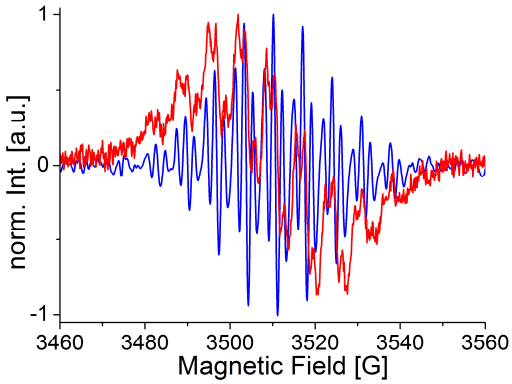

Figure 62: X-band *cw*-EPR spectra of Wurster`s blue acquired with a stopped flow (blue) and a steady flow (red)

As can be seen from the acquired spectra (Figure 62), a well resolved spectrum that matches the previously published spectra of Wurster`s blue[103b] was obtained. With a steady-flow through the cell, a broadening of the spectrum was observed. It should be noted though that for both cases, a better result was achieved than with the setup described in 3.2.1.

3. 3 Investigation of radical interaction on **13** and **14**

Organic radical cations are important reactive intermediates that receive a lot of attention by chemists. They have been used to induce single electron oxidations that start off a large number of C-C or C-X bond forming reactions[104], and they have been used as building blocks for magnetic[105] or conducting materials[106]. With respect to electron conduction, planar organic radical ions have been a major point of investigation[107]. For example, it has been shown that π-electrons can undergo intermolecular electron transfer reactions in stacks of planar radical cations[108]. Such π-electron transfer reactions play also an important role in biology e.g. in the case of stacked porphyrins[109]. In order to understand the factors that influence these electron transfer reactions, kinetic studies are necessary, which may then be interpreted within the framework of the Marcus theory. An interesting field within the framework of this theory is the influence of molecular structure on the electron transfer rate[62a, 110].

Here, the influence of steric demand on the electron self-exchange rate is studied using the two organic radical cations bis(2-pyridylmethyl)azine $\mathbf{13}^{+\cdot}$ and bis(2-pyridylmethyl-5-tert-butyl)azine $\mathbf{14}^{+\cdot}$, where the tert-butyl group at position 4 in $\mathbf{14}^{+\cdot}$ induces a considerable larger steric demand than the hydrogen-atom at the same position in $\mathbf{13}^{+\cdot}$. This couple of molecules is well suited for an investigation of the effect of steric demand on the electron self-exchange rate because they differ structurally only by the t-butyl group/H-atom at position 4 and are both highly persistent organic radicals.

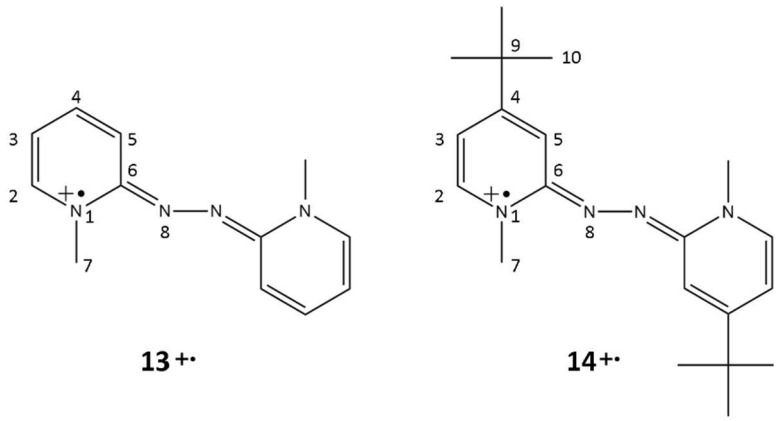

Figure 63: Radical cations of bis(2-pyridylmethyl)amine **13** and bis(2-pyridylmethyl-5-tert-butyl)amine **14**.

Previous studies could show that the electron self-exchange rate in organic radical salts is dependent on the steric demand of the organic systems and may decrease by several orders of magnitude when bulky substituents are introduced. It is usually in the range from 10^2 $L \cdot mol^{-1} \cdot s^{-1}$ to 10^9 $L \cdot mol^{-1} \cdot s^{-1}$ for organic radicals, although it is greatly dependent on the actual

structure and the electron donor properties of the radical in question[111]. However, it was also demonstrated that electron self-exchange is even for very bulky complexes usually faster than processes that require the formation of new bonds such as proton self-exchange[112].

The general mechanism of electron self-exchange reactions at the example of $\mathbf{13}^{+\cdot}$ is shown in Figure *64*. k_d is the rate of diffusion that brings the two reactants in close proximity to each other, k_{ex} is the reaction rate of the actual electron transfer, and k_{-d} is the rate of diffusion with which the reactants separate. From this, a reaction kinetic can be calculated[70b] yielding $k_{ET} = K_A \cdot k_{ex}$, where $K_A = k_d/k_{-d}$ and k_{ET} is the overall rate of the electron self-exchange. The rate for the actual electron transfer k_{ex} is, according to Marcus theory, a function of the reorganization parameter and the coupling matrix element.[61]

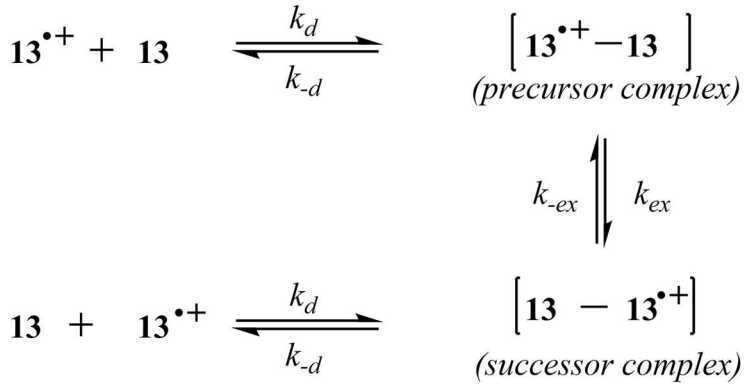

Figure 64: Mechanism of electron self-exchange as given by Marcus Theory for **13**.

Since electron self-exchange is a process where the product and the educt are indistinguishable and also does not involve a change in energy that could be detected as heat or emission of radiation, it cannot be observed by many analytical methods. Experiments monitoring the line broadening in cw-EPR spectra have been successfully used to determine electron self-exchange rates[69, 70b]. Here, compounds $\mathbf{13}^{+\cdot}$ and $\mathbf{14}^{+\cdot}$ are characterized by X-band cw-EPR and their electron self-exchange rates are experimentally determined.

3.3.1 EPR characterization of **13**$^{+\cdot}$ and **14**$^{+\cdot}$

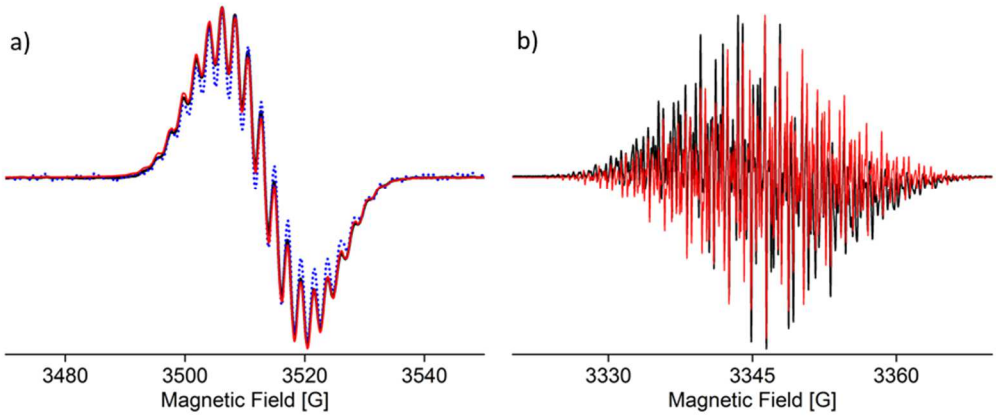

Figure 65: X-band cw-EPR of the radical cations a) **13**$^{+\cdot}$ and b) **14**$^{+\cdot}$ in degassed acetonitrile (chemically generated black, electrochemically generated blue, simulation red).

The X-Band *cw*-EPR spectra of **13**$^{+\cdot}$ and **14**$^{+\cdot}$ are shown in Figure 65. Both radical cations yielded spectra with resolved hyperfine coupling lines but with significantly different linewidths, the one for **13**$^{+\cdot}$ (1.334 G) being considerably larger than for **14**$^{+\cdot}$ (0.147 G). Simulating the spectra yielded the hyperfine coupling constants given in Table *10*, where the atom numbering follows the one in Figure *63*, and a *g*-value of 2.0039 for both. The *g*-value is in accordance with those found for other azo-compounds.[113] The hyperfine coupling constants are typical for heteroaromatic π-systems.[113]

Table 10: Hyperfine coupling constants (HFC) of **1**$^{+\cdot}$ and **2**$^{+\cdot}$ as obtained from DFT and EPR.

HFC [G]	**1**$^{+\cdot}$ (DFT)	**1**$^{+\cdot}$ (EPR)	**2**$^{+\cdot}$ (DFT)	**2**$^{+\cdot}$ (EPR)
N1	2.9	4.2	3.0	3.9
N2	2.1	2.2	1.8	2.3
H5	-3.4	2.9	-3.2	4.4
H3	-3.0	2.4	-3.0	2.9
H7	2.0	1.7	1.7	1.6
H2	0.9	-	0.8	-
H4	0.2	-	-	-
H10	-	-	0.1	-

The larger linewidth for **13**$^{+\cdot}$ is attributed to the unresolved hyperfine coupling constant to H4 (Table 10). To assure that chemical and electrochemical generation of the radical cations did cause the same species, and to exclude counter ion influences on the electronic structure, a *cw*-EPR spectrum of **13**$^{+\cdot}$ that was generated using electrochemical setup 2 was measured and superimposed with the spectrum of chemically generated **13**$^{+\cdot}$ (Figure 65a). The spectra

match each other nicely assuring that under both conditions radical cation **13**$^{+\cdot}$ is formed and that the electronic structure is unaffected by the counter ion.

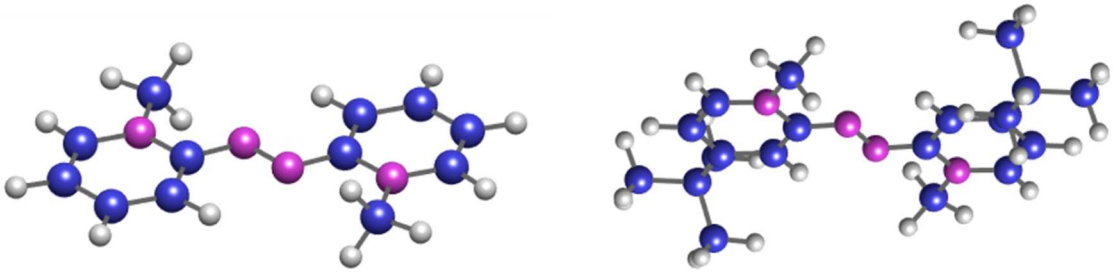

13$^{+\cdot}$ **14**$^{+\cdot}$

Figure 66: Geometry optimized structures of **13**$^{+\cdot}$ and **14**$^{+\cdot}$ as obtained by DFT calculations

Both molecules had been shown to be planar in an x-ray crystal structure (unpublished work by J. Beck et al.). In order to exclude that the planarity of both radical cations found in the x-ray structure is due to crystal packing, DFT based geometry optimizations were performed on both open-shell systems. In each case planar structures are found (dihedral angles of 0°, Figure 66). In addition, the hyperfine coupling constants of **13**$^{+\cdot}$ and **14**$^{+\cdot}$ were calculated based on the geometry optimized structures and where found to fit well to the experimentally obtained ones (Table *10*). This indicates that the radical cations are planar also in solution.

Table 11: Concentration of the neutral compounds and the EPR linewidths for the concentration series of **13**$^{+\cdot}$ and **14**$^{+\cdot}$.

13$^{+\cdot}$		**14**$^{+\cdot}$	
conc. of 1 [mM]	**linewidth [G]**	**conc. of 2 [mM]**	**linewidth [G]**
0	1.334	0	0.147
0.162	1.403	0.157	0.149
0.486	1.407	0.314	0.161
0.810	1.478	0.471	0.165
0.972	1.494	0.628	0.171
1.458	1.559	0.785	0.183
----	----	1.099	0.194

In order to obtain the electron self-exchange rates, the line broadening of the radical cation spectra is measured as a function of the concentration of the neutral, non-radical compound. For the concentrations and resulting linewidths, see Table 11. For these samples, chemically generated radicals were used as opposed to electrochemically generated ones, because it was easier to achieve a known and equal radical concentration for all samples that way. For the details of the sample preparation and the EPR measurements, see appendix A.II. Increasing

the concentration of **13** or **14** leads to a line broadening of the spectra of the corresponding radical cations, because the increasing electron self-exchange rate decreases the lifetime of the spin states[70a]. The obtained linewidths of the radicals are plotted against the concentration of the neutral compound in Figure 67. From these plots, an observed exchange rate constant k_{obs} can be calculated using (eq. 3.1).[70a]

$$\Delta B_{pp} = \frac{(1-p_i)k_{obs}}{\pi \cdot \sqrt{3}\gamma_e}[A] + \Delta B_{pp}^0 \qquad (3.1)$$

Here, ΔB_{pp} is the peak-to-peak linewidth of the self-exchange broadened EPR signal, γ_e is the gyromagnetic ratio of the free electron, p_i is a statistical population factor of the EPR line i that considers non-reactive collisions of equal spin states, because in this case, the exchanging orbitals correspond to equal quantum numbers, and an electron transfer between molecules with the same total nuclear spin number does not affect the EPR linewidths.[69] In case of the multiline spectra shown here, $p_i \ll 1$ can be assumed. ΔB_{pp}^0 is the initial linewidth without electron exchange and [A] is the concentration of the non-radical compound. To obtain the actual electron self-exchange rate constant k_{ET}, the observed self-exchange k_{obs} has to be corrected for diffusion.

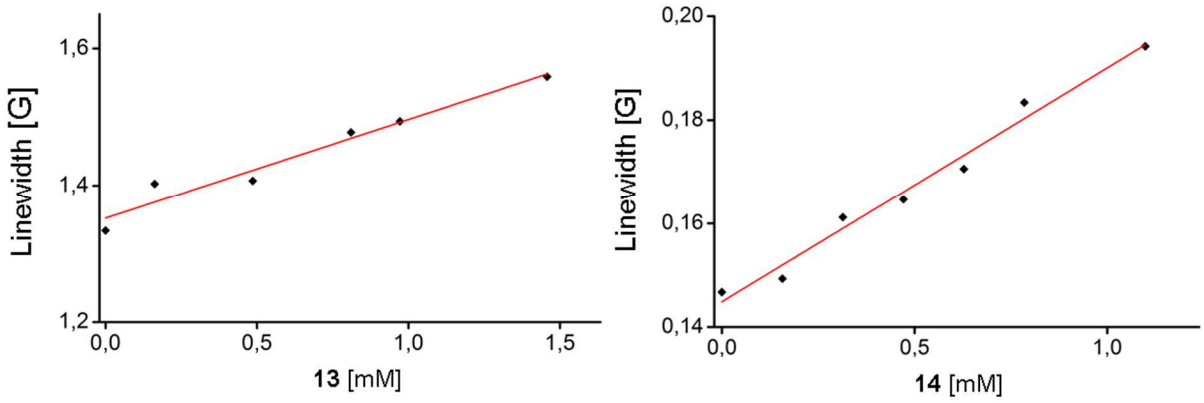

Figure 67: Plots of the EPR linewidths of $\mathbf{1}^{+\cdot}$ and $\mathbf{2}^{+\cdot}$ against the concentration of **1** and **2**, respectively.

Assuming steady state conditions for precursor and successor complex and a non-zero rate constant of electron back transfer, the resulting differential equations can be solved to give the following expression (eq. 3.2).[70a]

$$\frac{1}{k_{ET}} = \frac{1}{k_{obs}} - \frac{2}{k_d} \qquad (3.2)$$

Under the assumption that the radical and the neutral compounds have identical radii, the diffusion rate constant can be calculated using the simplified Smoluchowski equation (eq. 3.3).[114]. It can also be demonstrated that under the assumption of identical radii of the neutral

and the radical species, the diffusion rate is independent of the radii of the reactants, and therefore the same diffusion rate k_d is assumed here for **13**$^{+\cdot}$ and **14**$^{+\cdot}$,

$$k_d = \frac{8RT}{3\eta} \tag{3.3}$$

where R is the ideal gas constant, T the temperature and η the dynamic viscosity of the solvent. Here, η was taken to be 0.316 mPa·s[115]. From this, a diffusion rate constant of k_d= $2.1 \cdot 10^{10}$ L·mol^{-1}·s^{-1} is obtained. For compound **13**$^{+\cdot}$, an observable rate constant $k_{obs,1}$= $1.4 \cdot 10^{10} \pm 0.17 \cdot 10^{10}$ L·mol^{-1}·s^{-1} is obtained. The error of the rate constants is calculated via Gaussian error propagation from eq. 1. The observed rate constant $k_{obs,1}$is of the same order of magnitude as the diffusion rate constant k_d, therefore it is concluded that the electron self-exchange for **13**$^{+\cdot}$ is a very fast process that is diffusion controlled. Using eq. 3.1-3.3, the electron self-exchange rate constant for **14**$^{+\cdot}$ was calculated to give $k_{obs,2} = 4.4 \cdot 10^7 \pm 0.3 \cdot 10^7$ L·mol^{-1}·s^{-1}, which approximately equals $k_{ET,2}$ since $k_d \gg k_{ET,2}$. Thus, $k_{ET,2}$ is three orders of magnitude slower than the observed rate for **13**$^{+\cdot}$, and since it was determined that the rate limiting step for the electron self-exchange of **13**$^{+\cdot}$ is diffusion, the actual difference in the rate of the electron self-exchange may be even higher. Yet, both self-exchange rates are high as compared to other systems reported in the literature. For planar, non-heterocyclic organic radicals of alkyl-substituted multicyclic molecules, e.g. substituted hydrochinone ethers, electron transfer rates in charge-transfer processes with nitrosonium acceptors were reported in the range of 10^3 L·mol^{-1}·s^{-1} to 10^5 L·mol^{-1}·s^{-1}. For monocyclic molecules such as benzene and xylol derived radicals much lower electron transfer rates in the order of 10^{-10} L·mol^{-1}·s^{-1} and less have been reported.[116] For non-planar N-heterocyclic organic radicals, electron self-exchange rates between 10^3 L·mol^{-1}·s^{-1} and 10^5 L·mol^{-1}·s^{-1} have been observed.[110] In contrast very high rates of electron self-exchange were found for molecules with good electron donor or electron acceptor properties and low steric demand such as 2,3-dichlor-5,6-dicyano-1,4-benzochinon (DDQ) or tetracyanoethylene (TCNE), for which electron self-exchange rates in the order of 10^9 L·mol^{-1}·s^{-1} are given in literature.[62a, 117] For biological processes, e.g. the electron self-exchange in human cytochrome C, usual electron self-exchange rates are in the order of magnitude of 10^3 L·mol^{-1}·s^{-1} to 10^4 L·mol^{-1}·s^{-1}.[118] However, it was also found that in cases of a favorable preexisting alignment of the spin centers, faster rates can be observed. An example would be the electron-self-exchange in *pseudomonas aeruginosa azurin* dimers, which show an electron self-exchange rate of 10^6 L·mol^{-1}·s^{-1}.[62b] In addition, a drop by three orders of magnitude in the self-exchange rate is found here for a H/*t*-butyl exchange. This difference in the electron self-exchange rates is also high when compared to similar studies in

the literature[62a]. While similar molecules with different steric demand were found to differ in their electron self-exchange rates, three or more orders of magnitude differences are unusual for organic radicals and occur only in rare cases, e.g. when methyl groups are substituted with large cage-like structures.[110, 116] A plausible rational for the fast rates and the large differences upon H/*t*-butyl exchange may be the formation of stacked π-complexes for **13**/**13**$^{+\cdot}$ whereas the *t*-butyl group either inhibits the formation of such a complex for **14**/**14**$^{+\cdot}$ completely or at least strongly reduces the π-coupling within it. If **13**/**13**$^{+\cdot}$ forms a strongly coupled π-stacked complex, the transfer of an electron within it should be particularly fast.[62a, 119]

In summary, two radical cations were characterized by means of cw-EPR and their electron self-exchange rate constants determined. The found differences in the electron transfer rates are greater than expectations based on literature results for other organic radicals.[62a, 110] This difference can be rationalized as a result of the formation of strongly coupled π-complexes in the case of **13**/**13**$^{+\cdot}$. In addition, the successful use of electrochemical setup 2 was demonstrated.

3.4 Evidence for a radical intermediate in copper catalyzed THIQ coupling reactions

A principal and often rather challenging problem of organic synthesis is the formation of C-C bonds. A powerful tool in the arsenal of organic chemistry to this end is the activation of C-H bonds, which has received considerable attention in recent years.[120] However, many of these catalytic systems require harsh reaction conditions such as high temperatures and pressures

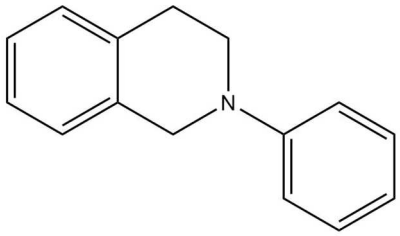

Figure 68: Chemical structure of 2-Phenyltetraisoquinoline(**15**)

as well as acidic or highly oxidizing environments,[121] which in turn have been reported to lead to reduced regioselectivity. A type of functionalization that is of special interest to this endeavors is the selective functionalization of sp^3 C-H bonds adjacent to nitrogen atoms. In this kind of compounds, oxidative activation leads to the formation of iminium ion intermediates, which then can react with a large variety of nucleophiles. One class of such systems that were used for the study of such reactions are tetrahydroisoquinolines (THIQ, **15**), where the activation of the N-benzylic position can be utilized for C1 functionalization. To achieve this, a large variety of conditions have been employed, either using metal catalysis with among others copper[122], platinum[123], iron[124], vanadium[125], ruthenium[126] and rhodium[127], or metal free approaches with hypervalent iodine[128] or DDQ[129]. Following this line of research, a catalytic system using copper and ambient oxygen was developed in the group of Dirk Menche at the University of Bonn.[130] The mechanism of this kind of reaction had been subject to scientific debate, where there were two main questions that needed to be answered. First, it was found that this reaction proceeds with significantly higher yields with $CuCl_2$ than with any other copper(II) salt as well as salts of other metals such as vanadium or ruthenium. This raised the question whether $CuCl_2$ simply "by accident" has the right oxidation potential for the reaction to occur or if a coordination of the THIQ by a copper ion is required. A second major point of debate that applied also to other copper-catalytic systems to functionalize THIQ was whether the reaction proceeded via a purely ionic mechanism or via radical intermediates. For both cases, the group of M. Klussmann proposed potential catalytic cycles[131], which were based on the analysis of the reaction rate at various conditions as well as isolatable intermediates and byproducts. Further computational studies suggested a

radical intermediate of some sort[132], although no definite statement about the structure of the radical intermediate was put forward. An interesting point that was raised for example by Li et al.[133] was if a hypothetical radical would be centered on the benzylic carbon or on the nitrogen, although they ultimately interpreted their results in favor of a ionic reaction mechanism based on the fact that they still could perform the reaction in the presence of a radical scavenger.

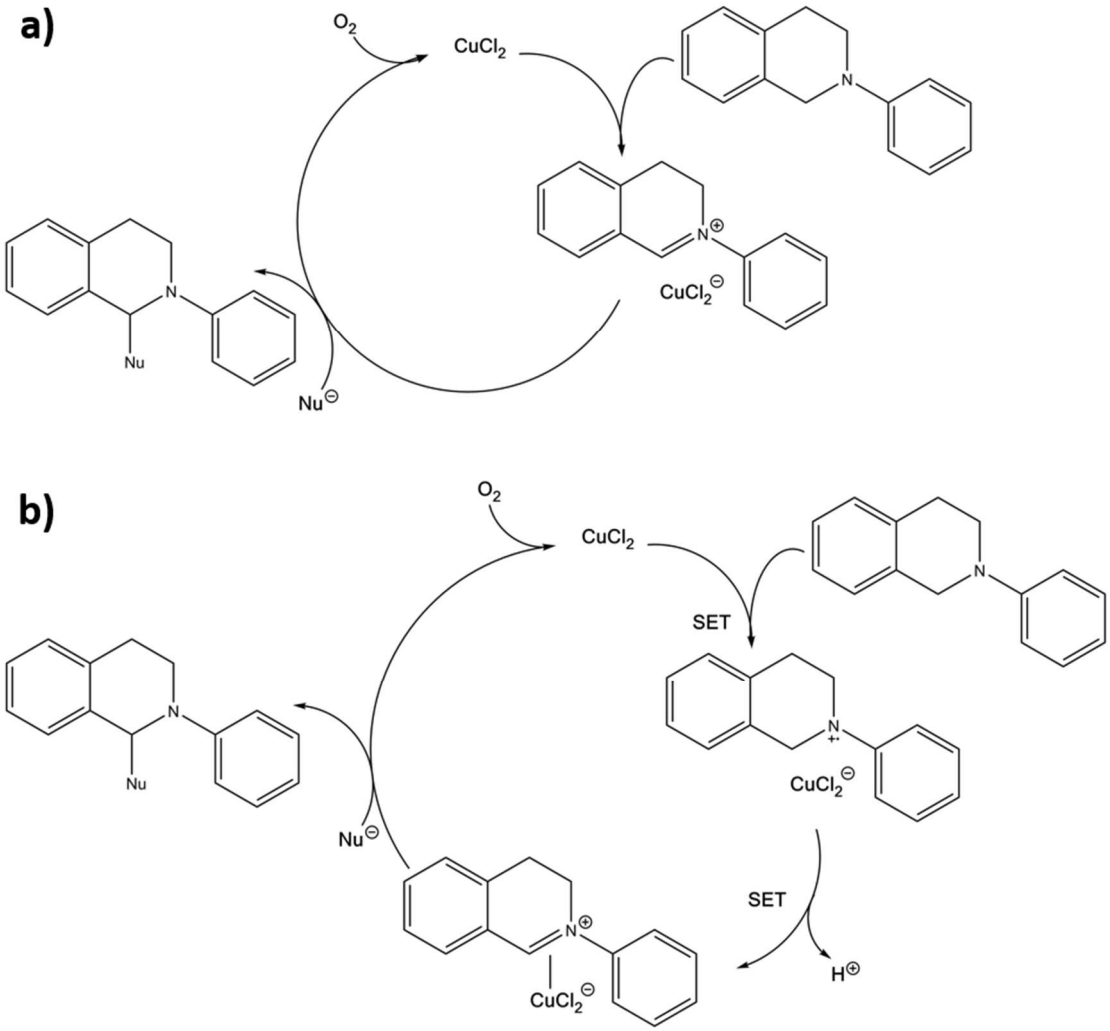

Figure 69: Mechanistic proposals for the copper catalyzed oxidative coupling of **15** under the assumption of a non-radical mechanism (a) and under the assumption of a radical mechanism (b). [125, 131]

Neither of the aforementioned studies employed a methodology that allowed for the direct detection of a radical and had to rely on secondary evidence provided by the post reaction analysis of the reaction mixture or on theoretical calculations. Therefore, an attempt was made to detect the radical intermediate shown in Figure 69b by X-band *cw*-EPR. To assure that no radical was present before a reaction occurred, three samples were prepared: Firstly, a sample of dry acetonitrile, the solvent that was found by the group of D. Menche to give the highest

yield of coupling product, secondly, a solution of THIQ in dry acetonitrile, and thirdly, a solution of $CuCl_2 \cdot H_2O$ in dry acetonitrile. The original coupling procedure calls for anhydrous copper(II) chloride, however, in the absence of THIQ or other organic compounds it can bind to, anhydrous copper(II) chloride is insoluble in dry acetonitrile. As expected, neither the used acetonitrile nor the THIQ solution showed any signal in the EPR spectrum. Cu(II), on the other hand, is a d^9 system and as such EPR active, and detectable at room temperature if present in sufficiently high concentrations. The spectrum recorded for the copper(II)chloride is shown in Figure *70*. The shape of the spectrum is similar to the shape obtained for other copper(II)-nitrogen complexes known from the literature.[134]

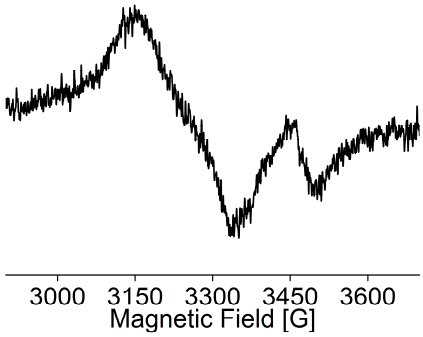

Figure 70: X-band cw-EPR spectrum of $Cu(II) \cdot H_2O$ in acetonitrile at room temperature.

To detect the proposed radical intermediate a reaction mixture as suggested by Menche et al. was made, where a concentration of 1 M THIQ was used together with 0.1 M of $CuCl_2$ in dry acetonitrile, but no nucleophile to intercept the radical or to otherwise interact with whatever intermediate might be formed in the reaction.

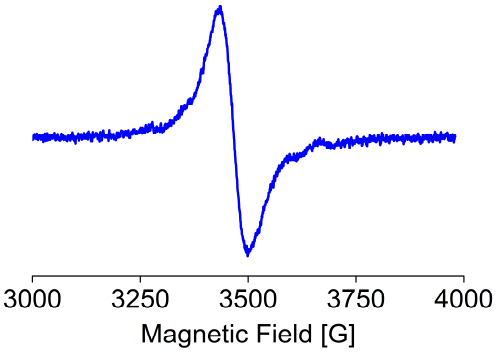

Figure 71: X-band cw-EPR spectrum of the reaction mixture for the copper(II) catalyzed oxidative coupling of THIQ.

As can be seen in Figure 71, no copper signal was evident in the spectrum recorded for the previously described reaction mixture, but a radical with a g-value of 2.014 and a peak-to-peak linewidth of 66 G was detected. From that, a number of conclusions can immediately be drawn: i) no copper(II) could be detected, so it must have formed an EPR silent species. ii) A different radical was detected, therefore, a radical was formed in the reaction cycle. This excludes non-radical mechanisms like the one depicted in Figure 69a. Unfortunately, the radical signal is only badly resolved, therefore no definite conclusions about the structure of the found radical can be drawn, but the data is still sufficient to allow some informed deductions about the structure of the found radical intermediate. The linewidth is unusually broad for an organic radical. This may indicate that the radical is coordinated by the copper, as is suggested in Figure 69b. Regarding the question if the radical intermediate is nitrogen or carbon centered, the g-value gives some indication towards the former, as a g-value of 2.014 is, in any case, rather large for an organic radical, and nitrogen centered radicals in general show larger g-values than carbon-centered radicals do.[113]

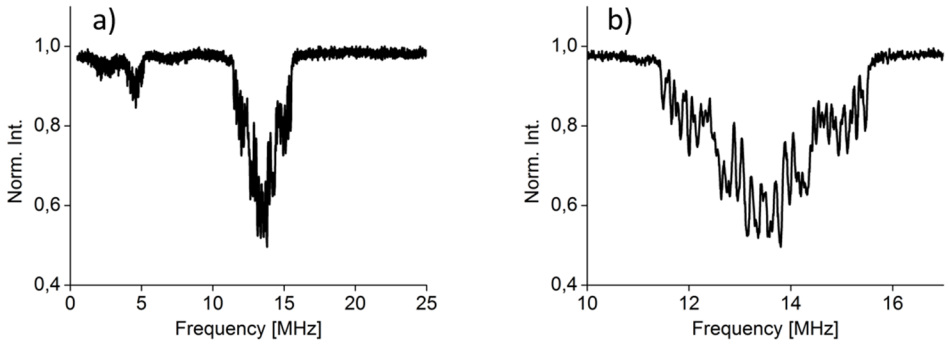

Figure 72: Q-band Mims-ENDOR of the radical in the THIQ coupling reaction mixture (a) and a magnification of the 10 to 17 MHz region of the spectrum (b)

In order to shine some light on the structure of the detected radical, more sophisticated pulsed experiments were conducted to determine the hyperfine coupling constants. A Mims-ENDOR was recorded at X-band and at Q-Band, as well as an X-band HYSCORE. Due to bad resolution(X-band), and strong polarization grating (Q-band), it was not possible to unambiguously assign hyperfine coupling constants. However, the Q-band ENDOR signals center around 13.5 MHz and 4.1 MHz. The calculated Larmor frequencies at the applied magnetic field of 12124 G for likely nuclei in the sample are 3.7 MHz (^{14}N), 13.0 MHz (^{13}C) and 13.7 MHz (^{63}Cu) and 51.6 MHz (^{1}H). These values are no exact match for the obtained data, but allowing for some deviations due to the high noise level of the acquired data, this data is indicative for the existence of spin density on ^{14}N and ^{13}C nuclei with possible

contributions of ^{63}Cu nuclei. The question of whether the radical is predominantly centered on the benzylic carbon or the nitrogen atom could not be clarified, but the existence of ^{13}C and ^{14}N hyperfine interactions solidifies the claim of an organic radical intermediate. A likely cause for the bad resolution of the experiments is a low radical concentration, which is to be expected for short-lived intermediates.

3.5 Evidence for a radical intermediate in the MacMillan catalytic cycle

The introduction of stereo information into organic molecules has been a major point of research in organic synthesis for well over 50 years. It continues to be critical in the synthetic reproduction of natural occurring compounds as well as in the development of bioactive compounds, such as antibiotics or virostatic agents. A key point of such reactions is that unless preexisting stereo information is present in the reacting molecules, only racemic mixtures are obtained. To impress stereo information onto previously achiral, enantioselective catalysis has emerged as the tool of choice. While literally thousands of different catalytic systems for a plethora of possible substrates were synthesized over time[135], the number of different principles for catalytic activation remains far less diverse. Known mechanisms include Lewis acid catalysis[136], σ-bond insertion[137], π-bond insertion[138] and hydrogen bond catalysis[139], each of which spawned a variety of subcategories. Since all these categories lead to significant advances in chemistry, the discovery of new concepts of catalysis is a valuable aim of research. Following this train of thought, the concept of iminium ion organocatalysis was introduced by the group of MacMillan[140], where through the formation of an imiunium ion the energy of the lowest unoccupied molecular orbital (LUMO) of an enal or enone is lowered, which facilitates the enantioselective formation of a large variety of C-C and C-N bond forming reactions. At the same time, the concept of enamine organocatalysis was put forward, where enal and enones where activated via enamine formation, which leads to a higher energy of the highest occupied molecular orbital (HOMO).[141] Since it is a known fact that enamines and iminium ions can rapidly interconvert in a two-electron redox process, MacMillan et al. proposed that it should be possible to intercept the reaction at the stage of the one electron oxidation at what is formally an enamine radical intermediate. At this stage, halfway between the concept of HOMO and LUMO activation, the molecule has a so-called singly occupied molecular orbital (SOMO), which should be activated towards a number of enantioselective reaction, which are not possible with the closed shell catalytic systems of enamines and iminium ions.

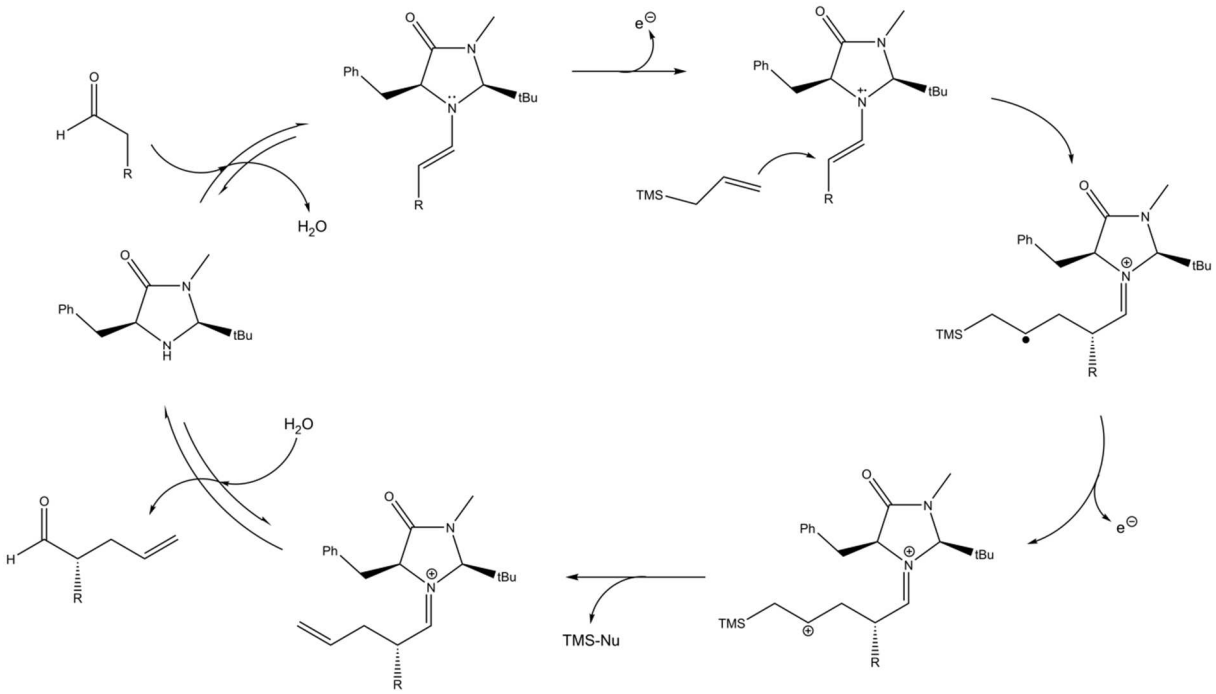

Figure 73: Proposed catalytic cycle of SOMO activated enantioselective α-functionalization of aldehydes[142].

While numerous papers published on that subject in the past decade demonstrate that the principle as such is sound and a viable method to achieve the enantioselective functionalization of carboxyl compounds and their nitrogen analogues, the actual mechanism of these reactions remains obscure. Proposals for the mechanism (for example, see Figure 73) were put forward, often based on the study of reaction kinetics, the products and byproducts of various reactions and theoretical calculations. First experimental evidence for the existence of a radical intermediate via ESI mass spectrometry was published by Beel et al. in 2011.[143]

The research presented here is a part of a larger collaborative effort to expand on these previous results by detecting the radical intermediate postulated in the MacMillan catalytic cycle by other methods, e.g. EPR, and to advance the mechanistic understanding of the reaction. To that end, Dipl. Chem. Christian Mundt of the workgroup of PD Dr. Marianne Engeser synthesized a number of variations of enamines formed from the catalyst (see Figure 74).

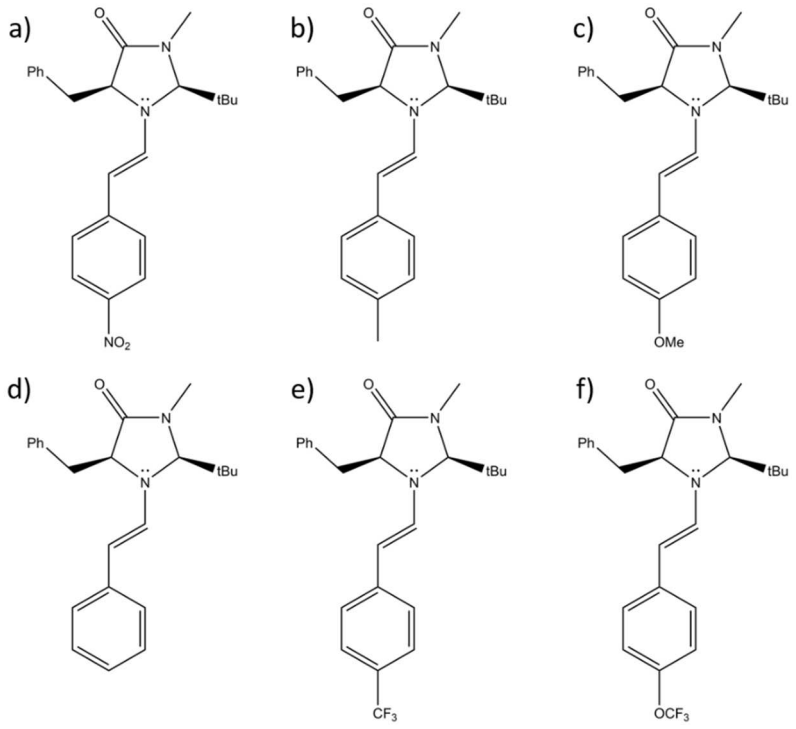

Figure 74: Enamines formed from the MacMillan catalyst and various benzaldehyde derivatives. [**16** (a), **17** (b), **18** (c), **19** (d), **20** (e), **21** (f)].

With these enamines, it is possible to study the radical formation step of the catalytic cycle separately from the other steps of the reaction. In the overall project, the radicals were supposed to be detected by mass spectrometry and EPR, and their electrochemical behavior studied by means of cyclic voltammetry and breakdown curves. The found behavior should then be explained by computational means. Here, only EPR and its aspects will be discussed in detail and the cyclic voltammetry to the extent that it concerns the EPR spectroscopy, as all other research was not performed by the author of this dissertation and will be included in the dissertation of C. Mundt.

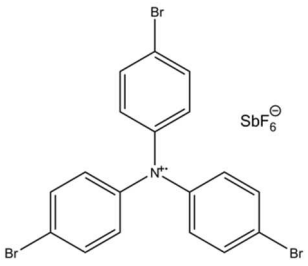

Figure 75:Structure of TPBA (**22**)

EPR detects radicals, so the starting point of the research was to decide on a way to oxidize the enamine to form a radical without over oxidizing it. It was known from previous research by the group of Engeser[144] that the enamine radicals could be generated either through electrolysis or through an excess of a chemical single electron transfer reagent with the right

oxidation potential. The oxidation agent previously used by Engeser was tris(p-bromophenyl)aminiumhexachloroantimonate (**22**). Since the oxidation agent is a nitrogen centered radical, and the goal was to detect an enamine radical that in all likeliness was going to have non-zero spin density on the nitrogen atom, it was assumed that the EPR spectrum of **22** and the postulated radical intermediates would be too similar to distinguish. Therefore, it was decided that the radical for the detection should be generated electrochemically. In preparation of that, the oxidation potential of all enamines were determined via cyclic voltammetry (see Table 12).

Table 12: Oxidation potentials of the enamines against Ag/Ag^+ in 1 : 1 acetonitrile and dichloromethane

Compound	**16**	**17**	**18**	**19**	**20**	**21**
Oxidation Potential [V]	1.10	0.44	0.94	0.82	1.04	0.54

Based on the found oxidation potentials, an attempt was made to detect the enamine radicals using electrochemical setup 1. To that end, solutions of all enamines in a 1:1 mixture of acetonitrile and dichloromethane were prepared, where the enamine concentration was 0.01 M and TBAF was added as a supporting electrolyte to a concentration of 0.1 M. Since the enamines are vulnerable to hydrolysis in the presence of water, dry solvents were used. To ensure that no over oxidation occurs, the potential was gradually increased until a steep increase in current was observed. At that point, the EPR spectrometer was tuned and a spectrum recorded. Unfortunately, no EPR signal was detected. There are several reasons why that might have been the case. First, while the solvent was dry when the solutions were prepared, electrochemical setup 1 does not allow a protection gas atmosphere, therefore moisture will be accumulated from the air. That may have led to the decomposition of the precursor compounds. Secondly, as an intermediate species, the enamine radicals are likely to have a rather short life cycle, which may even be shortened by the presence of oxygen, which is known to react in a number of ways with instable organic molecules. That suggests that while the radical may have been formed during the electrolysis, it never reached a sufficiently high concentration to be detected in an X-band *cw*-EPR experiment. A third point to be considered is that while the potential of the one electron oxidation has been previously determined, the oxidation potential for a second oxidation step was unknown. Also, since through the loss of a second electron a significantly more stable species is formed, it was considered very well possible that the difference in potential of the two oxidation steps was small. It was then decided to switch to electrochemical setup 2. In that setup, the exclusion of water and air could be guaranteed to a much higher degree, because it operates under a

nitrogen overpressure. Since it is a flow through system, the contact time of the individual molecules with the electrode material was reduced, and therefore the probability of over oxidation was lowered. Electrochemical setup 2 controls the current, not the potential, therefore the current was raised very slowly and after each change of current, an EPR spectrum was measured to see if a radical could be detected. In the first attempt to detect the enamine radicals via an electrochemical flow cell setup, in deviation to the setup described in section 3.2.2 a smaller cell with a weaker galvanostatic power unit was used. Both were provided by Prof. Dr. Günther Grampp of the Technical University Graz, Austria. The idea behind the smaller cell was to save substance, since due to the difficult synthesis only very small amounts of the enamines were available. Unfortunately, it turned out that the galvanostatic power unit did not generate currents above 0.1 A, which in the context of the evidently rapid decomposition of the enamine radicals did not generate a sufficiently high initial radical concentration, so that the radical concentration inside the EPR resonator was too low for detection. In order to overcome this issue, the experiment was repeated with a 5 A power unit similar to the one of electrochemical setup 2 and also with a 15 A amplifier. Regrettably, no radical could be detected with the 5 A power unit, and with the additional 15 A amplifier, a black solid formed inside the electrolysis chamber, presumably by way of electro polymerization of the precursor compound. From these results, it seemed clear that with the available equipment, it was impossible to generate the radicals via electrolysis in a

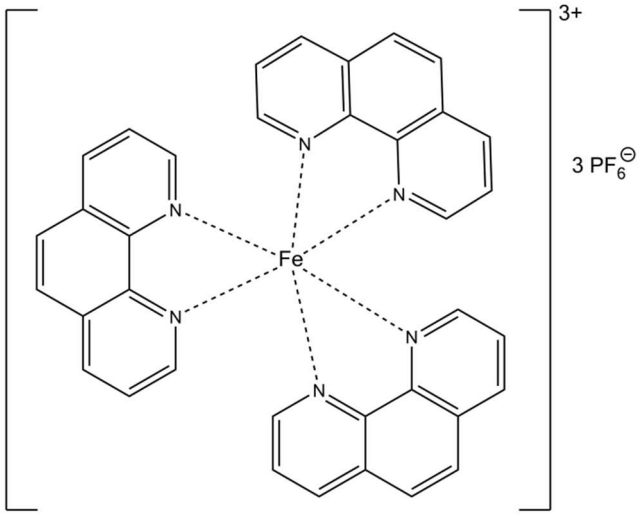

Figure 76: Structure of iron phenanthroline (**23**)

sufficiently high concentration to detect them by EPR.

Because of the failure of the electrochemical approach, alternative ways to generate the enamine radicals by chemical means were considered. The central reason against a chemical

oxidation had been that the oxidant would mask the radical in the EPR spectrum. Therefore, a different oxidant with a similar oxidation potential was needed. As a result of literature research, iron phenanthroline (**23**, see Figure 76) was chosen. Iron compounds usually only show an EPR signal at relatively low temperatures of approx. 50 K or below for low spin iron complexes, and high spin complexes can require temperatures of 10 K or less. Also, iron complexes have distinctly different *g*-values than organic radicals, so that even if an iron signal was detected, it could be distinguished from an enamine radical. In order to establish that indeed no EPR signal could be detected, a room temperature X-Band cw-EPR spectrum of **23** was measured. As expected, no signal was visible. Then, solutions of the enamines with a concentration of 0.01 M in acetonitrile where prepared and a tenfold excess of **23** was added. The samples turned from colorless to slightly yellowish into a distinctive bright red, which is the supposed color of the reduced **23**. All samples were measured immediately after the addition of the oxidizing agent, but no EPR signal could be detected. Since **23** had obviously reacted with the enamine solution, it was reasonably certain that the postulated intermediate of the MacMillan cycle had indeed been formed, but had decomposed too rapidly for detection. This short lifespan was in agreement with the difficulties previously encountered with the electrochemical radical generation approach. Therefore, a means to preserve the radical long enough for detection needed to be found, and the most obvious way was to freeze quench the reaction. To that end, solutions of the enamines in dry acetonitrile were prepared along with a solution of the oxidation agent in the same solvent. Small volumes of the enamine and oxidizing solution were drawn into individual syringes, and combined at the bottom of an X-band EPR tube, which then was immediately plunged into liquid nitrogen. After some practice, it was possible to freeze the sample within two seconds after the combination of the two liquids. Of the thusly-prepared samples and of the iron phenanthroline solution, X-band *cw*-EPR spectra were recorded at 100 K. While the **23** continued to give no EPR signal, EPR signals consistent with organic radicals could be detected for all enamines. For the spectra, see Figure 77.

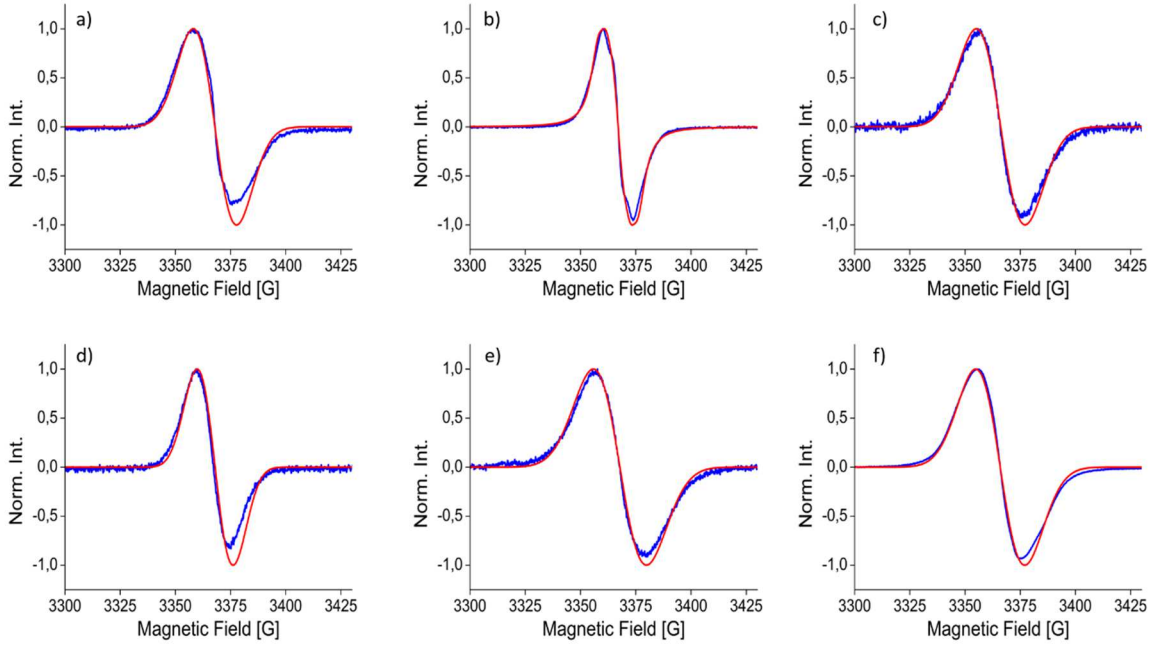

Figure 77: X-band cw-EPR spectra (blue) and Easyspin fits (red) of the enamine radicals formed from **16** (a), **17** (b), **18** (c), **19** (d), **20** (e) and **21** (f).

Table 13: Spectroscopic characteristics of the enamine radicals

Sample	**g-value**	**lwpp [mT]**	**HFC ^{14}N [MHz]**	**HFC ^{1}H [MHz]**	**HFC ^{1}H [MHz]**
16	2.00285	1.67	10.56	15.09	14.77
17	2.00334	0.57	10.34	7.79	15.33
18	2.00313	1.83	11.69	18.56	18.44
19	2.00279	1.11	10.05	18.15	16.75
20	2.00335	2.18	10.88	19.49	5.87
21	2.00317	2.05	10.04	12.75	10.08

From the obtained EPR spectra, the spectroscopic characteristics of the enamine radicals were determined via simulation using the program Easyspin[86]. While the g-values and linewidths can be taken as exact within the error of the experiment, it should definitely be considered that the hyperfine coupling constants are not or not fully resolved in any of the given spectra. As such, no definite claim can be made about the magnitude of the hyperfine coupling constants. The given values are modeled after DFT predictions including the dipolar part of the hyperfine coupling constants that were provided by Dr. Iogann Tolbatov of the workgroup of Prof. Dr. Stefan Grimme.(see appendix C) From the obtained data, a few things can be concluded. The EPR spectra proof unambiguously that in the MacMillan catalytic cycle, a radical intermediate is formed. This strongly supports the previously published results based on mass spectroscopy. The simulation of the spectra is possible with a parameter set that is

consistent with theoretical predictions for the postulated intermediates, which strongly supports the proposed mechanism, although strictly speaking no definite conclusion about the structure can be made other than the statement that the g-value matches expectations for an organic radical. The g-values, on the other hand, are all slightly larger than the g-value of the free electron of 2.0023, which is expected for the radicals of nitrogen compounds.[113]

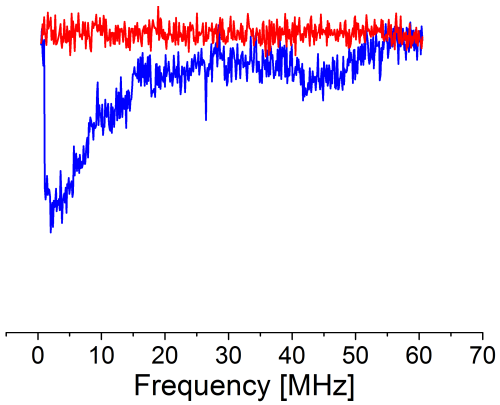

Figure 78: X-band Mims-ENDOR of **20**

In order to gain further evidence towards the actual structure of the radical intermediate, attempts were made to record a Mims-ENDOR, but while hints at signals were present in the experiments which were consistent with the Larmor frequencies of nitrogen and carbon, the overall signal intensity and therefore the SNR was far too low to allow any meaningful interpretation. The most likely reason for that is a too low radical concentration in the samples, which is not that surprising given the difficulties to generate a detectable amount of the enamine radicals.

In summary, it was possible to detect the radical intermediate of the MacMillan catalytic cycle, thereby giving strong evidence for the concept of SOMO activated catalysis, and give secondary evidence to the structure for the radical intermediate, which is consistent with the structure proposed based on product analysis.

3.6 Conclusion

In this part of the thesis, the design of two different setups that combine electrochemistry and EPR spectroscopy is shown. The setups were first tested with a stable test substance, Wurster`s reagent, and then employed at various stages in the investigation of single electron transfer processes. As part of this investigations, the electron self-exchange rates of **13** and **14** were determined and a very fast electron self-exchange was found. Further, the mechanism of the copper(II) catalysed oxidative coupling of **15** was investigated to determine whether the reaction proceeds via a ionic or a radical mechanism. The existence of an organic radical in the reaction mixture could be proved, giving strong evidence for a radical mechanism of the reaction. In an attempt to shine light on the mechanism of the MacMillan catalytic cycle, similar experiments have been conducted on six different enamines that were formed from the MacMillan catalyst and aldehyde substrates. With a combination of electrochemical means and rapid freeze quench, it was possible to show that all investigated enamines form radicals under the conditions of the catalytic reaction, giving strong evidence for a radical mechanism of the MacMillan cycle and the concept of SOMO catalysis.

4 Summary and Outlook

In this work, two major subjects have been addressed. Firstly, the use of trityl radicals in EPR distance measurements has been investigated. Protocols for the use of various distance measurement techniques have been established and compared. Protocols for the labelling of proteins were tested, and their labelling efficiency determined, as well as the performance of several new trityl spin label in label-iron distance measurements relative to an established and commercially available nitroxide label, **1**. Further, the use of a trityl spin label in an in cell measurement has been demonstrated. As was stated in section 2.4, it was demonstrated that DQC and SIFTER experiments are superior in terms of SNR to RIDME and PELDOR for the determination of trityl-trityl distance. PELDOR and most of all RIDME suffer especially at longer distances, where the RIDME experiment could not be successfully performed. For the trityl spin label, labelling procedures have been established for the labelling of *pseudomonas putida* cytochrome CYP101, **6** and **7** performed equally well as the commercially available **1**. **8** and **9** use different binding strategies than the previously mentioned labels, and performed significantly worse in terms of labelling efficiency. All labels were shown to be stable under the conditions and within the time frame of the labelling procedure. The *in vitro* measurement of the label-iron(III) distance on **7**, **8** and **1** showed that the trityl labels perform equally well as **1** in terms of modulation depth if variations in the iron-content of the protein are taken into account. **7** performs better in terms of SNR, while **8** performs equally well as **1**. This difference in performance is due to the relatively poor labelling efficiency of **8**. The successful demonstration of an in cell trityl-iron(III) RIDME measurement shows that trityl labels are indeed usable in an biological environment, and provide accurate distance information under such conditions. All the work presented here will further the use of trityl spin labels for applications in structural biology. Future work will aim at the improvement of the *in cell* distance measurement protocol, to enable distance measurements at biologically relevant conditions. Together with publications by Shevelev et al.[72] that demonstrated trityl distance measurements at physiological relevant temperatures, this work provides yet another step towards overcoming the limitations in terms of the measurement conditions that EPR faces today, were distance measurements are usually conducted in frozen buffer solutions.

Secondly, the development and application of two different combined electrochemical and EPR spectroscopic setups has been shown. As was also stated in section 3.6, the setups were used among other methods in the investigation of the electron self-exchange rate of **13** and **14**. A very fast exchange was found for both compounds, although the respective exchange rates

differ by three orders of magnitude. This is consistent with expectations based on the increased steric demand of **14** relative to **13**. Beyond these investigations, the mechanism of the copper catalysed coupling reactions of **15** was investigated, where an organic radical was found in the reaction mixture. While a characterization of the structure of the radical remained unsuccessful, the formation of a radical in the reaction mixture indicates that the reaction proceeds via a radical mechanism. The investigation therefore supports a radical mechanism, e.g. the one put forward by the group of M. Klussmann[125, 131] and opposes contradicting proposals of purely ionic reaction mechanisms.[122] Lastly, the mechanism of the MacMillan organocatalytic cycle and the concept of SOMO catalysis was investigated. To this end, the radical formation step of the reaction was modelled with enamines formed form the MacMillan catalyst and various aldehyde substrates. The postulated radical intermediate should then be formed either by means of electrochemical oxidation or chemical oxidation. Due to the short lifespan of the radical intermediates, it was not possible to generate a sufficiently high concentration of radicals for detection by electrochemical means. However, through a combination of chemical oxidation and freeze quench techniques, it was possible to detect organic radicals consistent with the postulated intermediate for all enamines. This is the first time the radical intermediate of the MacMillan cycle was directly observed by means of EPR, thereby giving strong evidence for the proposed mechanism and the concept of SOMO catalysis. The shown applications of the two electrochemical setups demonstrate that the setups do work, and can be used to acquire scientific information. While certainly not the only setup worldwide with these capabilities, the assembled gear allows to perform combined electrochemical and EPR experiments at the University of Bonn, which was previously not possible. The shown applications demonstrate that the combination of these two methodologies can be very useful to proof the existence of transient or short-lived radical species, such as the intermediates in the investigated catalytic reactions. Future work will concentrate on applying these setups to new areas of research, e.g. the investigation of phosphorus-organic compounds, and improving the protection gas atmosphere and time resolution of the electrochemical setups as necessary.

Appendix A: Materials and Methods

Appendix. A.I: Materials and Methods of Chapter 2

All pulsed EPR experiments were performed on a Bruker ELEXSYS 580 EPR spectrometer equipped with a SpecJet-II and a PatternJet-II combination. For measurements at cryogenic temperatures, a helium flow cryostat (CF935) and an ITC 502 temperature control system from Oxford Instruments was used. For pulsed X-band measurements, a dielectric ring resonator (MD-5) was used together with a 1kW TWT amplifier (117X) from Applied Systems Engineering. For pulsed Q-band measurements, an ER 5106QT-2 resonator from Bruker was used together with a 150 W amplifier from Applied Systems Engineering. Field-swept spectra were measured with the Hahn-Echo sequence $\pi/2$-τ-π.[28] PELDOR measurements were performed using the four-pulse sequence $\pi/2(\nu_A)$ - τ_1- $\pi(\nu_A)$ - τ_{1+t}- $\pi(\nu_B)$ - τ_{2-t} - $\pi(\nu_A)$ - τ_2 – echo.[8] To avoid detection artifacts, a two-step phase cycle was employed.

Table 14: 2-step phase cycle for PELDOR

$P_1(\pi/2)_A$	$P_2(\pi)_A$	$P_3(\pi)_A$	$P_4(\pi)_B$
+x	+x	+x	+x
-x	-x	-x	+x

RIDME measurements were performed using the five-pulse sequence $\pi/2$- τ_1- π - τ_{1+t}- $\pi/2$- T – $\pi/2$- τ_2 – π - echo.[9] RIDME measurements were performed with a 8-step phase cycle.

Table 15: 8-step phase cycle for RIDME

$P_1(\pi/2)$	$P_2(\pi)$	$P_3(\pi/2)$	$P_4(\pi/2)$	$P_5(\pi)$
+x	+x	+x	+x	+x
+x	+x	-x	-x	+x
+x	+x	+y	+y	+x
+x	+x	-y	-y	+x
-x	+x	+x	+x	+x
-x	+x	-x	-x	+x
-x	+x	+y	+y	+x
-x	+x	-y	-y	+x

SIFTER measurements were performed using the four pulse sequence introduced by Jeschke et al. $\pi/2$- τ_1- π - τ_1- $\pi_y/2$- τ_2 – π - τ_2- echo.[32] The sequence was used together with a 16-step phase cycles to filter out contributions from unwanted coherence pathways.

Table 16: 16-step phase cycle for SIFTER

$P_1(\pi/2)_x$	$P_2(\pi)_x$	$P_3(\pi/2)_y$	$P_4(\pi)_x$
+x	+x	+x	+y
+x	+y	+x	+y
+x	-x	+x	+y
+x	-y	+x	+y
+x	+x	+x	-y
+x	+y	+x	-y
+x	-x	+x	-y
+x	-y	+x	-y
+x	+x	-x	+y
+x	+y	-x	+y
+x	-x	-x	+y
+x	-y	-x	+y
+x	+x	-x	-y
+x	+y	-x	-y
+x	-x	-x	-y
+x	-y	-x	-y

DQC experiments were performed using the six pulse sequence $\pi/2$- τ_1 - π - τ_1- $\pi/2$-τ_2-π - τ_2 - $\pi/2$-$(\tau_m - \tau_p)$ - π - $(\tau_m - \tau_p)$ – echo proposed by Freed et al.[31]. To spearate the double quantum coherence pathway, a 64-step phase cycle was used.

Table 17: 64-step phase cycle for DQC

$P_1(\pi/2)$	$P_2(\pi)$	$P_3(\pi/2)$	$P_4(\pi)$	$P_5(\pi/2)$	$P_6(\pi)$
+x	+x	+x	+x	+x	+x
+y	+y	+y	+x	+x	+x
-x	-x	-x	+x	+x	+x
-y	-y	-y	+x	+x	+x
+x	+x	+x	+y	+x	+x

+y	+y	+y	+y	+x	+x
-x	-x	-x	+y	+x	+x
-y	-y	-y	+y	+x	+x
+x	+x	+x	-x	+x	+x
+y	+y	+y	-x	+x	+x
-x	-x	-x	-x	+x	+x
-y	-y	-y	-x	+x	+x
+x	+x	+x	-y	+x	+x
+y	+y	+y	-y	+x	+x
-x	-x	-x	-y	+x	+x
-y	-y	-y	-y	+x	+x
+x	+x	+x	+x	-x	+x
+y	+y	+y	+x	-x	+x
-x	-x	-x	+x	-x	+x
-y	-y	-y	+x	-x	+x
+x	+x	+x	+y	-x	+x
+y	+y	+y	+y	-x	+x
-x	-x	-x	+y	-x	+x
-y	-y	-y	+y	-x	+x
+x	+x	+x	-x	-x	+x
+y	+y	+y	-x	-x	+x
-x	-x	-x	-x	-x	+x
-y	-y	-y	-x	-x	+x
+x	+x	+x	-y	-x	+x
+y	+y	+y	-y	-x	+x
-x	-x	-x	-y	-x	+x
-y	-y	-y	-y	-x	+x
+x	+x	+x	+x	+y	+x
+y	+y	+y	+x	+y	+x
-x	-x	-x	+x	+y	+x
-y	-y	-y	+x	+y	+x
+x	+x	+x	+y	+y	+x
+y	+y	+y	+y	+y	+x

-x	-x	-x	+y	+y	+x
-y	-y	-y	+y	+y	+x
+x	+x	+x	-x	+y	+x
+y	+y	+y	-x	+y	+x
-x	-x	-x	-x	+y	+x
-y	-y	-y	-x	+y	+x
+x	+x	+x	-y	+y	+x
+y	+y	+y	-y	+y	+x
-x	-x	-x	-y	+y	+x
-y	-y	-y	-y	+y	+x
+x	+x	+x	+x	-y	+x
+y	+y	+y	+x	-y	+x
-x	-x	-x	+x	-y	+x
-y	-y	-y	+x	-y	+x
+x	+x	+x	+y	-y	+x
+y	+y	+y	+y	-y	+x
-x	-x	-x	+y	-y	+x
-y	-y	-y	+y	-y	+x
+x	+x	+x	-x	-y	+x
+y	+y	+y	-x	-y	+x
-x	-x	-x	-x	-y	+x
-y	-y	-y	-x	-y	+x
+x	+x	+x	-y	-y	+x
+y	+y	+y	-y	-y	+x
-x	-x	-x	-y	-y	+x
-y	-y	-y	-y	-y	+x

Unless otherwise stated, the length of $\pi/2$ – pulses was 12 ns, and the length of π – pulses 24 ns. Tau values for field swept spectra were 350 ns, unless stated otherwise. T values for RIDME experiments were 25000 ns for trityl-iron samples, and 30000 ns for nitroxide samples. Trityl and nitroxide samples were measured with a shot repetition time of 3000 μs. For PELDOR experiments, pulse phase and amplitude were set to optimize the refocuded echo. For RIDME experiments, the refocused virtual echo was optimized and detected.

Temperatures, other separations, length of inversion pulses vary between the different measurements and are stated with the individual experiments. Deviations from the values given here are stated with the respective experiments. The distance measurements on the bistrityl model compounds **4** and **5** were performed at 50 K, the measurement pulse lengthes and separations are given in the following tables.

*Table 18: Pulse lengths and separations of the PELDOR experiments on **4** and **5***

Compound	$\boldsymbol{\pi}$-pulse	$\boldsymbol{\pi/2}$-pulse	$\boldsymbol{\tau_1}$	$\boldsymbol{\tau_{1+t}}$+ $\boldsymbol{\tau_{2-t}}$	Frequency offset
4	64 ns	32 ns	350 ns	2000 ns	15 MHz
5	64 ns	32 ns	350 ns	4000 ns	15 MHz

*Table 19: Pulse lengths and separations of the RIDME experiments on **4** and **5***

Compound	$\boldsymbol{\pi}$-pulse	$\boldsymbol{\pi/2}$-pulse	$\boldsymbol{\tau_1}$	$\boldsymbol{\tau_2}$	T
4	24 ns	12 ns	350 ns	2000 ns	100 μs
5	24 ns	12 ns	350 ns	4000 ns	100 μs

*Table 20: Pulse lengths and separations of the SIFTER experiments on **4** and **5***

Compound	$\boldsymbol{\pi}$-pulse	$\boldsymbol{\pi/2}$-pulse	$\boldsymbol{\tau_1}$	$\boldsymbol{\tau_2}$
4	24 ns	12 ns	350 ns	2000 ns
5	24 ns	12 ns	350 ns	4000 ns

*Table 21: Pulse lengths and separations of the DQC experiments on **4** and **5***

Compound	$\boldsymbol{\pi}$-pulse	$\boldsymbol{\pi/2}$-pulse	$\boldsymbol{\tau_1}$	$\boldsymbol{\tau_2}$	$\boldsymbol{\tau_m}$
4	24 ns	12 ns	350 ns	50 ns	2000 ns
5	24 ns	12 ns	350 ns	50 ns	4000 ns

All X-band *cw*-EPR spectra were recorded on a Bruker EMX Micro X-Band EPR spectrometer using a standard 4122-SHQE resonator with a UMC0059 cryostat from Oxford Instruments. Spin counting experiments were performed on a Bruker EMX Nano X-Band benchtop EPR spectrometer. All room temperature spectra of bistrityl model compounds were measured with a modulation amplitude of 1 G and a power of 1.5 mW on 50 μM solutions in methanol (Sigma-Aldrich). The spectra were measured with a time constant of 20.48 ms and a resolution of 20 points per Gauss. Low temperature measurements for *cw*-EPR distance measurements were performed on 50 μM solutions in 2 : 1 dichloromethane and methanol.

The samples were degassed by five cycles of freeze-pump-thaw and flame sealed. The spectra were recorded with a time constant of 82 ms, a modulation amplitude of 0.008 G, a microwave power of 9 μW and a resolution of 250 points per Gauss. All spectra of free spin labels were measured on 100 µM solutions of the respective label in dry DMSO (Sigma-Aldrich) which were then degassed by five cycles freeze-pump-thaw and placed in flamesealed quarz capillaries. For stability measurements of said spin labels, both degassed and not degassed samples in both DMSO (Sigma-Aldrich) and deionised Water were used. Samples of labeled protein were measured in TRIS-buffer (pH = 7.4). Spectra were measured at room temperature and at 80 K. For all room temperature spectra of trityl labels and labeled protein, a microwave power of 9 µW and a modulation amplitude 0.008 G were used together with a time constant of 82 ms and a resolution of 250 points per Gauss. For frozen spectra of spin labels and labeled proteins, a microwave power of 9 mW and a modulation amplitude of 1 G were used with a time constant of 82 ms and aresolution of 10 points per Gauss. Time series of the free labels were recorded on a Bruker EMX nano benchtop *cw*-EPR X-band spectrometer at room temperature. Frozen solution spectra of labeled proteins were carried out on the previously described EMX micro setup at 10 K. For those spectra a microwave power of 0.546 mW and a modulation amplitude of 1 G and a time constant of 20.48 ms were used with a resolution of 20 points per Gauss. X-band *cw*-EPR of labeled protein in *xenopus laevis* oocytes were measured on the described EMX micro setup at 10 K. A microwave power of 0.053 mW and a time constant of 20.48 ms were used together with a modulation amplitude of 1 G. and a resolution of 10 points per Gauss.

Xenopus laevis oocytes were injected with 50.6 nL of a 5 mM solution of CYP101 C58T3 in TRIS buffer using a Drummond Nanoject II microinjector. As described by Azarkh et al. [50], the oocytes were handsorted to assure only healthy and intact oocytes are used. The microinjector was then prepared by first pulling a glass needle form a glass capillary (ø 0.3 mm) using a bunsen burner. The needle was than filled with a light silicone oil, mounted on the microincetor and filled with the protein solution. The oocytes are then placed under a dissection microscope in a buffer solution and carfully penetrated with the glass needle. A defined amount of protein solution (here: 50.6 nL) was injected via the microinjector. The glass needle is then removed carefully and the oocyte visually inspected for leakage. Oocytes that leak either protein or other fluids are sorted out. To ensure that there is no protein solution clinging to the outer surface of the oocytes, they were washed several times with clean buffer. Due to the intense coloring of the trityl, contaminations were easily spotted. The oocytes were then placed in a quartz Q-band EPR tube with buffer solution and shock frozen

with liquid nitrogen. The average inner volume of a *xenopis laevis* oocyte is 1 µL, therefore, with the given concentration of the protein solution and the injected volume, an average in cell protein concentration of 250 µM was calculated.

To determine the SNR of , all timetraces are fixed to the same length (2000 ns for experiments on **4** and **5**, 1500 ns for experiments on protein samples), and normalized to S = 1 at t = 0. The timetraces are corrected for their background, and renormalized. The timetraces are then multiplied with their respective modulation depth, and devided by the average noise. To maintain comparapility for different measurement times, the signal to noise is then devided by the square root of the measurement time in minutes. To account for different iron contents, the SNR of the CYP101 C58 samples is then devided by the relative iron content of the samples, where the iron content of the CYP101 C58R1 sample is taken to be 1.

Appendix. A.II: Materials and Methods of Chapter 3.3

Compounds **13** and **14** are in the neutral form deep red solids and are as their radical trifluormethanesulfonate salts deep purple. EPR-Spectra were recorded on a Bruker EMX Micro X-Band EPR Spectrometer For degassed samples, the solid radical cations were dissolved under argon in dry acetonitrile (Sigma Aldrich). The sample was placed under argon in a quartz capillary, which was then flame sealed. The samples for the determination of the electron exchange rate were made in the same way. All of these samples had a radical concentration of 0.1 mM. For the concentrations of the neutral compound in each sample and the corresponding EPR linewidths, see Table *11* in the main text. All *cw*-EPR spectra of $\mathbf{13}^{+\cdot}$ were measured with a modulation amplitude of 0.2 G, and all spectra of $\mathbf{14}^{+\cdot}$ were measured with a modulation amplitude of 0.01 G. A time constant of 81.92 ms was used together with a conversion time of 82 ms for all cases. For all spectra, a microwave power of 3.112 mW was used. Simulations of the EPR spectra were done with the Matlab script Easyspin[86] using the 'garlic' function and fitted with the 'esfit' function to match the recorded spectra. The linewidths of the concentration depended measurements were obtained by keeping the *g*-value and HFCs obtained for the pure radical compounds and fitting the linewidth with the 'esfit' function of Easyspin (Table *10*, main text). For electrochemical experiments, the radical salt was dissolved in acetonitrile to a concentration of 10^{-4} M and 0.01 M of tetrabutylammoniumhexafluorophosphate were added as a supporting electrolyte. Electrochemical setups were used as described in sections 3.2.1 Potentiostatic electrolysis cell (electrochemical setup 1) and 3.2.2 Electrochemical flow cell (electrochemical setup 2) For

degassed samples for electrochemical purposes, HPLC grade acetonitrile was bubbled with nitrogen for at least 30 minutes. DFT calculations for EPR parameters were done with Orca[145], using the functional PBE0 and the basis set EPRII. For geometry optimization, the functional B3LYP was used with the basis set 6-31+G.

Appendix B: EPR data

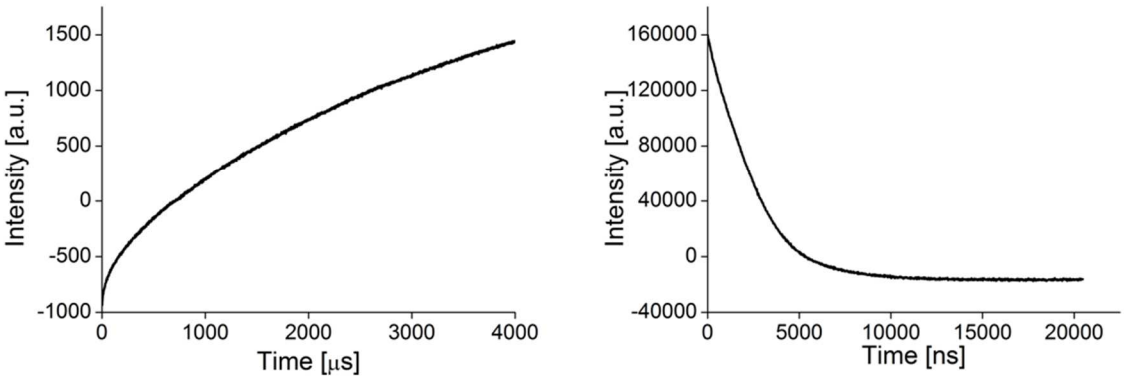

*Figure 79: Inversion recovery (left) and 2-Pulse ESEEM of **5** in DCM at 50 K.*

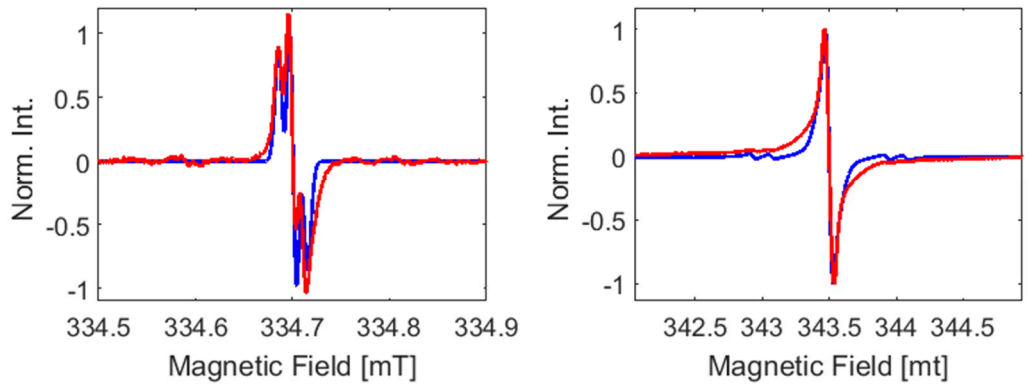

*Figure 80: X-Band cw-EPR spectra of **7** at room temperature (left) and at 80 K (right). Easyspin simulation is overlayed as a blue line.*

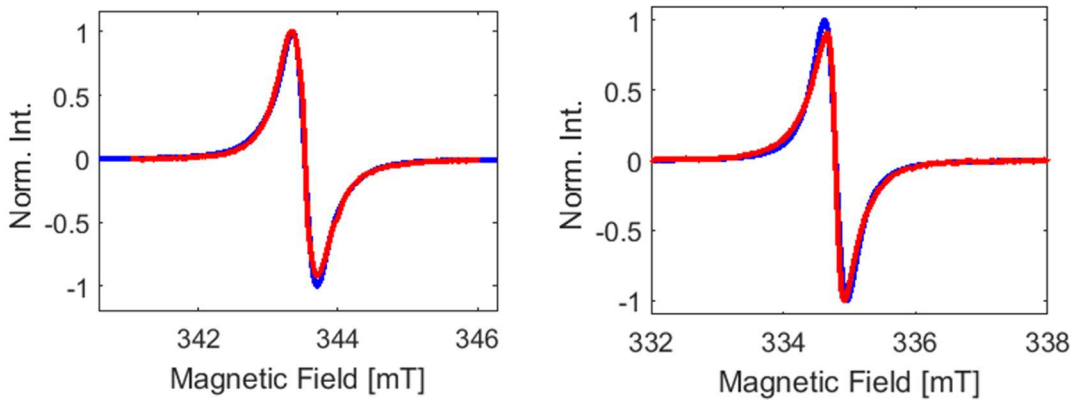

*Figure 81: X-Band cw-EPR spectra of **6** at room temperature (left) and at 80 K (right). Easyspin simulation is overlayed as a blue line.*

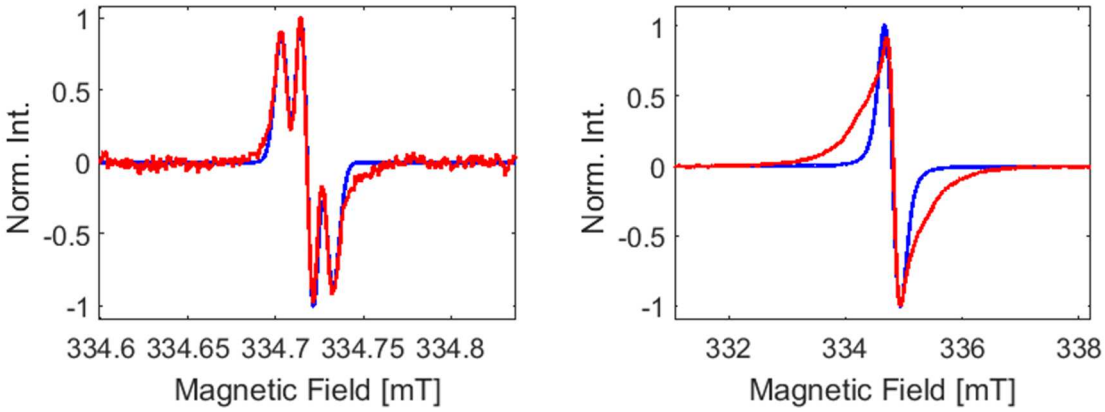

*Figure 82: X-Band cw-EPR spectra of **8** at room temperature (left) and at 80 K (right). Easyspin simulation is overlayed as a blue line.*

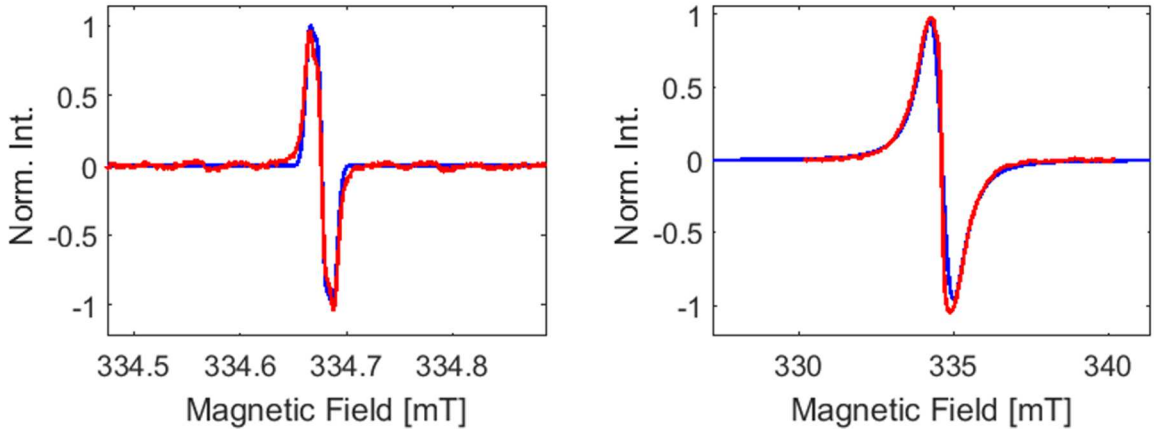

*Figure 83: X-Band cw-EPR spectra of **9** at room temperature (left) and at 80 K (right). Easyspin simulation is overlayed as a blue line.*

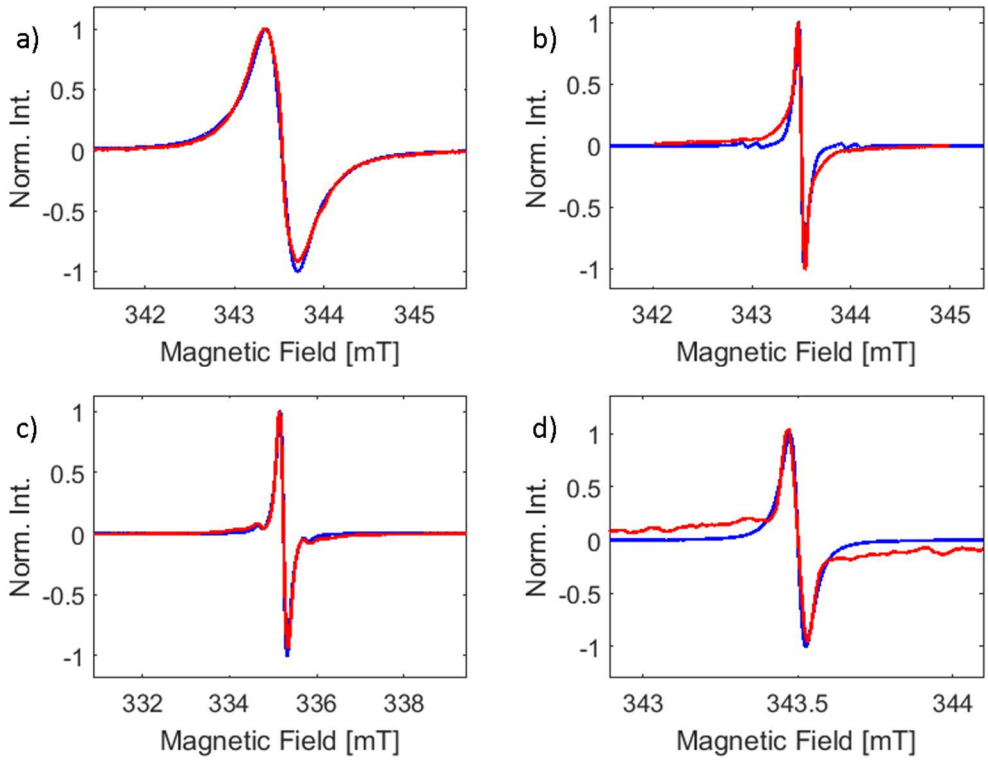

*Figure 84: X-band cw-spectra of a) CYP101 C58 labeled with **6** b) CYP101 C58 labeled with **7** c) CYP101 C58 labeled with **8** d) E. coli FeoB R152 labeled with **9**. Easyspin simulations for all spectra are overlayed as blue lines. In c), ^{13}C satellites were included in the simulation.*

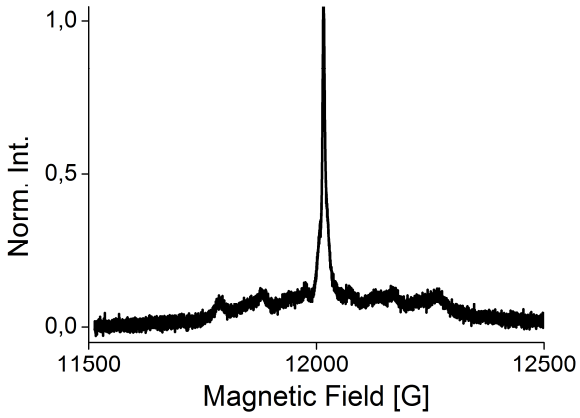

*Figure 85: Q-band field swept spectrum of CYP101 C58 labeled with **8** inside xenopus laevis oocytes*

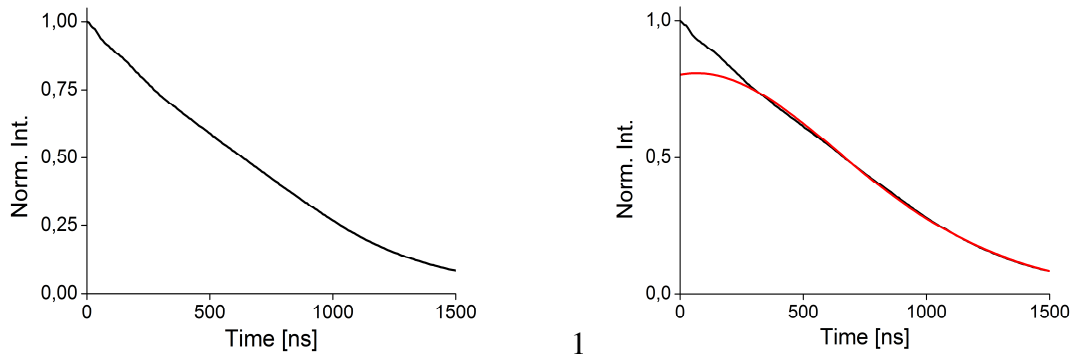

Figure 86: Q-band RIDME Timetrace (black) of CYP101 C58T1 at 25 K prior to background correction and background fit (red).

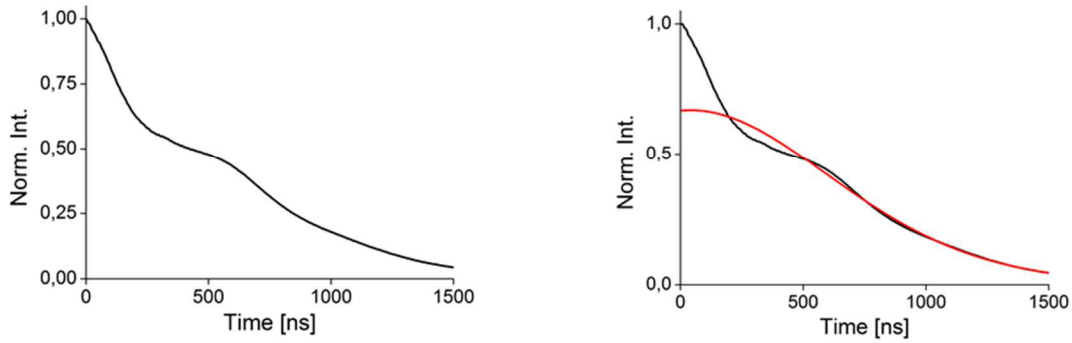

Figure 87: Q-band RIDME timetrace (black) of CYP101 C58R1 at 25 K prior to background correction and background fit (red).

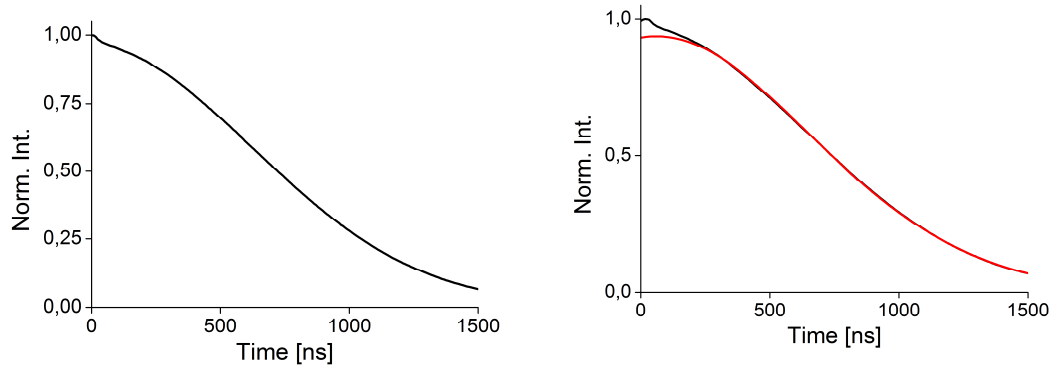

Figure 88: Q-band RIDME Timetrace (black) of CYP101 C58T3 at 25 K prior to background correction and background fit (red).

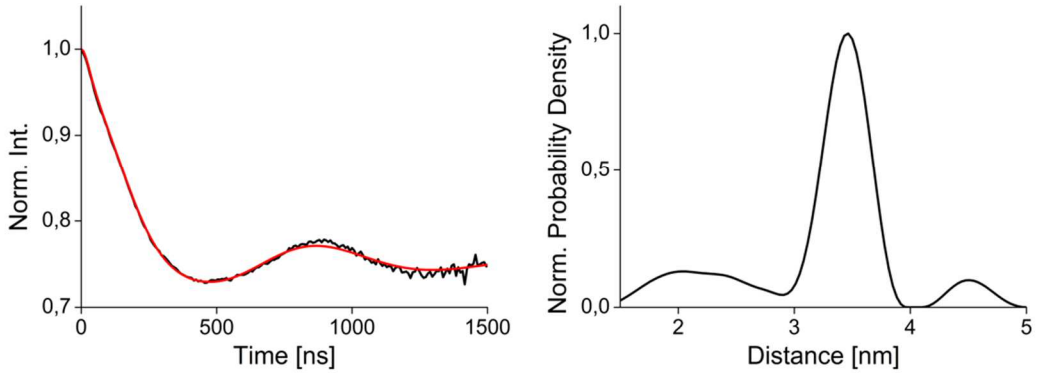

Figure 89: Q-band RIDME Timetrace (black) and DeerAnalysis fit (red) of CYP101 C58T1 at 25 K. The resulting distance distribution is shown on the right. The spectrum was recorded on a new sample independently prepared from the one used for the experiments shown in the main text to demonstrate the reproducibility of the results.

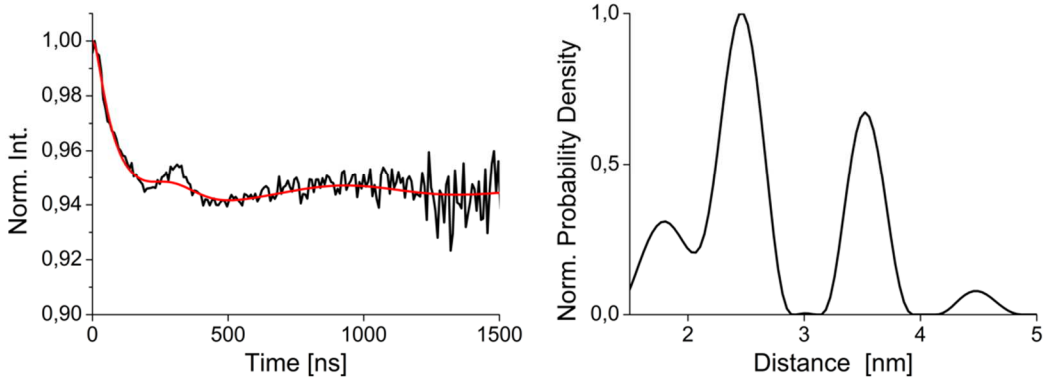

Figure 90:Q -band RIDME Timetrace (black) and DeerAnalysis fit (red) of CYP101 C58T3 at 25 K. The resulting distance distribution is shown on the right. The spectrum was recorded on a new sample independently prepared from the one used for the experiments shown in the main text to demonstrate the reproducibility of the results

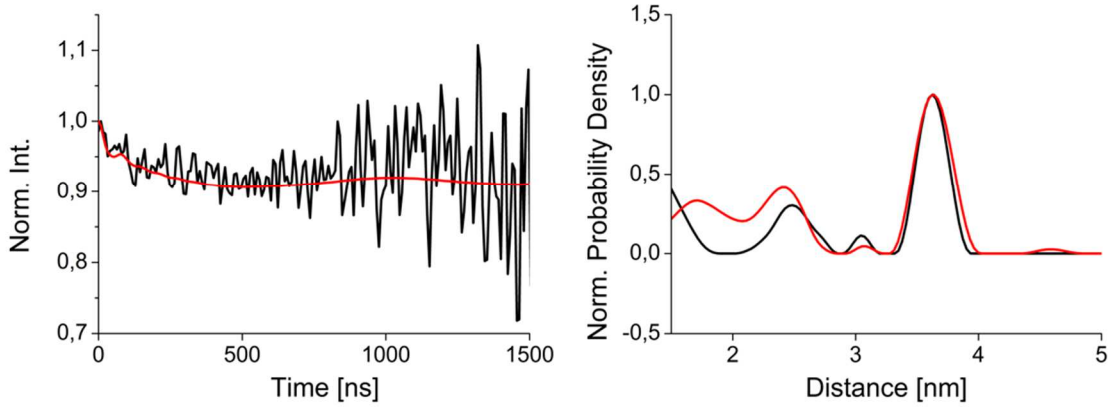

Figure 91: Q-band RIDME Timetrace (black) and DeerAnalysis fit (red) of CYP101 C58T3 at 25 K inside xenopus laevis oocytes. The resulting distance distribution is shown on the right (black) and overlaid with the in cell distribution obtained on a different batch that was used for the experiments shown in the main text.

Appendix C: Theoretical Calculations

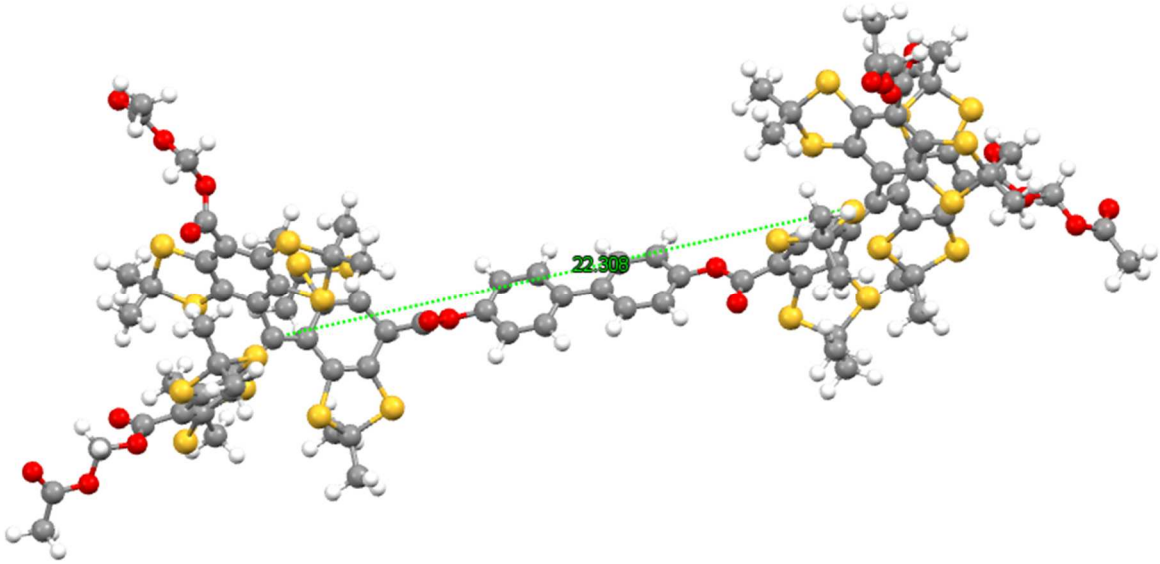

*Figure 92: Geometry optimized structure of **4**.*

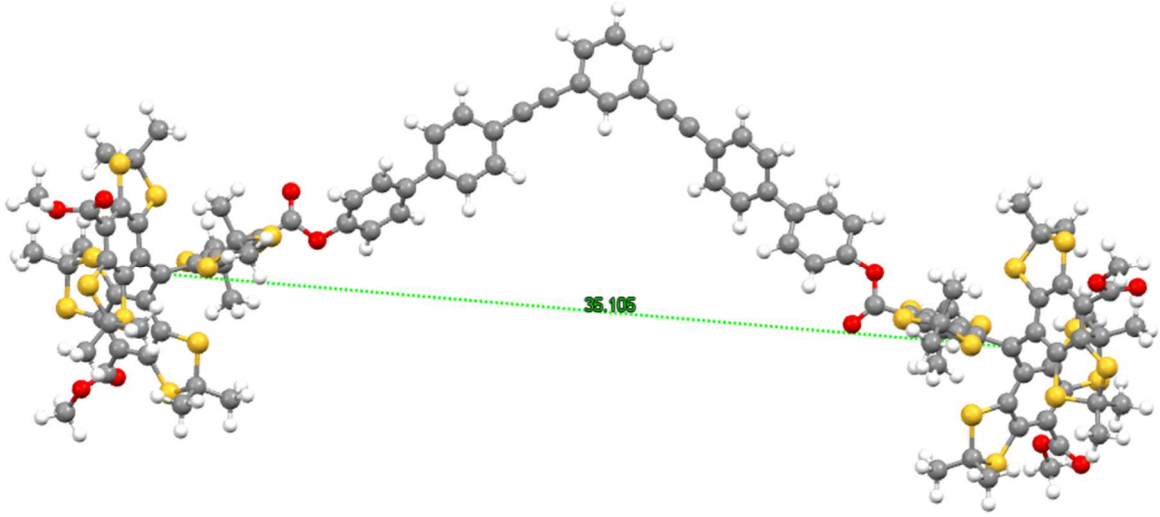

*Figure 93: Geometry optimized structure of **5**.*

The geometry of **4** and **5** was optimized using the program ORCA[145] via a DFT calculation using the functional PBE0 and the basis set def2-TZVP. In order to accelerate the optimization for these large molecules, RIJCOSX approximation was used with the auxiliary functional D3BJ.

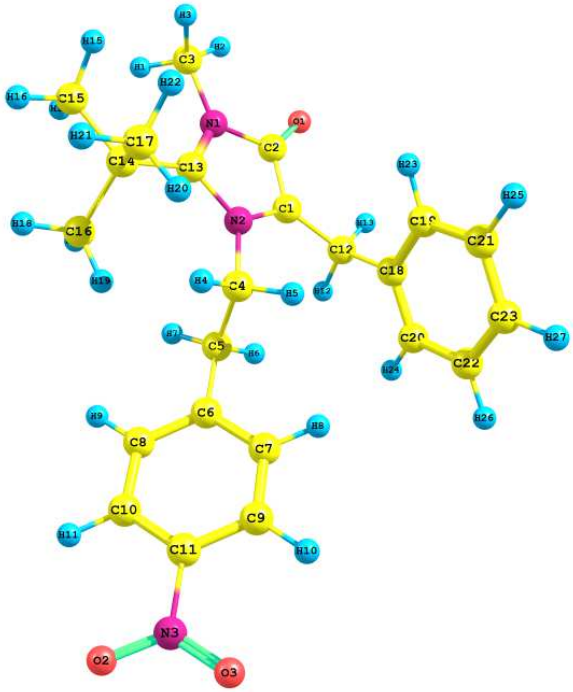

*Figure 94: DFT optimized structure of **16***

DFT-calculated HFC of **16**

Nucleus H1 :

Raw HFC matrix (all values in MHz):

-0.9167	-1.1601	0.2025
-1.1601	0.7764	0.4441
0.2025	0.4441	-1.6218

Nucleus H2 :

Raw HFC matrix (all values in MHz):

-1.7467	-1.8634	0.5198
-1.8634	3.3079	-0.1772
0.5198	-0.1772	-2.4114

Nucleus H3 :

Raw HFC matrix (all values in MHz):

-1.9825	-0.3327	0.5044
-0.3327	0.9032	-0.6130
0.5044	-0.6130	-1.7879

Nucleus H4 :

Raw HFC matrix (all values in MHz):

0.5632	-0.4096	2.1146
-0.4096	-2.0536	-0.1377
2.1146	-0.1377	-1.0638

Nucleus H5 :

Raw HFC matrix (all values in MHz):

1.9555	-1.3364	1.9110
-1.3364	-1.2152	-0.3641
1.9110	-0.3641	-1.3759

Nucleus H6 :

Raw HFC matrix (all values in MHz):

-0.8504	-0.6512	1.2399
-0.6512	0.1091	-1.4868
1.2399	-1.4868	1.2709

Nucleus H7 :

Raw HFC matrix (all values in MHz):

-1.1659	-0.1390	0.8202
-0.1390	-0.7202	-0.7705
0.8202	-0.7705	1.8893

Nucleus H8 :

Raw HFC matrix (all values in MHz):

0.2039	-0.5128	0.4785
-0.5128	-0.0885	-0.3228
0.4785	-0.3228	-0.1609

Nucleus H9 :

Raw HFC matrix (all values in MHz):

-0.2233	-0.0430	0.3583
-0.0430	-0.2903	-0.1200
0.3583	-0.1200	0.5178

Nucleus H10 :

Raw HFC matrix (all values in MHz):

0.1034	-0.1645	0.1857
-0.1645	-0.0531	-0.1073
0.1857	-0.1073	-0.0321

Nucleus H11 :

Raw HFC matrix (all values in MHz):

-0.0360	-0.0339	0.1835
-0.0339	-0.1301	-0.0536
0.1835	-0.0536	0.1495

Nucleus H12 :

Raw HFC matrix (all values in MHz):

61.1948	0.0149	-0.2471
0.0149	68.8650	-2.6795
-0.2471	-2.6795	62.6866

Nucleus H13 :

Raw HFC matrix (all values in MHz):

1.7833	0.6624	1.0243
0.6624	8.4036	2.6817
1.0243	2.6817	2.1776

Nucleus H14 :

Raw HFC matrix (all values in MHz):

-0.8054	-0.6269	-0.1863
-0.6269	1.1289	0.9867
-0.1863	0.9867	-0.6609

Nucleus H15 :

Raw HFC matrix (all values in MHz):

-0.9118	-0.0174	0.0900
-0.0174	1.6474	0.0968
0.0900	0.0968	-0.9559

Nucleus H16 :

Raw HFC matrix (all values in MHz):

-1.2255	0.1815	0.0735
0.1815	0.2915	0.6444
0.0735	0.6444	-1.0079

Nucleus H17 :

Raw HFC matrix (all values in MHz):

-1.6172	0.3209	-0.4221
0.3209	-1.5151	1.1891
-0.4221	1.1891	1.6189

Nucleus H18 :

Raw HFC matrix (all values in MHz):

3.9195	0.5506	0.5088
0.5506	4.8733	0.9956
0.5088	0.9956	5.0230

Nucleus H19 :

Raw HFC matrix (all values in MHz):

-0.7670	0.0267	1.6007
0.0267	-1.2451	0.2630
1.6007	0.2630	0.7355

Nucleus H20 :

Raw HFC matrix (all values in MHz):

1.9241	0.6361	0.6042
0.6361	-0.9216	0.4656
0.6042	0.4656	-1.8258

Nucleus H21 :

Raw HFC matrix (all values in MHz):

7.2436	1.1243	0.4333
1.1243	7.6815	0.9100

0.4333 0.9100 6.9053

Nucleus H22 :

Raw HFC matrix (all values in MHz):

-0.7048 1.9779 -0.5565

1.9779 -0.3472 -0.6433

-0.5565 -0.6433 -1.1896

Nucleus H23 :

Raw HFC matrix (all values in MHz):

0.6354 -1.6298 -2.6758

-1.6298 -2.1433 0.8153

-2.6758 0.8153 0.6653

Nucleus H24 :

Raw HFC matrix (all values in MHz):

-0.4276 -0.9168 0.0993

-0.9168 0.8780 -0.5242

0.0993 -0.5242 -0.9606

Nucleus H25 :

Raw HFC matrix (all values in MHz):

1.1688 -0.3400 -0.5919

-0.3400 0.4010 0.1857

-0.5919 0.1857 0.6077

Nucleus H26 :

Raw HFC matrix (all values in MHz):

0.3061 -0.4187 0.0300

-0.4187 0.6482 -0.0956

0.0300 -0.0956 -0.0538

Nucleus H27 :

Raw HFC matrix (all values in MHz):

0.0900	-0.3691	-0.2278
-0.3691	-0.4844	0.2011
-0.2278	0.2011	-0.5664

Nucleus C1 :

Raw HFC matrix (all values in MHz):

45.0565	12.2161	-58.5377
12.2161	-2.5396	-15.1887
-58.5377	-15.1887	60.6018

Nucleus C2 :

Raw HFC matrix (all values in MHz):

-27.9826	0.2625	2.1317
0.2625	-33.4679	-0.2699
2.1317	-0.2699	-28.7924

Nucleus C3 :

Raw HFC matrix (all values in MHz):

-0.5536	-0.2310	0.1675
-0.2310	0.4489	0.0881
0.1675	0.0881	-0.6568

Nucleus C4 :

Raw HFC matrix (all values in MHz):

-0.1239	-0.2194	0.7388
-0.2194	-0.5759	-0.1286
0.7388	-0.1286	-0.4827

Nucleus C5 :

Raw HFC matrix (all values in MHz):

1.1383	-0.1449	0.3816
-0.1449	1.1957	-0.2702
0.3816	-0.2702	1.5226

Nucleus C6 :

Raw HFC matrix (all values in MHz):

-0.1777	-0.0619	0.1443
-0.0619	-0.2193	-0.0814
0.1443	-0.0814	-0.0783

Nucleus C7 :

Raw HFC matrix (all values in MHz):

0.0457	-0.0720	0.1107
-0.0720	-0.0202	-0.0777
0.1107	-0.0777	0.0121

Nucleus C8 :

Raw HFC matrix (all values in MHz):

-0.0191	-0.0212	0.0946
-0.0212	-0.0656	-0.0553
0.0946	-0.0553	0.0856

Nucleus C9 :

Raw HFC matrix (all values in MHz):

0.0021	-0.0504	0.0678
-0.0504	-0.0471	-0.0325
0.0678	-0.0325	-0.0136

Nucleus C10 :

Raw HFC matrix (all values in MHz):

-0.0196	-0.0207	0.0647
-0.0207	-0.0565	-0.0197
0.0647	-0.0197	0.0259

Nucleus C11 :

Raw HFC matrix (all values in MHz):

0.0191	-0.0117	0.0494
-0.0117	-0.0036	-0.0346
0.0494	-0.0346	0.0239

Nucleus C12 :

Raw HFC matrix (all values in MHz):

-16.0270	-0.3949	-1.1783
-0.3949	-15.2783	-0.4415
-1.1783	-0.4415	-15.2389

Nucleus C13 :

Raw HFC matrix (all values in MHz):

25.8104	7.4676	-28.9919
7.4676	4.1540	-7.5840
-28.9919	-7.5840	34.2616

Nucleus C14 :

Raw HFC matrix (all values in MHz):

-6.9760	0.4321	-0.8033
0.4321	-7.1005	-0.0083
-0.8033	-0.0083	-6.6462

Nucleus C15 :

Raw HFC matrix (all values in MHz):

-0.0764	-0.0059	0.0267

-0.0059	0.7131	0.2028
0.0267	0.2028	-0.0201

Nucleus C16 :

Raw HFC matrix (all values in MHz):

9.1927	0.1994	0.8335
0.1994	9.1070	0.5990
0.8335	0.5990	11.7203

Nucleus C17 :

Raw HFC matrix (all values in MHz):

15.2341	1.7385	-0.2448
1.7385	12.9447	-0.0909
-0.2448	-0.0909	11.9972

Nucleus C18 :

Raw HFC matrix (all values in MHz):

20.3379	-2.8890	-2.3359
-2.8890	20.2739	2.2607
-2.3359	2.2607	19.2252

Nucleus C19 :

Raw HFC matrix (all values in MHz):

-0.6277	0.2479	-0.3841
0.2479	0.7729	0.5210
-0.3841	0.5210	-1.1185

Nucleus C20 :

Raw HFC matrix (all values in MHz):

-0.9644	-0.4576	0.2645
-0.4576	-0.9384	-0.2326

0.2645 -0.2326 -0.8635

Nucleus C21 :

Raw HFC matrix (all values in MHz):

-0.3967 -0.2837 -0.3057

-0.2837 -0.6348 -0.0540

-0.3057 -0.0540 -0.6454

Nucleus C22 :

Raw HFC matrix (all values in MHz):

0.4073 -0.0796 0.2059

-0.0796 0.0627 0.0349

0.2059 0.0349 0.0223

Nucleus C23 :

Raw HFC matrix (all values in MHz):

0.8987 0.1525 0.3885

0.1525 0.6103 0.3845

0.3885 0.3845 0.8490

Nucleus N1 :

Raw HFC matrix (all values in MHz):

-4.1269 -0.2546 0.4778

-0.2546 -3.5470 0.0739

0.4778 0.0739 -4.2544

Nucleus N2 :

Raw HFC matrix (all values in MHz):

-5.3007 0.1763 -0.0427

0.1763 -5.5240 -0.0386

-0.0427 -0.0386 -5.0034

Nucleus N3 :

Raw HFC matrix (all values in MHz):

0.0006	-0.0045	0.0098
-0.0045	-0.0071	-0.0039
0.0098	-0.0039	0.0007

Nucleus O1 :

Raw HFC matrix (all values in MHz):

-32.2323	-19.0550	75.3122
-19.0550	28.6114	21.3962
75.3122	21.3962	-49.2616

Nucleus O2 :

Raw HFC matrix (all values in MHz):

-0.0023	0.0019	-0.0137
0.0019	0.0068	0.0071
-0.0137	0.0071	-0.0058

Nucleus O3 :

Raw HFC matrix (all values in MHz):

-0.0067	0.0062	-0.0132
0.0062	0.0053	0.0085
-0.0132	0.0085	0.0001

Appendix D: Biochemical Procedures

Disclaimer: The procedures presented here were developed and implemented by Fraser Duthie, B. Sc.. They are included to give context to the labeling efficiencies determined by Andreas Berndhäuser.

*Labeling of CYP101 with **7***

A fivefold excess of label **7** (26 µL of a 25 mM stock solution in DMSO, 640 nmol) was added to GF buffer (2.90 mL, pH = 7.4; 150 mM NaCl, 20 mM TRIS) in a 15-mL-Falcon tube. Lastly, the protein sample (50 µL of a 2.56 mM solution in the above mentioned buffer, 128 nmol) was transferred into the Falcon® tube and the solution was incubated in the dark during 4 h at room temperature. The labeling solution was concentrated to a volume of 2.5 mL (Vivaspin 6/10000) and the labeled protein was isolated by means of size exclusion chromatography (PD-10 column).

*Labeling of CYP101 with **6***

A fivefold excess of **6** (23 µL of a 28 mM stock solution in DMSO, 640 nmol) was added to a mixture of GF buffer (2.75 mL, pH = 8.0; 150 mM NaCl, 20 mM TRIS) and DDM (30 µL of a 10%-DDM solution in above mentioned buffer) in a 15-mL-Falcon tube. Lastly, the protein sample (50 µL of a 2.56 mM solution in the above mentioned buffer, 128 nmol) was transferred into the Falcon® tube and the solution was incubated in the dark during 4 h at room temperature. The incubation was continued for another 16 h at 5 °C. The labeling solution was concentrated to a volume of 2.5 mL (Vivaspin 6/10000) and the labeled protein was isolated by means of size exclusion chromatography (PD-10 column).

*Labeling of CYP101 with **8***

A fivefold excess of label **8** (73 µL of a 8.8 mM stock solution in DMSO, 640 nmol) was added to GF buffer (2.95 mL, pH = 8.0; 150 mM NaCl, 20 mM TRIS) in a 15-mL-Falcon tube. Lastly, the protein sample (50 µL of a 2.56 mM solution in the above mentioned buffer, 128 nmol) was transferred into the Falcon® tube and the solution was incubated in the dark during 4 h at room temperature. The incubation was continued for another 16 h at 5 °C. The labeling solution was concentrated to a volume of 2.5 mL (Vivaspin 6/10000) and the labeled protein was isolated by means of size exclusion chromatography (PD-10 column).

*Labeling of FeoB with **9***

An eightfold excess of label **9** (400 nL of a 100 mM stock solution in DMSO, 41 nmol) was added to a mixture of GF buffer (20.6 µL, pH = 8.0; 150 mM NaCl, 20 mM TRIS), $CuSO_4$ (5 µL of a 2 mM aqueous solution), sodium ascorbate (5 µL of a 2 mM aqueous solution) and TBTA (Tris(benzyltriazolylmethyl)amine, 1 µL of a 5 mM aqueous solution) in a 1-mL-Eppendorf tube. Lastly, the protein sample (68 µL of a 75 µM solution in the above

mentioned buffer, 5.1 nmol) was transferred into the Eppendorf tube and the solution was incubated in the dark during 2 h at room temperature. The labeling solution was diluted to a total volume of 500 µL, the observed precipitate was separated by centrifugation and the labeled protein was isolated by means of size exclusion chromatography (PD-25 column).

Publications

Papers

A. Berndhäuser, J.-J. Jassoy, F. Duthie, S. P. Kühn, G. Hageluecken, O. Schiemann, *Angew. Chem. Int. Ed.* **2017**, *56*, 177-181.

T. Wang, M. Schrempp, A. Berndhäuser, O. Schiemann, D. Menche, *Org. Lett.* **2015**, *17*, 3982-3985.

Posters

A. Berndhäuser, J.-J. Jassoy, F. Duthie, G. Hagelueken, O. Schiemann, *38th FGMR Discussion Meeting*, Düsseldorf, **12.09.2016-15.09.2016**, "Triarylmethyl Radicals as Spin Labels for Distance Measurements on Proteins".

A. Berndhäuser, J.-J. Jassoy, O. Schiemann, *Young Researcher Workshop 2016*, Konstanz, **11.04.2016-14.04.2016**, "Triarylmethyl Radicals (Trityl) as Spin Labels for Biomacromolecules".

A. Berndhäuser, J.-J. Jassoy, F. Duthie, G. Hagelueken, O. Schiemann, *Annual Meeting of the DFG Priority Program 1601*, Hirschegg, **04.10.2016-08.10.2016**, "Triarylmethyl Radicals for Distance Measurements on Proteins".

A. Berndhäuser, J.-J. Jassoy, G. W. Reginsson, G. Hageluecken, O. Schiemann*, Proposal Evaluation Meeting for the DFG Priority Program 1601*, Göttingen, **21.01.2015-23.01.2015**, "Trityl radicals as Spin Labels".

A. Berndhäuser, B. Mladenova, J. Bächle, S. Grimme, G. Grampp, O. Schiemann, *7th Summer School of the European Federation of EPR Groups*, Berlin, **24.08.2015-31.08.2015**, "Electrochemistry and EPR of Organic Salts".

A. Berndhäuser, J.-J. Jassoy, O. Schiemann, *37th FGMR Discussion Meeting*, Darmstadt, **07.09.2015-10.09.2015**, "Triarylmethyl Radicals as Spin Labels for Biomolecules".

A. Berndhäuser, O. Schiemann, *35th FGMR Discussion Meeting*, Frauenchiemsee, **09.09.2015-12.09.2013**, "Synthesis of Trityl based Spin Labels".

Presentations

A. Berndhäuser, *Young Researchers Workshop 2016,* Konstanz, **11.04.2016-14.04.2016**,
"Synthesis of Trityl Spin Labels and their use in RIDME distance measurements on CYP101"

A. Berndhäuser, *Young Researchers Workshop 2014,* Bonn, **31.03.2014-02.04.2014**,
"Synthesis of Trityl Spin Labels for EPR distance measurements"

A. Berndhäuser, *Young Researchers Workshop 2013,* Berlin, **03.04.2013-05.04.2013**,
"Synthesis and EPR characterization of Trityl Spin Labels"

List of Figures

List of Tables

Abbreviations

AWG	Arbitrary wave function generator
BMPA	Bis(2-pyridylmethyl)azine
CD	Circular dichroism
CW-EPR	Continuous wave electron paramagnetic resonance
DEER	Double electron-electron resonance
DFT	Density functional theory
DQC	Double quantum coherence
ENDOR	Electron Nuclear Double Resonance
EPR	Electron paramagnetic resonance
ESEEM	Electron spin echo envelope modulation
FFT	Fast Fourier transform
FRET	Fluorescence resonance energy transfer
FWHM	Full width at half maximum
HYSCORE	Hyperfine sublevel correlation spectroscopy
MD	Molecular dynamics
MTSSL	(1-Oxyl-2,2,5,5-tetramethylpyrroline-3-methyl) methanethiosulfonate spin label
NMR	Nuclear magnetic resonance
OD	Optical density
PDB	Protein data bank
PELDOR	Pulsed electron-electron paramagnetic resonance
RIDME	Relaxation-induced dipolar modulation enhancement
RMSD	Root-mean-square deviation
RMSE	Root means square error of the fit
SDSL	Site-directed spin labeling
SIFTER	Single frequency technique for refocusing dipolar couplings
SNR	Signal-to-noise ratio

tBu-BMPA	Bis(2-pyridylmethyl-5-tert-butyl)azine
THIQ	Tetrahydoisoquinolines

Literature

[1] J. M. Berg, J. L. Tymoczko, L. Stryer, *Biochemistry*, W.H. Freeman, Basingstoke, **2012**.

[2] a) B. Loll, J. Kern, W. Saenger, A. Zouni, J. Biesiadka, *Nature* **2005**, *438*, 1040-1044; b) J.-R. Shen, *Nature* **2016**, *530*, 168-169; c) E. Malito, A. Carfi, M. J. Bottomley, *International Journal of Molecular Sciences* **2015**, *16*, 13106-13140.

[3] A. Doerr, *Nat. Meth.* **2015**, *12*, 1112-1113.

[4] I. Bertini, C. Luchinat, G. Parigi, R. Pierattelli, *Dalton Trans.* **2008**, 3782-3790.

[5] E. Nogales, *Nat. Meth.* **2016**, *13*, 24-27.

[6] a) E. Hirata, E. Kiyokawa, *Biophys. J.* **2016**, *111*, 1103-1111; b) R. Roy, S. Hohng, T. Ha, *Nat. Meth.* **2008**, *5*, 507-516.

[7] a) O. Schiemann, T. F. Prisner, *Q. Rev. Biophys.* **2007**, *40*, 1-53; b) T. Schmidt, M. A. Wälti, J. L. Baber, E. J. Hustedt, G. M. Clore, *Angew. Chem. Int. Ed.* **2016**, *55*, 15905-15909.

[8] R. E. Martin, M. Pannier, F. Diederich, V. Gramlich, M. Hubrich, H. W. Spiess, *Angew. Chem. Int. Ed.* **1998**, *37*, 2833-2837.

[9] S. Milikisyants, F. Scarpelli, M. G. Finiguerra, M. Ubbink, M. Huber, *J. Magn. Reson.* **2009**, *201*, 48-56.

[10] J. H. Freed, *J. Chem. Phys.* **1997**, *107*, 1317-1340.

[11] P. P. Borbat, A. J. Costa-Filho, K. A. Earle, J. K. Moscicki, J. H. Freed, *Science* **2001**, *291*, 266.

[12] D. Goldfarb, *Phys. Chem. Chem. Phys.* **2014**, *16*, 9685-9699.

[13] a) G. Y. Shevelev, O. A. Krumkacheva, A. A. Lomzov, A. A. Kuzhelev, D. V. Trukhin, O. Y. Rogozhnikova, V. M. Tormyshev, D. V. Pyshnyi, M. V. Fedin, E. G. Bagryanskaya, *J. Phys. Chem. B* **2015**, *119*, 13641-13648; b) G. W. Reginsson, N. C. Kunjir, S. T. Sigurdsson, O. Schiemann, *Chemistry* **2012**, *18*, 13580-13584.

[14] M. Qi, A. Groß, G. Jeschke, A. Godt, M. Drescher, *J. Am. Chem. Soc.* **2014**, *136*, 15366-15378.

[15] D. Goldfarb, *PCCP* **2014**, *16*, 9685-9699.

[16] A. Collauto, V. Frydman, M. D. Lee, E. H. Abdelkader, A. Feintuch, J. D. Swarbrick, B. Graham, G. Otting, D. Goldfarb, *Phys. Chem. Chem. Phys.* **2016**, *18*, 19037-19049.

[17] A. A. Kuzhelev, D. V. Trukhin, O. A. Krumkacheva, R. K. Strizhakov, O. Y. Rogozhnikova, T. I. Troitskaya, M. V. Fedin, V. M. Tormyshev, E. G. Bagryanskaya, *J. Phys. Chem. B* **2015**, *119*, 13630-13640.

[18] P. K. Das, B. Geul, S.-B. Choi, S.-D. Yoo, Y.-I. Park, *Plant Signaling & Behavior* **2011**, *6*, 23-25.

[19] E. C. Gentry, R. R. Knowles, *Acc. Chem. Res.* **2016**, *49*, 1546-1556.

[20] a) R. A. Marcus, *Phys. Chem. Chem. Phys.* **2012**, *14*, 13729-13730; b) R. A. Marcus, *J. Chem. Phys.* **1956**, *24*, 966-978.

[21] a) J. F. Endicott, Y.-J. Chen, P. Xie, *Coord. Chem. Rev.* **2005**, *249*, 343-373; b) N. Sutin, C. Creutz, *J. Chem. Educ.* **1983**, *60*, 809.

[22] a) H. Miyabe, A. Kawashima, E. Yoshioka, S. Kohtani, *Chemistry – A European Journal* **2017**, *23*, 6225-6236; b) D. S. G. Henriques, K. Zimmer, S. Klare, A. Meyer, E. Rojo-Wiechel, M. Bauer, R. Sure, S. Grimme, O. Schiemann, R. A. Flowers, A. Gansäuer, *Angew. Chem. Int. Ed.* **2016**, *55*, 7671-7675.

[23] a) A. Schweiger, G. Jeschke, *Principles of Pulse Electron Paramagnetic Resonance*, Oxford University Press, **2001**; b) A. Bencini, D. Gatteschi, *Electron Paramagnetic Resonance of Exchange Coupled Systems*, Springer-Verlag, **1990**; c) J. A. Weil, J. R. Bolton, *Electron paramagnetic resonance: elementary theory and practical*

applications, John Wiley & Sons, **2007**; d) G. Jeschke, University of Konstanz, Chair of Physical Chemistry, **2008**.
[24] B. B. A. Abragram, *Electron Paramagnetic Resonance of Transition Ions* Oxford University Press, Oxford, **1970**.
[25] D. Abdullin, Rheinische Friedrich-Wilhelms University (Bonn), **2017**.
[26] a) G. Y. Shevelev, O. A. Krumkacheva, A. A. Lomzov, A. A. Kuzhelev, O. Y. Rogozhnikova, D. V. Trukhin, T. I. Troitskaya, V. M. Tormyshev, M. V. Fedin, D. V. Pyshnyi, E. G. Bagryanskaya, *J. Am. Chem. Soc.* **2014**, *136*, 9874-9877; b) V. Meyer, Michael A. Swanson, Laura J. Clouston, Przemysław J. Boratyński, Richard A. Stein, Hassane S. McHaourab, A. Rajca, Sandra S. Eaton, Gareth R. Eaton, *Biophys. J.* **2015**, *108*, 1213-1219.
[27] G. W. Reginsson, University of St. Andrews and University of Iceland (St. Andrews), **2013**.
[28] E. L. Hahn, *Physical Review* **1950**, *80*, 580-594.
[29] a) N. C. Kunjir, G. W. Reginsson, O. Schiemann, S. T. Sigurdsson, *PCCP* **2013**, *15*, 19673-19685; b) A. H. B. E. J. Husted, *Annu. Rev. Biophys. Biomol. Struct.* **1999**, 129-153; c) E. J. Hustedt, R. A. Stein, L. Sethaphong, S. Brandon, Z. Zhou, S. C. DeSensi, *Biophys. J.* **2006**, *90*, 340-356.
[30] A. Blank, *Phys. Chem. Chem. Phys.* **2017**, *19*, 5222-5229.
[31] P. P. Borbat, J. H. Freed, *Chem. Phys. Lett.* **1999**, *313*, 145-154.
[32] G. Jeschke, M. Pannier, A. Godt, H. W. Spiess, *Chem. Phys. Lett.* **2000**, *331*, 243-252.
[33] a) E. R. Georgieva, P. P. Borbat, C. Ginter, J. H. Freed, O. Boudker, *Nat Struct Mol Biol* **2013**, *20*, 215-221; b) G. Jeschke, *ChemPhysChem* **2002**, *3*, 927-932.
[34] G. Jeschke, Y. Polyhach, *Phys. Chem. Chem. Phys.* **2007**, *9*, 1895-1910.
[35] K. M. S. A. D. Milov, M. D. Shirov, *Fiz. Tverd. Tela* **1981**, 975-981.
[36] P. P. Borbat, E. R. Georgieva, J. H. Freed, *J. Phys. Chem. Lett.* **2013**, *4*, 170-175.
[37] a) C. E. Tait, S. Stoll, *PCCP* **2016**, *18*, 18470-18485; b) C. L. Motion, J. E. Lovett, S. Bell, S. L. Cassidy, P. A. S. Cruickshank, D. R. Bolton, R. I. Hunter, H. El Mkami, S. Van Doorslaer, G. M. Smith, *J. Phys. Chem. Lett.* **2016**, *7*, 1411-1415; c) P. E. Spindler, S. J. Glaser, T. E. Skinner, T. F. Prisner, *Angew. Chem. Int. Ed.* **2013**, *52*, 3425-3429.
[38] G. Jeschke, V. Chechik, P. Ionita, A. Godt, H. Zimmermann, J. Banham, C. R. Timmel, D. Hilger, H. Jung, *Appl. Magn. Reson.* **2006**, *30*, 473-498.
[39] a) L. V. Kulik, S. A. Dzuba, I. A. Grigoryev, Y. D. Tsvetkov, *Chem. Phys. Lett.* **2001**, *343*, 315-324; b) L. V. Kulik, I. A. Grigor'ev, E. S. Salnikov, S. A. Dzuba, Y. D. Tsvetkov, *J. Phys. Chem. A* **2003**, *107*, 3692-3695; c) L. V. Kulik, E. S. Salnikov, S. A. Dzuba, *Appl. Magn. Reson.* **2005**, *28*, 1.
[40] W. B. Mims, *Phys. Rev. B* **1972**, *5*, 2409-2419.
[41] S. Razzaghi, M. Qi, A. I. Nalepa, A. Godt, G. Jeschke, A. Savitsky, M. Yulikov, *J. Phys. Chem. Lett.* **2014**, *5*, 3970-3975.
[42] a) A. V. Astashkin, B. O. Elmore, W. Fan, J. G. Guillemette, C. Feng, *J. Am. Chem. Soc.* **2010**, *132*, 12059-12067; b) A. Savitsky, A. A. Dubinskii, M. Flores, W. Lubitz, K. Möbius, *J. Phys. Chem. B* **2007**, *111*, 6245-6262.
[43] A. V. Astashkin, *Methods Enzymol* **2015**, *563*, 251-284.
[44] a) D. Shachal, Y. Manassen, *Chem. Phys. Lett.* **1997**, *271*, 107-112; b) S. Saxena, J. H. Freed, *The Journal of Chemical Physics* **1997**, *107*, 1317-1340.
[45] P. Schöps, P. E. Spindler, A. Marko, T. F. Prisner, *J. Magn. Reson.* **2015**, *250*, 55-62.
[46] T. F. P. O. Schiemann, *Q. Rev. Biophys.* **2007**, *40*, 1-53.
[47] a) C. Altenbach, S. L. Flitsch, H. G. Khorana, W. L. Hubbell, *Biochemistry* **1989**, *28*, 7806-7812; b) C. Altenbach, T. Marti, H. G. Khorana, W. L. Hubbell, *Science* **1990**, *248*, 1088.

[48] S.-i. Ohnishi, H. M. McConnell, *J. Am. Chem. Soc.* **1965**, *87*, 2293-2293.
[49] L. J. Berliner, J. Grunwald, H. O. Hankovszky, K. Hideg, *Anal. Biochem.* **1982**, *119*, 450-455.
[50] M. Azarkh, V. Singh, O. Okle, I. T. Seemann, D. R. Dietrich, J. S. Hartig, M. Drescher, *Nat. Protocols* **2013**, *8*, 131-147.
[51] a) I. A. Kirilyuk, A. A. Bobko, S. V. Semenov, D. A. Komarov, I. G. Irtegova, I. A. Grigor'ev, E. Bagryanskaya, *J. Org. Chem.* **2015**, *80*, 9118-9125; b) I. A. Kirilyuk, Y. F. Polienko, O. A. Krumkacheva, R. K. Strizhakov, Y. V. Gatilov, I. A. Grigor'ev, E. G. Bagryanskaya, *J. Org. Chem.* **2012**, *77*, 8016-8027.
[52] J. H. Ardenkjær-Larsen, I. Laursen, I. Leunbach, G. Ehnholm, L. G. Wistrand, J. S. Petersson, K. Golman, *J. Magn. Reson.* **1998**, *133*, 1-12.
[53] Z. Yang, Y. Liu, P. Borbat, J. L. Zweier, J. H. Freed, W. L. Hubbell, *J. Am. Chem. Soc.* **2012**, *134*, 9950-9952.
[54] A. A. Kuzhelev, D. V. Trukhin, O. A. Krumkacheva, R. K. Strizhakov, O. Y. Rogozhnikova, T. I. Troitskaya, M. V. Fedin, V. M. Tormyshev, E. G. Bagryanskaya, *J. Phys. Chem. B* **2015**, *119*, 13630-13640.
[55] M. R. Fleissner, E. M. Brustad, T. Kálai, C. Altenbach, D. Cascio, F. B. Peters, K. Hideg, S. Peuker, P. G. Schultz, W. L. Hubbell, *Proceedings of the National Academy of Sciences* **2009**, *106*, 21637-21642.
[56] K. Mobius, *Chem. Soc. Rev.* **2000**, *29*, 129-139.
[57] M. L. Genova, in *The Structural Basis of Biological Energy, Vol. 39* (Ed.: M. F. Hohmann-Mariott), Springer Netherlands, Dordrecht, **2014**, pp. 401-417.
[58] A. J. Birch, *Journal of the Chemical Society (Resumed)* **1944**, 430-436.
[59] a) A. Gansäuer, C. Kube, K. Daasbjerg, R. Sure, S. Grimme, G. D. Fianu, D. V. Sadasivam, R. A. Flowers, *J. Am. Chem. Soc.* **2014**, *136*, 1663-1671; b) N. Funken, F. Mühlhaus, A. Gansäuer, *Angew. Chem. Int. Ed.* **2016**, *55*, 12030-12034.
[60] a) H. Taube, H. Myers, R. L. Rich, *J. Am. Chem. Soc.* **1953**, *75*, 4118-4119; b) H. Taube, *Pure Appl. Chem.* **1975**, *44*, 25-42.
[61] R. A. Marcus, *J. Chem. Phys.* **1965**, *43*, 679-701.
[62] a) S. V. Rosokha, J. K. Kochi, *J. Am. Chem. Soc.* **2007**, *129*, 3683-3697; b) T. E. de Jongh, M. Hoffmann, O. Einsle, D. Cavazzini, G.-L. Rossi, M. Ubbink, G. W. Canters, *Eur. J. Inorg. Chem.* **2007**, *2007*, 2627-2634.
[63] a) E. K. J. Huheey, R. Keiter, *Anorganische Chemie*, 2. Edition ed., de Gruyter, Berlin **1995**; b) T. L. O. P. W. Atkins, J. P. Rourke, M. T. Weller, F. A. Armstrong, M. Hagerman, *Shriver and Atkins` Inorganic Chemistry*, 5th Edition ed., Oxford University Press, New York, **2010**.
[64] R. A. Marcus, *Reviews of Modern Physics* **1993**, *65*, 599-610.
[65] a) H. Staerk, R. Treichel, A. Weller, *Chem. Phys. Lett.* **1983**, *96*, 28-30; b) S. N. Batchelor, K. A. McLauchlan, I. A. Shkrob, in *Z. Phys. Chem., Vol. 180*, **1993**, p. 9.
[66] Y. A. Im, D. H. Busch, *J. Am. Chem. Soc.* **1961**, *83*, 3357-3362.
[67] R. L. Ward, S. I. Weissman, *J. Am. Chem. Soc.* **1957**, *79*, 2086-2090.
[68] a) G. Grampp, A. Kapturkiewicz, W. Jaenicke, *Berichte der Bunsengesellschaft für physikalische Chemie* **1990**, *94*, 439-447; b) H. Larsen, S. U. Pedersen, J. A. Pedersen, H. Lund, *J. Electroanal. Chem.* **1992**, *331*, 971-983; c) C. D. Stevenson, C. V. Rice, *J. Am. Chem. Soc.* **1995**, *117*, 10551-10554.
[69] G. Grampp, *Spectrochimica Acta Part A: Molecular and Biomolecular Spectroscopy* **1998**, *54*, 2349-2358.
[70] a) G. Grampp, K. Rasmussen, *PCCP* **2002**, *4*, 5546-5549; b) J. Bächle, B. Mladenova, G. Grampp, *Chem. Phys. Lett.* **2015**, *620*, 35-37.
[71] G. W. Reginsson, O. Schiemann, *The Biochemical journal* **2011**, *434*, 353-363.

[72] G. Y. Shevelev, O. A. Krumkacheva, A. A. Lomzov, A. A. Kuzhelev, O. Y. Rogozhnikova, D. V. Trukhin, T. I. Troitskaya, V. M. Tormyshev, M. V. Fedin, D. V. Pyshnyi, E. G. Bagryanskaya, *J Am Chem Soc* **2014**, *136*, 9874-9877.
[73] Y. Liu, F. A. Villamena, J. Sun, T.-y. Wang, J. L. Zweier, *Free Radical Biol. Med.* **2009**, *46*, 876-883.
[74] W. Takahashi, A. A. Bobko, I. Dhimitruka, H. Hirata, J. L. Zweier, A. Samouilov, V. V. Khramtsov, *Appl. Magn. Reson.* **2014**, *45*, 817-826.
[75] D. Akhmetzyanov, P. Schops, A. Marko, N. C. Kunjir, S. T. Sigurdsson, T. F. Prisner, *Phys. Chem. Chem. Phys.* **2015**, *17*, 24446-24451.
[76] N. C. Kunjir, G. W. Reginsson, O. Schiemann, S. T. Sigurdsson, *Phys. Chem. Chem. Phys.* **2013**, *15*, 19673-19685.
[77] L. Yong, J. Harbridge, R. W. Quine, G. A. Rinard, S. S. Eaton, G. R. Eaton, C. Mailer, E. Barth, H. J. Halpern, *J Magn Reson* **2001**, *152*, 156-161.
[78] J. E. Banham, C. M. Baker, S. Ceola, I. J. Day, G. H. Grant, E. J. J. Groenen, C. T. Rodgers, G. Jeschke, C. R. Timmel, *J. Magn. Reson.* **2008**, *191*, 202-218.
[79] P. Lueders, G. Jeschke, M. Yulikov, *J. Phys. Chem. Lett.* **2011**, *2*, 604-609.
[80] H. Chen, A. G. Maryasov, O. Y. Rogozhnikova, D. V. Trukhin, V. M. Tormyshev, M. K. Bowman, *Phys. Chem. Chem. Phys.* **2016**, *18*, 24954-24965.
[81] a) N. K. H. Swartz, *Biological Magnetic Resonance, Vol. 23*, Kluwer Academic New York, **2005**; b) R. Owenius, G. R. Eaton, S. S. Eaton, *J. Magn. Reson.* **2005**, *172*, 168-175.
[82] P. E. Spindler, P. Schöps, A. M. Bowen, B. Endeward, T. F. Prisner, in *eMagRes*, John Wiley & Sons, Ltd, **2007**.
[83] B. Joseph, V. M. Tormyshev, O. Y. Rogozhnikova, D. Akhmetzyanov, E. G. Bagryanskaya, T. F. Prisner, *Angew. Chem. Int. Ed.* **2016**, *128*, 11710-11714.
[84] S. Bleicken, G. Jeschke, C. Stegmueller, R. Salvador-Gallego, Ana J. García-Sáez, E. Bordignon, *Mol. Cell* **2014**, *56*, 496-505.
[85] B. Endeward, J. A. Butterwick, R. MacKinnon, T. F. Prisner, *J. Am. Chem. Soc.* **2009**, *131*, 15246-15250.
[86] S. Stoll, A. Schweiger, *J. Magn. Reson.* **2006**, *178*, 42-55.
[87] D. Abdullin, F. Duthie, A. Meyer, E. S. Müller, G. Hagelueken, O. Schiemann, *J. Phys. Chem. B* **2015**, *119*, 13534-13542.
[88] A. Martorana, Y. Yang, Y. Zhao, Q.-F. Li, X.-C. Su, D. Goldfarb, *Dalton Trans.* **2015**, *44*, 20812-20816.
[89] Y. Yang, Q. F. Li, C. Cao, F. Huang, X. C. Su, *Chemistry* **2013**, *19*, 1097-1103.
[90] C. Bello, K. Farbiarz, J. F. Möller, C. F. W. Becker, T. Schwientek, *Chem. Sci.* **2014**, *5*, 1634.
[91] Y. T. Lee, E. C. Glazer, R. F. Wilson, C. D. Stout, D. B. Goodin, *Biochemistry* **2011**, *50*, 693-703.
[92] a) P. Ding, D. Wunnicke, H. J. Steinhoff, F. Seela, *Chemistry* **2010**, *16*, 14385-14396; b) O. Schiemann, N. Piton, J. Plackmeyer, B. E. Bode, T. F. Prisner, J. W. Engels, *Nat. Protocols* **2007**, *2*, 904-923.
[93] D. Abdullin, N. Florin, G. Hagelueken, O. Schiemann, *Angew. Chem. Int. Ed.* **2015**, *54*, 1827-1831.
[94] G. Hagelueken, R. Ward, J. H. Naismith, O. Schiemann, *Appl. Magn. Reson.* **2012**, *42*, 377-391.
[95] N. R. Voss, M. Gerstein, *Nucleic Acids Res.* **2010**, *38*, W555-W562.
[96] F. C. Mascali, H. Y. V. Ching, R. M. Rasia, S. Un, L. C. Tabares, *Angew. Chem. Int. Ed.* **2016**, *55*, 11041-11043.
[97] a) A. Martorana, G. Bellapadrona, A. Feintuch, E. Di Gregorio, S. Aime, D. Goldfarb, *J. Am. Chem. Soc.* **2014**, *136*, 13458-13465; b) F.-X. Theillet, A. Binolfi, B. Bekei, A.

Martorana, H. M. Rose, M. Stuiver, S. Verzini, D. Lorenz, M. van Rossum, D. Goldfarb, P. Selenko, *Nature* **2016**, *530*, 45-50.
[98] B. Joseph, A. Sikora, E. Bordignon, G. Jeschke, D. S. Cafiso, T. F. Prisner, *Angew. Chem. Int. Ed.* **2015**, *54*, 6196-6199.
[99] J. Broggi, T. Terme, P. Vanelle, *Angew. Chem. Int. Ed.* **2014**, *53*, 384-413.
[100] F. Nami, P. Gast, E. J. Groenen, *Appl. Magn. Reson.* **2016**, *47*, 643-653.
[101] a) M. Felleisen, *Elektrochemie für Dummies*, Wiley-VCH, Weinheim, **2015**; b) U. v. Rienen, Rostock, **2007**.
[102] L. Michaelis, M. P. Schubert, S. Granick, *J. Am. Chem. Soc.* **1939**, *61*, 1981-1992.
[103] a) L. D. Andreas Neudeck, *Electrochim. Acta* **1995**, *40*, 1427-1434; b) L. D. Andreas Petr, Andreas Neudeck, *J. Electroanal. Chem.* **1996**, *412*, 153-158.
[104] X. Jia, *Synthesis* **2016**, *48*, 18-30.
[105] S. S. Turner, P. Day, *J. Mater. Chem.* **2005**, *15*, 23-25.
[106] R. K. K. Kubo, *Topics in Organometallic Chemistry* **2009**, *27*, 35-53.
[107] a) H. M. Yamamoto, *RIKEN Review* **2002**, *46*, 3-6; b) A. L. Kanibolotsky, N. J. Findlay, P. J. Skabara, *Beilstein J. Org. Chem.* **2015**, *11*, 1749-1766.
[108] A. V. Lonchakov, O. A. Rakitin, N. P. Gritsan, A. V. Zibarev, *Molecules* **2013**, *18*, 9850-9900.
[109] D. Dolphin, R. H. Felton, *Acc. Chem. Res.* **1974**, *7*, 26-32.
[110] S. F. Nelsen, M. T. Ramm, R. F. Ismagilov, M. A. Nagy, D. A. Trieber, D. R. Powell, X. Chen, J. J. Gengler, Q. Qu, J. L. Brandt, J. R. Pladziewicz, *J. Am. Chem. Soc.* **1997**, *119*, 5900-5907.
[111] L. K. E. T. Kaiser, *Radical Ions*, 1. Edition ed., Krieger Publishing Company Inc. , Malabar, **1968**.
[112] M. Goez, I. Frisch, I. Sartorius, *Beilstein J. Org. Chem.* **2013**, *9*, 437-446.
[113] W. H. F. Gerson, *Electron Spin Resonance Spectroscopy of Organic Radicals*, Wiley VCH, **2003**.
[114] G. Wedler, *Lehrbuch der Physikalischen Chemie*, 5. Edition ed., Wiley-VCH, Weinheim, **2004**.
[115] W. M. Haynes, *Handbook of Chemistry and Physics*, 92. Edition ed., CRC Press, Boca Raton, **2011**.
[116] S. V. Rosokha, J. K. Kochi, *J. Am. Chem. Soc.* **2001**, *123*, 8985-8999.
[117] K. Rasmussen, T. Hussain, S. Landgraf, G. Grampp, *J. Phys. Chem. A* **2012**, *116*, 193-198.
[118] M. D. Liptak, R. D. Fagerlund, E. C. Ledgerwood, S. M. Wilbanks, K. L. Bren, *J. Am. Chem. Soc.* **2011**, *133*, 1153-1155.
[119] D. Sun, S. V. Rosokha, J. K. Kochi, *J. Am. Chem. Soc.* **2004**, *126*, 1388-1401.
[120] a) X. Chen, K. M. Engle, D. H. Wang, J. Q. Yu, *Angew Chem Int Ed Engl* **2009**, *48*, 5094-5115; b) R. G. B. D. A. Colby, J. A. Ellman, *Chem. Rev.* **2010**, *110*, 624-655.
[121] a) K. Ueda, S. Yanagisawa, J. Yamaguchi, K. Itami, *Angew Chem Int Ed Engl* **2010**, *49*, 8946-8949; b) K. U. S. Yanagashiwa, H. Sekizawa, K. Itami, *J. Am. Chem. Soc.* **2009**, *131*, 14622-14623.
[122] Z. Li, C.-J. Li, *J. Am. Chem. Soc.* **2004**, *126*, 11810-11811.
[123] X.-Z. Shu, Y.-F. Yang, X.-F. Xia, K.-G. Ji, X.-Y. Liu, Y.-M. Liang, *Org. Biomol. Chem.* **2010**, *8*, 4077-4079.
[124] H.-P. Bi, W.-W. Chen, Y.-M. Liang, C.-J. Li, *Org. Lett.* **2009**, *11*, 3246-3249.
[125] A. Sud, D. Sureshkumar, M. Klussmann, *Chem. Commun.* **2009**, 3169-3171.
[126] S. Murahashi, N. Komiya, H. Terai, *Angew. Chem. Int. Ed.* **2005**, *44*, 6931-6933.
[127] A. J. Catino, J. M. Nichols, B. J. Nettles, M. P. Doyle, *J. Am. Chem. Soc.* **2006**, *128*, 5648-5649.
[128] W. Muramatsu, K. Nakano, C.-J. Li, *Org. Biomol. Chem.* **2014**, *12*, 2189-2192.

[129] W. Muramatsu, K. Nakano, C.-J. Li, *Org. Lett.* **2013**, *15*, 3650-3653.
[130] T. Wang, M. Schrempp, A. Berndhäuser, O. Schiemann, D. Menche, *Org. Lett.* **2015**, *17*, 3982-3985.
[131] a) E. Boess, C. Schmitz, M. Klussmann, *J. Am. Chem. Soc.* **2012**, *134*, 5317-5325; b) E. Boess, D. Sureshkumar, A. Sud, C. Wirtz, C. Farès, M. Klussmann, *J. Am. Chem. Soc.* **2011**, *133*, 8106-8109.
[132] G.-J. Cheng, L.-J. Song, Y.-F. Yang, X. Zhang, O. Wiest, Y.-D. Wu, *ChemPlusChem* **2013**, *78*, 943-951.
[133] Z. Li, D. S. Bohle, C. J. Li, *Proc Natl Acad Sci U S A* **2006**, *103*, 8928-8933.
[134] N. D. Yordanov, E. Ganeva, G. Gochev, *Z. Anorg. Allg. Chem.* **1995**, *621*, 699-703.
[135] E. N. Jacobsen, A. Pfaltz, H. Yamamoto, *Comprehensive Asymmetric Catalysis: Supplement 1*, Springer Berlin Heidelberg, **2003**.
[136] M. Shibasaki, K.-I. Yamada, N. Yoshikawa, in *Lewis Acids in Organic Synthesis*, Wiley-VCH Verlag GmbH, **2000**, pp. 911-944.
[137] John Wiley & Sons, Inc., Hoboken, **2014**.
[138] R. A. Sheldon, *Asymmetric Catalysis in Organic Synthesis. Ryoji Noyori. John Wiley & Sons, Chichester, 1994.* .
[139] M. S. Taylor, E. N. Jacobsen, *Angew. Chem. Int. Ed.* **2006**, *45*, 1520-1543.
[140] K. A. Ahrendt, C. J. Borths, D. W. C. MacMillan, *J. Am. Chem. Soc.* **2000**, *122*, 4243-4244.
[141] B. List, R. A. Lerner, C. F. Barbas, *J. Am. Chem. Soc.* **2000**, *122*, 2395-2396.
[142] J. J. Devery, 3rd, J. C. Conrad, D. W. MacMillan, R. A. Flowers, 2nd, *Angew. Chem. Int. Ed.* **2010**, *49*, 6106-6110.
[143] R. Beel, S. Kobialka, M. L. Schmidt, M. Engeser, *Chem. Commun.* **2011**, *47*, 3293-3295.
[144] a) J. A. Willms, R. Beel, M. L. Schmidt, C. Mundt, M. Engeser, *Beilstein J. Org. Chem.* **2014**, *10*, 2027-2037; b) R. Beel, S. Kobialka, M. L. Schmidt, M. Engeser, *Chem. Commun.* **2011**, *47*, 3293-3295.
[145] F. Neese, *Wiley Interdiscip. Rev. Comput. Mol. Sci.* **2012**, *2*, 73-78.